Titre: Title:	From Multi-Port Interferometry to Virtual Transceiver Matrices: Reconfigurable Architectures for Multifunctional Millimeter-Wave Sensing and Communication Systems
Auteur: Author:	Seyed Ali Keivaan
Date:	2025
Type:	Mémoire ou thèse / Dissertation or Thesis
Référence: Citation:	Keivaan, S. A. (2025). From Multi-Port Interferometry to Virtual Transceiver Matrices: Reconfigurable Architectures for Multifunctional Millimeter-Wave Sensing and Communication Systems [Thèse de doctorat, Polytechnique Montréal]. PolyPublie. https://publications.polymtl.ca/71045/

POLYTECHNIQUE MONTRÉAL
affiliée à l'Université de Montréal

From Multi-Port Interferometry to Virtual Transceiver Matrices: Reconfigurable Architectures for Multifunctional Millimeter-Wave Sensing and Communication Systems

SEYED ALI KEIVAAN
Département de génie électrique

Thèse présentée en vue de l'obtention du diplôme de *Philosophiæ Doctor*
Génie électrique

Décembre 2025

POLYTECHNIQUE MONTRÉAL
affiliée à l'Université de Montréal

Cette thèse intitulée :

From Multi-Port Interferometry to Virtual Transceiver Matrices: Reconfigurable Architectures for Multifunctional Millimeter-Wave Sensing and Communication Systems

présentée par **Seyed Ali KEIVAAN**
en vue de l'obtention du diplôme de *Philosophiæ Doctor*
a été dûment acceptée par le jury d'examen constitué de :

Raman KASHYAP, président
Ke WU, membre et directeur de recherche
Tarek DJERAFI, membre
Milica POPOVIC, membre externe

DEDICATION

To my parents,
for their love, support, and invaluable sacrifices . . .

ACKNOWLEDGEMENTS

First and foremost, I would like to express my deepest gratitude to my Ph.D. advisor, Professor Ke Wu, for granting me the opportunity to pursue my doctoral studies at École Polytechnique de Montréal. His unwavering passion for research, innovative thinking, and constant encouragement have been instrumental in shaping my academic journey and guiding me through the exploration of new research frontiers. His mentorship has played a critical role in the completion of this thesis.

I would also like to express my sincere appreciation to Dr. Pascal Burasa for his support, encouragement, and friendship throughout my doctoral studies. His thoughtful advice and positive spirit were truly meaningful and greatly enriched my experience during this journey.

My heartfelt appreciation goes to the technical staff at the Poly-Grames Research Center for their invaluable assistance in the fabrication and measurement of prototypes.

I am grateful to all my colleagues and friends at École Polytechnique de Montréal for their professional support and personal camaraderie. Their advice, encouragement, and companionship made my time here truly memorable.

Most importantly, I would like to thank my family for their unconditional love and support. Their belief in me has been a constant source of strength throughout this journey.

RÉSUMÉ

L'évolution rapide des technologies sans fil dans les bandes millimétriques et térahertz a créé des besoins sans précédent pour des architectures capables d'intégrer, au sein d'une même plateforme, un système de détection haute résolution et une communication fiable. Les transceivers et réseaux phasés traditionnels, bien que performants, présentent des limites intrinsèques en termes de complexité matérielle, de consommation de puissance et de faible polyvalence. Cette thèse de doctorat répond à ces défis en développant une nouvelle classe d'architectures interférométriques multiports fondées sur les concepts de la Matrice de Réception Virtuelle (VRM) et de son extension généralisée, la Matrice de Transception Virtuelle (VTM), permettant des frontaux RF reconfigurables, évolutifs et multifonctionnels pour les systèmes intégrés de détection et communication (ISAC) de prochaine génération.

La première partie de ce travail introduit le cadre conceptuel de la VRM, où des cellules interférométriques distribuées réalisent des opérations analogiques combinatoires pour la démodulation directe, l'estimation d'angle d'arrivée et la détection multifonctionnelle. Contrairement aux récepteurs conventionnels, la VRM élimine la nécessité de chaînes de conversion complexes et de convertisseurs de données haute vitesse, en s'appuyant plutôt sur des jonctions multiports passives et la détection de puissance. Le concept est formulé théoriquement, validé expérimentalement et démontre une multifonctionnalité simultanée avec une réduction notable de la complexité matérielle.

En s'appuyant sur ces fondations, le concept VTM est proposé comme une architecture matricielle généralisée où chaque cellule peut fonctionner dynamiquement comme émetteur, récepteur ou capteur. Une innovation clé réside dans sa capacité à extraire simultanément des paramètres multidimensionnels — notamment l'angle d'arrivée 2-D (AoA) et la polarisation — tout en prenant en charge des formats de communication d'ordre élevé tels que le 64-QAM. Les modélisations théoriques et la mise en œuvre d'un prototype confirment que la VTM améliore significativement la diversité spatiale et de polarisation, permettant une multifonctionnalité robuste sans recourir à des réseaux phasés denses ni à un traitement MIMO fortement computationnel.

La contribution finale de cette thèse porte sur la conception et la réalisation d'un système automobile conjoint radar-communication (RadCom) 4D basé sur la VTM. Ce système permet la mesure simultanée de la distance, de la vitesse, de l'azimut et de l'élévation, tout en assurant une récupération fiable des symboles de communication. Les démonstrations matérielles valident une détection précise de multiples cibles dans des environnements urbains denses,

avec de fines séparations angulaires, une grande précision de vitesse et une faible erreur vectorielle (EVM) lors de la démodulation QAM. Ces résultats établissent la VTM comme une plateforme pratique et écoénergétique pour les réseaux de véhicules autonomes, les stations de base 5G/6G et les applications ISAC au-delà de la 5G.

En conclusion, cette thèse fait progresser l'état de l'art en reliant la théorie interférométrique et le matériel reconfigurable au sein d'un cadre unifié de matrices virtuelles. Les architectures VRM et VTM proposées étendent non seulement la fonctionnalité des techniques classiques à six ports, mais ouvrent également la voie à des transcepteurs mmWave/THz de grande échelle capables d'assurer simultanément communication, localisation et perception environnementale. Les résultats de cette recherche fournissent une base évolutive pour les futurs systèmes sans fil, avec des applications allant du transport intelligent aux réseaux de capteurs évolués, en passant par l'intégration térahertz sur puce.

ABSTRACT

The rapid evolution of wireless technologies in the millimeter-wave and terahertz spectrum has created unprecedented demands for architectures capable of integrating high-resolution sensing and reliable communication within a unified platform. Traditional transceivers and phased arrays, although effective, face intrinsic challenges of hardware complexity, power consumption, and limited multifunctionality. This Ph.D. dissertation addresses these challenges by developing a new class of multiport interferometric architectures based on the concepts of the Virtual Receiver Matrix (VRM) and its generalized extension, the Virtual Transceiver Matrix (VTM), enabling reconfigurable, scalable, and multifunctional front-ends for next-generation integrated sensing and communication (ISAC) systems.

The first part of this work introduces the VRM framework, where distributed interferometric cells perform combinatory analog operations for direct demodulation, direction-of-arrival estimation, and multifunctional sensing. Unlike conventional receivers, the VRM avoids complex down-conversion chains and high-speed data converters, relying instead on passive multiport junctions and power detection. The concept is theoretically formulated, experimentally validated, and shown to achieve simultaneous multi-functionality with reduced hardware complexity.

Building on this foundation, the VTM concept is proposed as a generalized matrix-based architecture where each cell can dynamically operate as a transmitter, receiver, or sensor. A key innovation lies in its ability to concurrently extract multi-dimensional parameters—including 2-D angle-of-arrival (AoA) and polarization—while supporting high-order communication formats such as 64-QAM. Theoretical modeling and prototype implementation confirm that VTM significantly improves spatial and polarization diversity, enabling robust multi-functionality without resorting to dense phased arrays or computationally intensive MIMO processing.

The final contribution of this thesis is the design and realization of a 4D automotive joint radar-communication (RadCom) system based on VTM. This system achieves simultaneous measurement of range, velocity, azimuth, and elevation, alongside reliable recovery of communication symbols. Hardware demonstrations validate accurate multi-target detection under dense urban conditions, with fine angular separations, high velocity accuracy, and low error vector magnitude in QAM demodulation. These results establish the VTM paradigm as a practical and energy-efficient platform for autonomous vehicular networks, 5G/6G base stations, and beyond-5G ISAC applications.

In conclusion, this dissertation advances the state-of-the-art by bridging interferometric theory and reconfigurable hardware into a unified framework of Virtual Matrices. The proposed VRM and VTM architectures not only extend the functionality of classical six-port techniques but also pave the way toward large-scale mmWave/THz transceivers with simultaneous communication, localization, and environmental perception. The outcomes of this research provide a scalable foundation for future wireless systems, with applications spanning intelligent transportation, smart sensing networks, and chip-scale THz integration.

TABLE OF CONTENTS

LIST OF TABLES

LIST OF FIGURES

LIST OF SYMBOLS AND ABBREVIATIONS

5G	Fifth Generation
6G	Sixth Generation
ADC	Analog-to-Digital Converter
ADAS	Advanced Driver Assisance System
AI	Artifical Intelligence
AM	Amplitude Modulation
ANN	Artificial Neural Network
AoA	Angle-of-Arrival
BER	Bit Error Rate
BPF	Bandpass Filter
CSI	Channel State Information
DAC	Digital-to-Analog Converter
DPD	Digital Predistortion
EVM	Error Vector Magnitude
FDM	Frequency Division Multiplexing
FM	Freqency Modulation
FDSS	Frequency Diversity Spread Spectrum
HC	Hybrid Coupler
I	In-Phase Component
IF	Intermediate Frequency
IoT	Internet of Things
ISAC	Integrated Sensing and Communication
JRC	Joint Radar-Communication
LNA	Low-Noise Amplifier
LO	Local Oscillator
MIMO	Multi-Input Multi-Output
ML	Machine Learning
MMIC	Monolithic Microwave Integrated Circuits
mmW	Millimeter-Wave
MSps	Mega Symbol-per-second
OFDM	Orthogonal Frequency-Division Multiplexing
PA	Power Amplifier
PC	Power Combiner

PD	Power Divider
P.S.	Phase Shifter
Q	Quadratute Component
QAM	Quadrature Amplitude Modulation
QPSK	Quadrature Phase Shift Keying
RF	Radio Freqeuncy
RIS	Reconfigurable Intelligent Surface
RX	Receiver
SDR	Software Defined Radio
SIW	Substrate Integrated Waveguide
SNR	Signal-to-Noise Ratio
SoC	System on-Chip
SPDR	Six-port Digital Receiver
TDD	Time Division Duplex
THz	Terahertz
TRX	Transceiver
TX	Transmitter
UWB	Ultra-Wideband
VRM	Virtual Receiver Matrix
VTM	Virtual Transceiver Matrix
WRI	Wave-Radio Interferometer

LIST OF APPENDICES

CHAPTER 1 INTRODUCTION

1.1 Motivation and Research Background

1.1 Motivation and Research Background

The continuous evolution of wireless technologies has shaped modern society, beginning with the pioneering work of early radio innovators and progressing to today's deployment of 5G and exploration of 6G and terahertz (THz) systems. Across this century-long journey, two core functions have consistently stood out: sensing and communication. Sensing technologies enable devices to perceive their surroundings through range, velocity, and spatial measurements among many others, while communication systems provide reliable, high-speed transfer of information—together forming the foundation of modern connected infrastructure.

Historically, these two functions have developed along separate paths. Sensing platforms were designed to locate and characterize objects, whereas communication systems focused on conveying data efficiently across changing wireless channels. This separation resulted in distinct hardware architectures, signal formats, and processing pipelines. Deploying both capabilities often required separate systems—each with its own antennas, RF chains, and processing resources—leading to increased hardware duplication, higher cost, and larger power consumption. Such parallel designs have become increasingly difficult to support in compact or energy-limited platforms.

As emerging applications—such as the Internet of Things (IoT), autonomous mobility, smart factories, and human-centric wireless environments—continue to grow, this divide has become less practical. A connected vehicle, for example, must both sense the surrounding environment with high precision and exchange information with nearby vehicles and roadside infrastructure. Similarly, industrial automation and healthcare ecosystems require devices that simultaneously perceive and communicate within shared environments. These trends have motivated the rise of a unified design approach known as Integrated Sensing and Communication (ISAC), in which a single system jointly performs sensing and data transmission. ISAC reduces hardware redundancy, improves spectral efficiency, and enables richer cross-domain functionalities where sensing information supports communication, and communication waveforms can also serve sensing purposes [1–5].

A promising pathway toward ISAC is found in multiport interferometric techniques. The six-port junction, originally conceived as a microwave power-measurement network, later became a compelling alternative to traditional quadrature demodulators by enabling ex-

traction of in-phase (I) and quadrature (Q) components without mixers or local oscillators. Over time, six-port and multiport receivers have been explored for numerous applications, including communication demodulation, phase detection, and direction-of-arrival estimation. They offer benefits such as passive operation, simplicity, and wide instantaneous bandwidth. However, conventional multiport architectures also exhibit limitations, including moderate sensitivity, calibration challenges, and restricted flexibility in multifunction scenarios [6–17].

The shift toward millimeter-wave (mmWave) and THz frequencies in next-generation wireless systems has renewed interest in such passive architectures. Conventional MIMO radars and phased arrays achieve high angular resolution but typically require many RF chains, mixers, and high-speed analog-to-digital converters—leading to substantial power consumption and hardware complexity. These demands challenge the feasibility of large-scale deployment in energy-limited or size-constrained platforms such as autonomous vehicles, drones, and wearable or handheld devices. Multiport interferometers, in contrast, naturally map incident electromagnetic fields into low-frequency baseband signals through passive analog transformation, enabling compact and power-efficient front-ends while still extracting rich spatial information.

Despite their potential, classical six-port and multiport designs are not inherently scalable or reconfigurable enough to meet the needs of modern ISAC systems. Their operation is typically fixed and tailored to specific functions, making it difficult to support simultaneous or adaptable sensing and communication tasks.

This thesis addresses these challenges by introducing two new architectures—the Virtual Receiver Matrix (VRM) and its generalized extension, the Virtual Transceiver Matrix (VTM). These matrix-based frameworks expand traditional multiport interferometry into a flexible, reconfigurable platform capable of multifunctional operation, scalable spatial processing, and efficient ISAC performance at mmWave and THz frequencies.

1.2 Objectives

1.2 Objectives

The overarching objective of this thesis is to investigate and realize virtualized multiport architectures that can unify sensing and wireless communication in a single, reconfigurable hardware framework. This general goal translates into the following specific objectives:

- To formulate the theoretical foundations of the VRM demonstrating how combinatory analog operations enable simultaneous demodulation, angle-of-arrival estimation, and multifunctional sensing.

- To extend the VRM concept into the VTM, where cells can dynamically operate as transmitters, receivers, or passive sensors, thereby enabling flexible resource allocation for integrated radar-communication systems.
- To demonstrate the capability of VTM to extract multiple dimensions of information simultaneously, including azimuth, elevation, polarization, range, and Doppler velocity, alongside the recovery of communication symbols.
- To design, fabricate, and experimentally validate prototypes of VRM- and VTM-based systems operating at millimeter-wave frequencies, particularly in the 24 GHz band for automotive radar applications.

These objectives not only aim to validate VRM and VTM as viable ISAC architectures but also to position them as scalable alternatives to conventional phased-array and MIMO approaches.

1.3 Methodology

1.3 Methodology

The methodology adopted in this research combines theoretical analysis, system simulations, hardware prototyping, and experimental validation.

Theoretical Modeling

The first step is the rigorous mathematical formulation of VRM and VTM architectures. This involves modeling hybrid coupler and combiner cells as linear operators that project incident electromagnetic fields into measurable baseband voltages. Matrix transformations are derived to map antenna inputs to detector outputs, forming the foundation for angle-of-arrival estimation, polarization detection, and joint radar-communication signal processing.

Simulations

The theoretical framework is validated through simulations carried out in MATLAB and Keysight ADS. MATLAB is used extensively for algorithmic validation, including subspace-based AoA estimation (e.g., MUSIC), range–Doppler processing, and QAM demodulation. ADS is used for circuit-level validation of SIW-based hybrid couplers, power dividers, and detector circuits. These simulations bridge the gap between high-level mathematical models and physical hardware implementations.

Hardware Prototyping

To translate the theoretical and simulated results into practice, hardware prototypes of VRM and VTM cells and arrays are fabricated. Substrate-integrated waveguide (SIW) technology is chosen for its low-loss propagation and ease of integration at mmWave frequencies. Schottky diode-based power detectors are implemented for analog baseband extraction. Both VRM-only and VTM-enabled front-ends are developed for proof-of-concept validation.

Experimental Validation

The final step involves laboratory measurements and real-world emulation. 2D AoA and polarization detection are validated using controlled signal sources and calibrated positioning setups. Range and velocity detection are validated using frequency-modulated continuous-wave (FMCW) chirps and channel emulators such as Keysight Propsim C8. Communication experiments are carried out using high-order modulation schemes (64-QAM). These experiments demonstrate the simultaneous functionality of the proposed architectures in radar and communication tasks.

1.4 Original Contributions

1.4 Original Contributions

The main original contributions of this thesis can be summarized as follows:

- The introduction and validation of VRM, a novel architecture enabling combinatory analog operations for simultaneous demodulation, AoA estimation, and multifunctional sensing using passive interferometric cells.
- The generalization of VRM into VTM, which extends functionality to reconfigurable transmit–receive operations. VTM enables concurrent extraction of azimuth, elevation, polarization, range, and Doppler velocity, while also supporting communication symbol detection.
- The design and experimental demonstration of a 4D automotive RadCom system operating at 24 GHz, integrated with VTM to achieve joint range, velocity, azimuth, and elevation detection alongside high-order QAM communication.
- A comprehensive comparative evaluation showing that VRM and VTM architectures achieve competitive or superior angular resolution and communication fidelity while re-

ducing hardware complexity, power consumption, and dependency on high-speed ADCs compared to phased-array and MIMO systems.

These contributions establish VRM and VTM as scalable, energy-efficient, and multifunctional solutions for future integrated sensing and communication systems.

1.5 Thesis Organization

1.5 Thesis Organization

This thesis is organized as follows:

- Chapter 2 reviews the state of the art in multiport interferometry, six-port techniques, and integrated sensing and communication systems, with emphasis on their evolution toward multifunctional mmWave/THz architectures.
- Chapter 3 presents the VRM, including theoretical derivations, algorithmic validations, circuit-level implementations, and experimental results.
- Chapter 4 introduces the VTM as a generalization of VRM, demonstrating its capability for concurrent 2D AoA, polarization detection, and communication symbol recovery.
- Chapter 5 details the design, fabrication, and experimental validation of a 4D automotive RadCom system, integrating VTM for accurate multi-target detection and data exchange in high-density environments.
- Chapter 6 presents the concept, implementation, and validation of a VRM architecture enabling simultaneous multifunction communication and sensing using co-frequency incident waves.
- Chapter 7 concludes the thesis by summarizing the main contributions, identifying limitations, and outlining future research directions, including extensions to terahertz on-chip systems.

CHAPTER 2 ARTICLE 1: EVOLUTION OF MULTI-PORT TRANSCEIVER SYSTEMS: FROM FOUNDATIONAL ARCHITECTURES TO VIRTUALIZED AND RECONFIGURABLE PLATFORMS

Seyed Ali Keivaan, Pascal Burasa, and Ke Wu
Published in: *Electromagnetic Science*
Date of Submission: November 11, 2025

The landscape of radiofrequency (RF) front-end design has evolved significantly over the past decades, driven by the demand for higher integration, reduced complexity, and enhanced reconfigurability. Among the key innovations, the six-port technique has emerged as a foundational architecture enabling passive and highly linear RF signal processing. Building upon its principles, multi-port front-ends have expanded to support complex modulation schemes, multi-functional operations, and millimeter-wave (mmW) integration. With the progression of integrated circuit technologies and software-defined platforms, these architectures now serve as the backbone for multifunctional communication and sensing systems. Recent developments have introduced novel frameworks such as the Virtual Receiver Matrix (VRM) and Virtual Transceiver Matrix (VTM), which provide dynamic analog reconfiguration for adaptive operation. In parallel, Reconfigurable Intelligent Surfaces (RIS) have also gained attention for their ability to manipulate electromagnetic waves passively, offering new avenues for wireless front-end design. This review presents a comprehensive analysis of the historical foundations, technological advancements, and emerging trends in multi-port RF front-ends, highlighting the trajectory from classical six-port receivers to futuristic VRM, VTM, and RIS-based architectures.

2.1 Introduction

The rapid evolution of wireless communication and sensing technologies is driving the need for RF front-end architectures that are not only compact and energy-efficient, but also adaptive and multifunctional. Conventional receiver (RX) designs rely on complex, power-intensive active components—such as mixers, local oscillators (LOs), and elaborate calibration chains to suppress non-linearities—which inherently limit scalability and efficiency. These legacy architectures struggle to meet the stringent requirements of emerging applications like 5G/6G networks, vehicular radar, and the Internet of Things (IoT), where high scalability, low power consumption, and real-time reconfigurability are paramount.

An important step in rethinking front-end design was the emergence of multi-port RF architectures, with the six-port technique standing out as a significant milestone. Initially introduced for passive vector network analysis, six-port systems were later adapted into RX topologies due to their unique capability of extracting both amplitude and phase information through simple scalar power measurements and calibration [6,18]. These systems offered high linearity and broadband performance without requiring active mixers, making them suitable for high-frequency and low-power applications [7]. The six-port architecture has evolved into more generalized multi-port front-end systems that support reconfigurable operation, dual-band processing, and signal discrimination—features that are crucial for emerging multifunctional wireless platforms [19].

The recent introduction of VRM [20] and VTM [21] architectures has added a new dimension to this field. These reconfigurable analog frameworks support dynamic signal routing and real-time front-end adaptation, allowing multifunctional operation across standards and protocols without significant digital overhead [22]. By enabling analog domain programmability, VRM and VTM systems can support concurrent signal paths and they are especially well-suited for integrated sensing and communication (ISAC) applications [23].

To better contextualize this evolution, Fig. 2.1(a) presents a three-stage progression of multi-port RF front-ends: from classical six-port and interferometric architectures to fully AI-integrated VTM systems. The first stage relies on passive components with limited reconfigurability, constrained to basic communication and sensing tasks. The second stage illustrates the VTM, where dynamic analog matrix allocation and power-aware design enable scalable, multifunctional platforms. Finally, the third stage highlights AI-assisted VTM, characterized by real-time adaptive reconfiguration, intelligent spectrum management, and simultaneous support for ISAC, edge intelligence, and enhanced security. This architectural shift reflects the convergence of RF hardware with intelligent control, marking a foundational transition toward future 6G-ready reconfigurable systems.

The growing research interest in multi-port RF systems is further evidenced by the sharp increase in related publications over the past two decades. As shown in Fig. 2.1(b), the number of journal and conference papers focusing on multi-port RXs, transmitters (TXs), transceivers (TRXs), sensors, and radar systems has experienced exponential growth since 2000, with a particularly steep rise after 2015. This trend, derived from the Compendex database, highlights the field's rapid evolution and the increasing relevance of multi-port and virtualized RF front-end technologies in wireless systems such as emerging communication and sensing applications. In a parallel but complementary direction, RIS have emerged as passive Metasurface-based solutions capable of dynamically shaping the propagation environment.

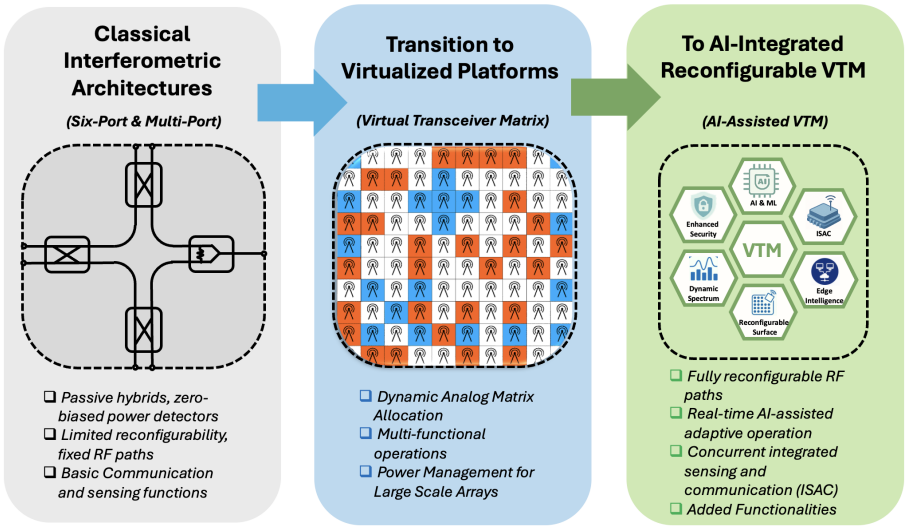

(a)

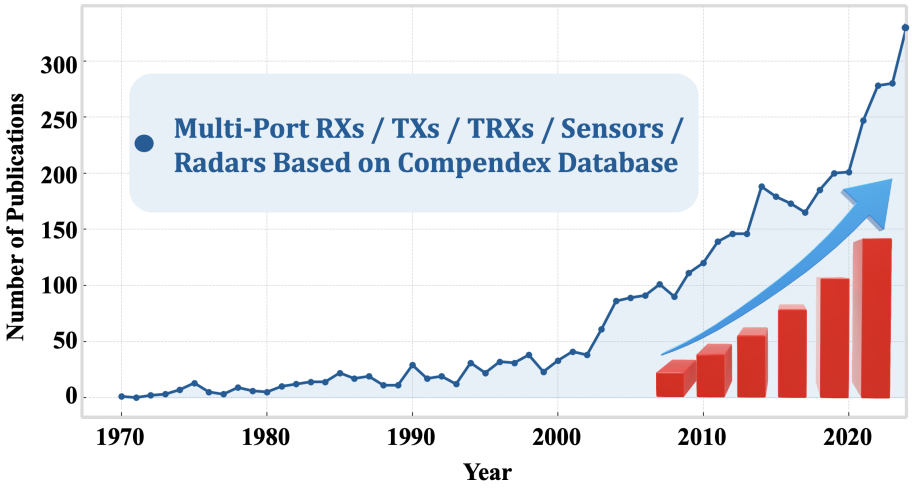

(b)

Figure 2.1 (a) Conceptual overview of the evolution and applications of multi-port TRX systems, highlighting their transition from classical architectures to virtualized and reconfigurable platforms, and their roles in sensing, communication, and integrated multifunctional systems. (b) Annual number of published papers related to multi-port RF front-end systems and reconfigurable architectures from 1970 to 2025, based on Engineering Village database records. The figure reflects the historical progression and recent surge in research interest, corresponding to the emergence of integrated multifunctional RF front-end technologies, and Virtual Transceiver Matrix (VTM).

Unlike six-port or VRM/VTM systems, RIS operates at the electromagnetic wavefront level, altering the wireless channel itself rather than signal chains [24]. Despite these differences, RIS shares key goals such as reconfigurability, spectrum efficiency, and low-power operation, positioning it as a promising component of next-generation reconfigurable RF systems [25].

This paper provides a comprehensive review of multi-port RF front-end technologies, tracing the development from classical six-port RXs to advanced VRM/VTM systems and RIS-enabled architectures. Section 2.2 discusses the historical development of six-port and early multi-port architectures. Section 2.3 explores modern hardware advances, including Software Defined Radio (SDR) integration and mmW implementations. Section 2.4 addresses calibration, linearity, and machine learning (ML) enhancements. Section 2.5 examines multifunctional and concurrent system designs. Section 2.6 delves into the structure and application of VRM and VTM frameworks. Section 2.7 elaborates on futuristic aspects of ML-VTM. Section 2.8 presents recent trends in RIS-enabled RXs. Section 2.9 offers comparative benchmarks, and Sections 2.10 and 2.11 conclude with future directions and reflections.

2.2 Historical Evolution of Multiport Architectures

2.2.1 Classical Six-Port Junctions

The origin of six-port technology is deeply rooted in microwave network analysis, where it was initially conceived as a passive reflectometric method for measuring complex reflection coefficients. Introduced in the 1970s and formalized in the early 1980s, the six-port junction provided a means to determine both magnitude and phase information of a signal using only power detectors and a set of calibrated loads [18]. This approach offered a unique alternative to conventional vector network analyzers, which relied heavily on active circuitry and phase-sensitive detection.

The theoretical foundation of the six-port concept is based on the principle of constructive and destructive interference at multiple linear combining junctions. The incident unknown RF signal at the input port is distributed among several paths through hybrid couplers or Wilkinson dividers together with a known reference source at the reference port, and the resulting four outputs are measured using square-law detectors. The system response is characterized by a set of calibration coefficients derived from known standards, enabling accurate reconstruction of amplitude and phase of the input signal [26, 27].

The leap from instrumentation to communication systems occurred when researchers began exploring six-port junctions for direct down-conversion in RXs. This transition was driven by the architecture's inherent advantages, including wideband operation, linearity,

low-power, and the elimination of active mixers [6]. In the 1990s, experimental six-port RXs demonstrated successful demodulation of Amplitude Modulation (AM), Frequency Modulation (FM), Quadrature Phase Shift Keying (QPSK), and other modulation formats, proving the architecture's capability as a practical RF front-end [7, 28]. Its passive nature also contributed to excellent linearity and low intermodulation distortion, features desirable for low power and broadband applications.

In this early phase, key milestones included the use of dual-tone calibration [29], advanced modeling of nonlinearities [30], and demonstration of system-level integration in automotive radar platforms [31]. The six-port junction thus evolved from a laboratory novelty into a viable candidate for low-cost, high-performance RF RXs. Building upon this foundational success, the research community soon explored ways to generalize and expand the concept to more complex and higher-order structures, paving the way for early multi-port architectures.

2.2.2 Early Multi-Port Architectures

The foundational success of six-port technology catalyzed a series of developments that expanded into broader multi-port RX and TX architectures. Early research efforts explored configurations such as five-port, eight-port, and even ten-port structures to improve system versatility, signal processing capability, and performance across bandwidth and modulation domains. These systems were aimed at enhancing direct conversion functionalities, increasing calibration redundancy, and enabling more sophisticated demodulation mechanisms suitable for broadband and high-data-rate communications [32].

One key direction in this evolution was the adaptation of multi-port RXs for both analog and hybrid analog-digital designs. The six-port direct conversion RX, proposed in various configurations, demonstrated real-time quadrature demodulation without relying on mixers or frequency down-conversion chains. Notably, [8] presented a mmW six-port RX operating in the 23–31 GHz range with integrated monolithic microwave circuit design, optimized for QPSK-based mass-market communication. This RX utilized a wideband six-port junction and a multi-chip module approach to simplify baseband processing while preserving linearity and noise resilience.

Building on these developments, [33] advanced the concept by introducing a Ka-band six-port analog front-end tailored for software-defined direct conversion receivers. In contrast to earlier approaches that required four ADCs to digitize detector outputs, their design employed analog vector formation and differential baseband circuitry to directly generate I/Q signals. This allowed the system to demodulate higher-order digitally modulated signals, including BPSK, QPSK, 8PSK, 16PSK, and even 16QAM, at data rates up to 40 Mb/s

without resorting to high-speed ADCs or extensive digital post-processing. The direct detection of such constellations purely through analog processing is particularly unique, as it significantly reduces hardware complexity and computational burden while maintaining excellent constellation fidelity and phase accuracy.

In parallel, comparative studies between six-port digital RXs (SPDRs) and conventional zero-IF demodulators reinforced the benefits of multi-port architectures in suppressing LO phase noise and interference. Such comparisons revealed that six-port structures offered robust performance under noise and co-channel interference, maintaining BERs suitable for high-speed QPSK operation at rates above 40 Mb/s [34].

To extend six-port applicability into ultra-wideband (UWB) domains, several studies integrated Frequency Diversity Spread Spectrum (FDSS) and DS-UWB approaches with multi-port front-ends. For instance, FDSS-enabled six-port RXs demonstrated frequency diversity by simultaneously transmitting multiple carriers, enhancing robustness against jamming and multipath fading without relying on complex synchronization mechanisms [35]. In another effort, the six-port RAKE RX architecture was proposed for DS-UWB systems to facilitate analog correlation and demodulation while alleviating digital processing burden, further confirming the analog strengths of multi-port designs in dense multipath environments [36].

The multi-port concept was not limited to reception. The wave-radio interferometer (WRI) architecture extended six-port concepts into dual-function TRXs, merging modulation and demodulation paths into a compact, reconfigurable platform. Using FPGA-controlled switches, the WRI could alternate between transmission and reception in QPSK systems, offering flexibility and signal integrity over UWB ranges such as 3.1–4.1 GHz [37]. Beyond the canonical six-port topology, reduced-order designs like the five-port RX also gained attention. By employing a combination of high-pass and low-pass phase shifters and only three detectors, these RXs maintained broadband operation (300 MHz–2.7 GHz) while reducing complexity and LO-RF coupling issues [38]. With these early developments setting the stage, research soon turned to advancing the hardware capabilities of multi-port systems—pushing toward integration, miniaturization, and support for emerging wireless technologies, as discussed in the next section.

2.3 Hardware Advances in Modern Multi-Port Systems

2.3.1 Integration with Software-Defined Radio (SDR)

The convergence of multi-port RF architectures with SDR technology marks a pivotal shift in the adaptability and scalability of wireless front-end systems. SDRs enable radio func-

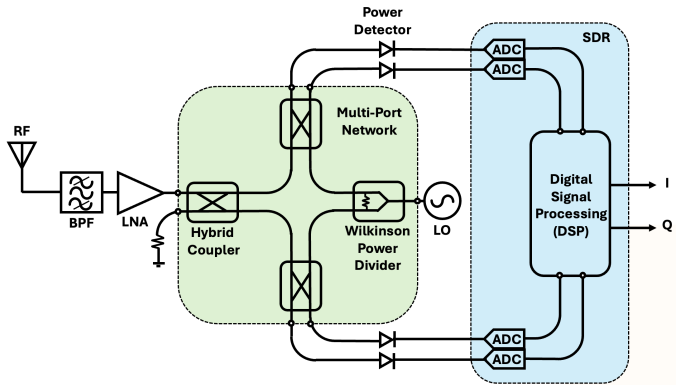

Figure 2.2 Block diagram of a six-port receiver integrated with an SDR system, illustrating signal flow from antenna through the six-port junction, power detection, digitization, and digital baseband processing.

tions—such as modulation, demodulation, and filtering—to be implemented in software, offering an unparalleled degree of reconfigurability and real-time flexibility. The passive nature of six-port architectures makes them particularly well-suited for SDR integration, as they simplify the analog front-end by eliminating active mixers (see Fig. 2.2).

Early attempts to integrate six-port systems with SDR platforms demonstrated significant promise [9,39–45]. In one notable study, a six-port-based digital RX was employed for QPSK demodulation at high speeds, showing strong compatibility with SDR frameworks [6]. These systems relied on square-law detectors and high-speed ADCs to digitize the outputs of the multi-port junction, with baseband signal recovery handled in software. This separation of analog and digital domains enabled not only flexibility in modulation schemes but also enhanced linearity and dynamic range.

Subsequent implementations expanded the scope to include orthogonal frequency-division multiplexing (OFDM), where software-defined six-port RXs demonstrated robust performance in multipath environments [46]. The key advantage of this architecture was its ability to maintain frequency agility and signal integrity without the added complexity of conventional down-conversion chains.

Moreover, MMIC-based six-port junctions provided a pathway for miniaturized and integrated SDR-compatible hardware. By embedding the passive multi-port structure directly into monolithic substrates, researchers achieved compact form factors with reduced parasitics and improved phase stability [47]. These innovations laid the groundwork for future SDR-driven reconfigurable radios, particularly in satellite and mmW communication systems. The synergy between six-port architectures and SDRs underscores the value of hybrid

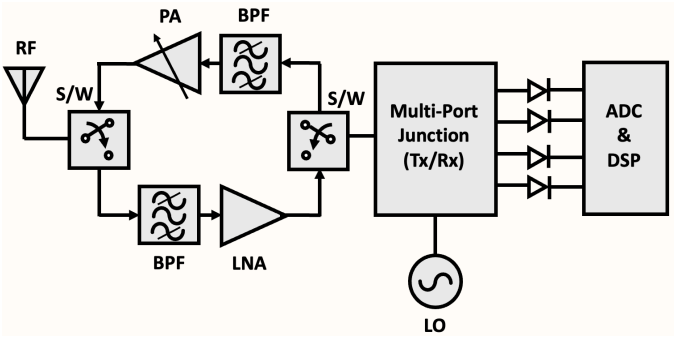

Figure 2.3 Time-division duplex multi-port TRX architecture showing TX/RX pathways via a central multi-port junction and switches with hybrid coupler for signal isolation.

analog-digital design approaches. While SDRs offer digital versatility, six-port junctions provide linear and wideband analog signal conversion with minimal hardware. This fusion is especially promising for future 5G/6G systems, where rapid reconfiguration, spectrum sharing, and multi-standard coexistence are key performance metrics. With software-defined integration establishing a flexible digital interface, the next frontier in multi-port system evolution focuses on enabling full TRX operation and bidirectional communication—topics explored in the following subsection.

2.3.2 Toward Full-Duplex Operations

As wireless systems increasingly demand simultaneous transmission and reception within compact hardware environments, the development of multi-port transmitters (TXs) and full-duplex RF front-ends has emerged as a critical advancement. Extending the six-port concept to bidirectional operation necessitated innovations in port configuration, isolation techniques, and signal linearization strategies.

Initial implementations demonstrated six-port transceivers (TRXs) capable of supporting time-division duplex (TDD) schemes with integrated switching logic (see Fig. 2.3). These designs leveraged the symmetrical nature of multi-port junctions to alternate between transmit and receive functions, enabling compact and power-efficient solutions suitable for gigabit-rate communications. For example, a 2.4 GHz prototype utilized a single six-port junction along with a switched reflection coefficient generator and analog decoder, achieving 15 Mbps QPSK modulation in transmit mode and 10 Mbps demodulation in receive mode [10].

More advanced implementations extended this concept to millimeter-wave (mmW) frequencies. A 61 GHz six-port TRX was proposed with integrated beam-switching antennas and

TDD, using variable reflection loads for modulation and direct digital reception. The system supported PSK and QAM signals with high directionality and compact integration, making it suitable for MIMO and 5G applications [48].

In parallel, frequency-division multiplexing (FDM) was used to boost throughput. A 60–64 GHz six-port V-band TRX achieved 4 Gbps data rates using four QPSK sub-carriers and ceramic hybrid couplers, demonstrating efficient mixer-less operation and low BER performance [49].

Following the evolution toward bidirectional operation, modern multi-port systems must also address physical integration challenges, especially as systems scale toward mmW and THz frequencies. These challenges are examined in the next subsection. Moreover, a surge in activity has been seen in bias-point initialization techniques.

2.3.3 Miniaturization and Substrate Integration Technologies

As RF systems continue to scale in both frequency and complexity, miniaturization and substrate-level integration have become indispensable in realizing practical multi-port RXs and TRXs. The passive nature of six-port junctions inherently supports integration into compact planar structures and non-planar structures, and their evolution into substrate-integrated waveguide (SIW), monolithic microwave integrated circuits (MMICs), and silicon-germanium (SiGe) technologies has significantly expanded their utility in modern wireless systems.

Early breakthroughs in Ka-band MMICs implementations demonstrated the feasibility of embedding six-port architectures into compact, low-loss front-end modules [47]. These MMICs-based RXs leveraged advanced GaAs semiconductor fabrication techniques to optimize phase accuracy, matching, and bandwidth. The resulting devices were capable of handling complex modulation formats and high-frequency operations within a minimal footprint, marking a major step toward portable and embedded applications.

Parallel advancements in SIW technology introduced new opportunities for low-profile, multilayer integration. Half-mode SIW configurations were used to develop broadband six-port front-ends that maintained high isolation and low insertion loss, suitable for radar and direct-conversion systems [50, 51]. These approaches not only enhanced electromagnetic performance but also facilitated low-cost mass production using PCB-like processes. In the automotive and mmW sensing domains, integration into SiGe semiconductor processes enabled the realization of high-performance, on-chip six-port RXs operating at 77 GHz and above [11]. Such systems demonstrated real-time angle-of-arrival (AoA) detection capabilities, making

them ideal for collision avoidance radar and autonomous navigation applications. Building on these advancements, earlier work at 60 GHz introduced a low-power, fully integrated six-port TRX in 0.13 µm CMOS for gigabit software-defined TRX applications, achieving up to 4 Gb/s data rates with high modulation accuracy after real-time calibration [9]. More recently, a fully integrated 120 GHz six-port front-end fabricated in 130-nm SiGe BiCMOS technology exemplified the state-of-the-art in compact radar-on-chip solutions [52].

Ultra-low-power implementations have also been developed for portable applications, including motion-sensitive radar systems operating at microwatt levels of power consumption [53]. These devices are notable for achieving high sensitivity and motion detection accuracy without compromising size or energy efficiency. At the system level, integration trends have culminated in all-in-one multi-port RX modules designed for gigabit backhaul and ISAC use cases, combining reconfigurable RF circuitry, power detectors, and analog routing into a unified substrate [54].

While miniaturization and substrate integration optimize spatial and material efficiency, the next challenge lies in extending these systems to mmW and terahertz (THz) frequencies, where dispersion, parasitics, and losses become critical limitations. These aspects are discussed in the next subsection.

2.3.4 mmW and THz Implementation Challenges

Scaling multi-port architectures to mmW and THz frequency bands introduces a host of challenges related to component accuracy, loss mechanisms, material selection, and system calibration. While the theoretical framework of six-port systems remains valid at high frequencies, practical implementation becomes increasingly difficult due to parasitic effects, fabrication tolerances, and dielectric losses [55–62].

Early implementations of six-port RXs at mmW frequencies, such as 30–60 GHz, highlighted the feasibility of direct down-conversion and interferometric detection in high-speed systems [6, 8]. However, these designs faced limitations in terms of signal-to-noise ratio (SNR), thermal drift, and phase imbalance due to the reduced wavelength and increased sensitivity to substrate properties.

One critical challenge is the realization of wideband and low-loss passive components such as hybrid couplers, dividers, and delay lines at mmW and THz frequencies. Even slight dimensional mismatches or material inhomogeneities can significantly distort the phase and amplitude response, leading to degradation in demodulation accuracy. Studies have shown that substrate-integrated solutions can partially mitigate this issue but often require multi-

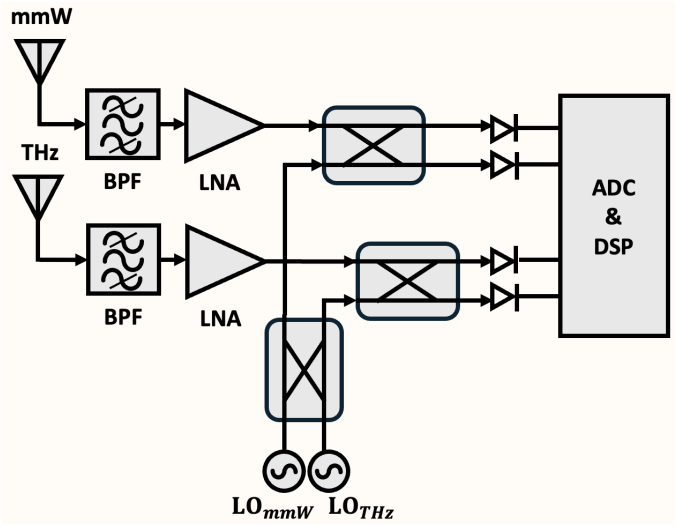

Figure 2.4 Block diagram and signal flow of the unified mmW-THz interferometric receiver [52].

layer or multi-dielectric stack-ups, which increase complexity and cost [51].

Thermal stability and power handling also become prominent issues at higher frequencies. Devices operating above 60 GHz must maintain consistent impedance and isolation across temperature fluctuations, which is difficult to guarantee with conventional PCB or LTCC substrates. Furthermore, power detectors at these frequencies demand extremely fast response times and high dynamic range, necessitating specialized diode technologies and calibration schemes [48].

In the THz domain (0.1–1 THz), six-port systems face additional constraints. The fabrication of passive junctions with sub-micron precision is essential, often requiring photonic or MEMS-compatible processes. Moreover, integrating antennas, RF networks, and detection circuits on the same die becomes critical for maintaining low loss and phase coherence [62]. While recent advances in silicon photonics and plasmonic materials show promise, their commercial viability and large-scale reproducibility remain open issues.

Fig. 2.4 illustrates a dual-band receiver (RX) architecture capable of simultaneously processing millimeter-wave (mmW) and terahertz (THz) signals [63]. Two separate antennas are used to capture mmW and THz signals, which are then passed through dedicated bandpass filters (BPFs) to remove out-of-band noise and interference. Each filtered signal is amplified by a low-noise amplifier (LNA) before being down-converted.

The mmW signal is down-converted using a six-port technique driven by a local oscillator

(LO) operating at LO_{mmW}, while the THz signal requires a two-stage mixing process. The first hybrid coupler combines the THz signal with an intermediate LO to generate an intermediate frequency (IF), which is then down-converted again using a second hybrid coupler driven by LO_{THz}.

Both down-converted signals are then digitized by analog-to-digital converters (ADCs) and processed digitally in the DSP block. This architecture supports wideband sensing and communication by enabling joint processing of mmW and THz signals.

As these implementations push the boundaries of frequency and fabrication, the next frontier lies in system-level convergence and co-integration—particularly with on-chip analog-digital hybrid designs. This is explored further in the final subsection of Section 2.3.

2.3.5 On-Chip Multi-Port Systems

The integration of multi-port RF front-ends into monolithic semiconductor platforms represents a significant milestone in the miniaturization and commercialization of these technologies. On-chip implementations reduce interconnect parasitics, improve electromagnetic stability, and enable seamless co-integration with baseband and digital processing circuits, all of which are essential for scalable, high-performance wireless systems [9].

One of the earliest breakthroughs in this domain was the development of a 77 GHz six-port RX front-end in a SiGe process, which demonstrated real-time AoA estimation with compact, automotive-grade packaging [11]. This achievement illustrated that six-port systems could be realized at mmW frequencies using mature BiCMOS fabrication processes while maintaining high precision and integration density.

Subsequent efforts pushed this boundary to even higher frequencies. A fully integrated 120 GHz six-port RX fabricated in 130 nm SiGe BiCMOS technology showcased phase and amplitude reconstruction in a single-chip front-end suitable for radar sensing and gigabit data transmission [52]. These systems featured embedded phase detectors, power sensors, and analog baseband processors—all within a single silicon die.

Meanwhile, low-power CMOS implementations have enabled the design of battery-powered or energy-harvested six-port radars, achieving high sensitivity with microwatt-level power consumption [64]. These designs are particularly valuable in wearable, biomedical, and IoT scenarios where energy efficiency and form factor are critical constraints.

More recent developments have reached into the THz domain. A 300 GHz dual-polarized CMOS waveguide RX demonstrated high-density integration for multichannel THz systems-on-chip (SoC), supporting both communication and sensing functionalities (see Fig. 2.5)

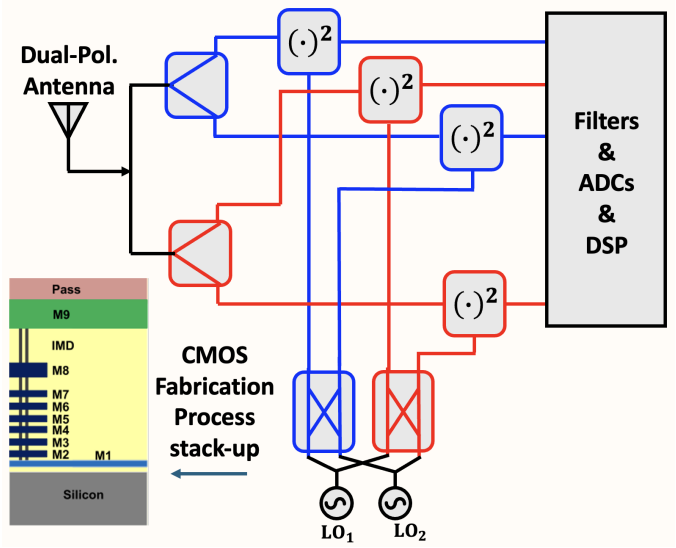

Figure 2.5 Block diagram and signal flow of the 300 GHz dual-polarized CMOS waveguide receiver [54].

[65]. These on-chip implementations underscore the transition of multi-port systems from laboratory-scale prototypes to commercially viable RF front-ends. The ability to synthesize advanced signal processing directly on-chip opens new frontiers for radar imaging, ISAC platforms, and intelligent edge communication nodes.

With the hardware landscape now firmly extended into software-defined, full-duplex, high-frequency, and chip-scale implementations, the next set of challenges revolves around precision calibration, and enhanced linearity—topics which are explored in Section 2.4.

2.4 Trends in Calibration and Linearity Enhancement For Multi-port Systems

2.4.1 Evolution of Calibration Strategies

Calibration plays a central role in multi-port RF systems, as the accurate reconstruction of amplitude and phase information hinges on precise knowledge of the network's response. Historically, six-port and multi-port systems required exhaustive calibration procedures involving known reference loads, network analyzers, and elaborate modeling. However, the evolution of calibration strategies has paralleled the hardware and algorithmic advances in multi-port architectures, moving from static methods to adaptive, machine-learning-enhanced techniques [66–73].

The earliest approaches were based on deterministic standards such as load, short, and offset

reflection terminations. These methods established the linear relationship between measured power levels and the incident signal's complex envelope through analytical matrix inversion [18]. While accurate, these techniques required stringent control over environmental and hardware parameters, making them labor-intensive and prone to drift.

To address the limitations of traditional calibration, dual-tone and three-point calibration techniques were developed to reduce complexity while maintaining accuracy [29]. These methods used a set of controlled input signals to generate internal reference vectors, which could then be mapped to system responses using algebraic transformation. This strategy reduced dependency on external reference components and enabled practical implementations in mobile and vehicular systems.

The real shift in calibration philosophy began with the adoption of blind and semi-blind algorithms. These techniques exploit signal statistics, redundancy, or known pilot sequences in communication signals to derive calibration parameters without physical references [74]. For instance, blind calibration methods using least-squares estimation or covariance matching have proven effective in real-time cognitive radio systems.

With the rise of ML, especially in the 2010s, new strategies emerged that leveraged artificial neural networks (ANNs), support vector regression (SVR), and time-delay networks for adaptive and nonlinear calibration. These models are trained using either synthetic or empirical data and can generalize to unseen configurations, thereby reducing the need for manual intervention [75, 76]. ANNs have been used for tasks such as direction finding, error mitigation, and sensor calibration in six-port systems, offering resilience to hardware variability and environmental noise [71].

Recent developments include low-complexity calibration schemes for SDRs and radar applications, such as squircle-based geometric fitting and multivariate compensation [44, 77]. These methods combine analytical modeling with learning-based residual correction, ensuring both explainability and adaptability.

The trajectory of calibration strategies reflects a broader trend toward autonomy and cognitive functionality in RF systems. As hardware continues to scale, and operating conditions become more dynamic, future calibration will likely rely even more on embedded intelligence, cross-domain feedback, and online learning algorithms. Fig. 2.6 illustrates the evolution of calibration techniques in RF and communication systems, transitioning from manual methods to ML-assisted calibration. The leftmost column outlines Manual Calibration, which involves injecting a known reference signal, manually switching to calibration loads, measuring detector outputs, calculating calibration coefficients, and applying static correction. The middle column shows Auto Calibration, which automates the process by generating ref-

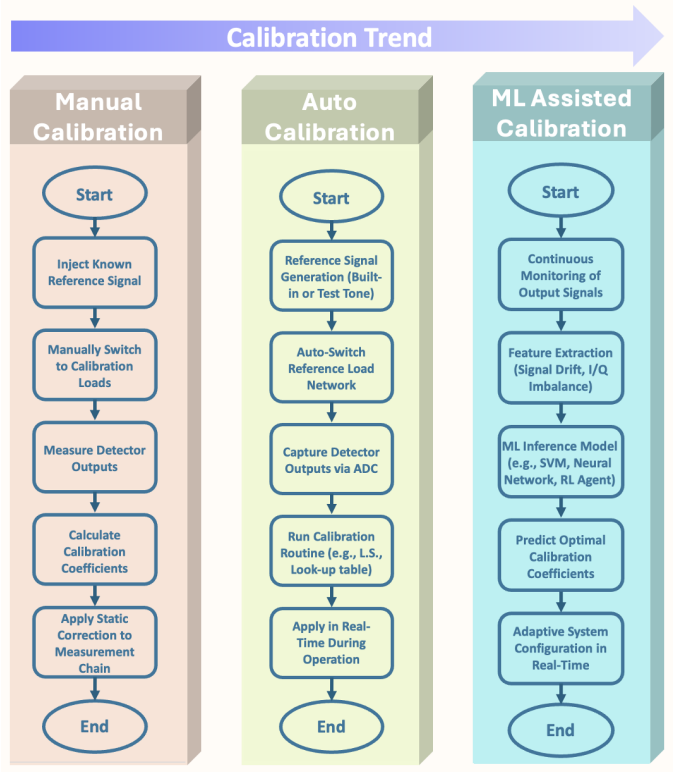

Figure 2.6 Flowchart illustrating trends in calibration, linearity enhancement, and ML integration in multi-port systems, from traditional reference-based methods to AI-driven adaptive compensation.

erence signals internally, auto-switching load networks, capturing outputs through ADCs, and running calibration routines (e.g., least squares or look-up tables), allowing real-time corrections. The rightmost column represents ML Assisted Calibration, where the system continuously monitors output signals, extracts features like signal drift or I/Q imbalance, and uses ML inference models (e.g., SVMs, neural networks, or reinforcement learning agents) to predict optimal calibration parameters. These are then applied adaptively in real time, enabling highly dynamic and intelligent calibration without human intervention. The figure emphasizes a clear calibration trend toward increased automation, intelligence, and real-time adaptability.

Once calibration is established, another critical hardware limitation arises—linearity. Section 2.4.2 explores how multi-port systems address nonlinearity through biasing, design choices, and digital compensation.

2.4.2 Linearity Enhancement and Diode Biasing Techniques

Linearity remains a fundamental design concern in multi-port RXs and TRXs, especially those employing nonlinear detection mechanisms such as Schottky or zero-bias diodes. Nonlinearities in these detectors can introduce intermodulation distortion, DC offsets, and degradation of EVM, which severely affect system performance in broadband or high-order modulation scenarios. Therefore, maintaining signal fidelity across a wide dynamic range demands both hardware and algorithmic techniques for linearity enhancement.

In passive multi-port RXs, the selection and biasing of square-law detectors are particularly critical. These detectors exhibit strong nonlinearity near threshold regions, leading to second-order intermodulation distortion (IMD2) and baseband asymmetry. Traditional I/Q demodulation architectures, such as those used in five-port and six-port systems, are especially vulnerable to such nonlinear effects. To address this, enhanced baseband regeneration and calibration techniques have been proposed to mitigate DC offset and suppress IMD2 artifacts [68].

A direct hardware approach involves optimizing the detector's bias point to operate within its most linear region. Recent work has introduced blind optimization algorithms that dynamically adjust diode bias based on performance metrics like EVM or total harmonic distortion (THD), enabling real-time adaptive linearization without requiring known reference signals [78]. Complementary to this, heuristic and model-based estimators have been developed to provide reliable initial bias settings, reducing the overhead of manual calibration during system setup or reconfiguration [79].

At higher frequencies—particularly in mmW front-ends—the nonlinear behavior of detectors becomes more pronounced due to greater signal attenuation and reduced dynamic headroom. To compensate, digital predistortion (DPD) techniques have been adapted to multi-port architectures. These algorithms correct for both diode-induced and RF amplification nonlinearities in SDR environments, allowing for full-duplex and concurrent transmission linearization at the baseband level [80]. Advanced DPD strategies have even been demonstrated for concurrent dual-band multi-port TXs, underscoring the demand for hybrid analog-digital linearization in future multi-band communication systems [81].

A novel contribution in this area involves the introduction of a nonlinear driver stage placed before the square-law detector to compensate for the detector's compression behavior (see Fig. 2.7) [82]. This stage introduces controlled amplitude compression at high input levels, counteracting the inherent nonlinearity of the detector's I–V curve and thereby extending the square-law operating region. Experimental validation has shown a 14-dB improvement

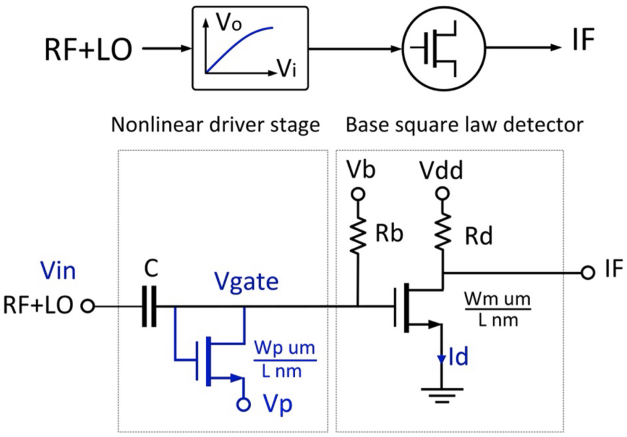

Figure 2.7 Dynamic range enhancement of power detector[71].

in the 1-dB compression point (P1dB) using a MOSFET-based implementation, with negligible power and area overhead. The technique maintains ultra-low bias currents and is fully compatible with CMOS integration. This makes it an ideal solution for six-port RXs, where power efficiency, compactness, and broadband operation are critical. Its applicability to large-scale mmW and THz RX arrays further highlights its potential for future passive RF front-end architectures.

As signal bandwidths and integration levels increase, incorporating these linearization techniques—whether through analog biasing strategies, digital correction schemes, or hybrid predistortion mechanisms—will be essential to ensuring robust multi-port RX performance in next-generation wireless systems [83, 84]. With calibration and linearity enhancement now firmly embedded in modern multi-port systems, the next section explores how these advancements have enabled the design of multifunctional front-ends capable of concurrent operation and seamless adaptability across multiple communication standards.

2.5 Emergence of Multi-functional Multi-port Systems

2.5.1 Conceptual Foundation of Concurrent Operations

The concept of multifunctionality in RF front-end design refers to the ability of a single hardware platform to support multiple communication and sensing tasks simultaneously. In the context of multi-port systems, this capability has been extended to enable concurrent operations across multiple frequency bands, modulation schemes, and application domains such as radar and wireless communication. This shift toward convergence is motivated by spec-

trum scarcity, device miniaturization, and the increasing demand for integrated sensing and communication. At the heart of this transformation lies the reconfigurable and symmetrical nature of multi-port architectures. Unlike conventional RXs that are typically tailored for a single standard or frequency range, six-port and interferometric systems inherently support broadband operation and frequency-agnostic vector detection. These properties make them ideal candidates for concurrent multi-standard TRXs.

Initial demonstrations of concurrent dual-band RXs based on six-port correlators established the feasibility of processing two independent RF signals simultaneously within the same analog front-end. These systems shared a single LO, minimizing hardware redundancy and synchronization issues [43]. Follow-up designs refined the architecture to include multiple IF chains, adaptive gain control, and digital baseband mapping for SDR compatibility [85–87].

Beyond dual-band operation, the multifunctional potential of multi-port RXs has been extended to support hybrid radar-communication systems, often referred to as RadCom platforms. These architectures allow simultaneous wireless data transmission and radar sensing using shared hardware and spectral resources [88]. By exploiting the interferometric properties of multi-port junctions, RadCom RXs can detect motion, range, or angular displacement while maintaining data connectivity, making them ideal for vehicular networks and autonomous systems.

Practical implementations have validated the theoretical potential of these architectures. Six-port RadCom platforms demonstrated flexible support for modulation schemes such as QPSK and 16-QAM. Precision range measurement systems using interferometric six-port structures achieved sub-centimeter accuracy, while enabled real-time Doppler and displacement sensing with high spatial resolution [89]. These implementations not only confirmed the feasibility of concurrent operation but also highlighted the robustness and adaptability of six-port designs in real-world scenarios [90].

Having established the architectural basis for concurrent functionality, the next subsection explores how this foundation has evolved into robust multi-standard and multi-band RXs for modern wireless platforms.

2.5.2 Development of Multi-Standard and Multi-Band Architectures

The proliferation of wireless standards—spanning Wi-Fi, LTE, 5G, UWB, radar, and satellite—has created demand for RF front-ends capable of multi-standard and multi-band operation. Multi-port systems are particularly suited for this due to their broadband impedance characteristics, vector signal processing capability, and passive, symmetric structures.

One approach to multi-band operation leveraged heterodyne six-port radar sensors, where beat frequency techniques enabled down-conversion while preserving phase for range and Doppler estimation [12]. Broadband substrate-integrated six-port front-ends were developed using multilayer waveguide structures to achieve low loss and high isolation over multi-gigahertz spans [51]. High-pass and low-pass phase shifters integrated within five-port and six-port RXs facilitated wideband operation without the need for active tuning [38].

Advanced designs introduced concurrent dual-band architectures that processed multiple RF carriers using shared or calibrated LO paths. These systems supported adaptive switching between standards like LTE and 802.11ac, using interferometric six-port front-ends with dynamic signal routing based on spectral occupancy [19, 91].

Experimental studies comparing six-port RXs with traditional zero-IF and low-IF architectures have shown superior linearity, broader bandwidth, and lower spurious response under dynamic conditions [92]. Furthermore, heterodyne implementations have demonstrated stable phase detection and high data-rate demodulation at frequencies approaching 60 GHz [93].

Recent innovations have focused on multi-band RXs capable of simultaneous demodulation across V-band and K-band using real-time calibration and even ML-assisted optimization [94–96]. The analog-domain flexibility of six-port architectures, combined with digital adaptation layers, continues to support the evolution of multi-band, multi-standard platforms.

2.5.3 Applications in Integrated Sensing and Communications

ISAC unifies sensing and data transmission within shared hardware and spectral resources. Six-port and multi-port architectures, with their ability to process amplitude and phase information over broad frequency ranges, are naturally suited for ISAC.

Initial use cases appeared in automotive radar, where six-port sensors at 94 GHz enabled accurate velocity and range estimation using passive phase-frequency discriminators [13]. These architectures were later refined using SIW technology to achieve compact form factors and improved sensitivity [97, 98]. The interferometric capabilities of six-port RXs made them suitable for environmental mapping and adaptive control systems.

The transition to ISAC emerged as six-port platforms were shown to perform both radar sensing and high-speed communication simultaneously. A software-defined six-port radar system, for instance, achieved dual-functionality by extracting target range while demodulating embedded communication signals [42]. Other implementations used time-division or spectral multiplexing to support concurrent radar and communication at 77 GHz, applicable to vehicular and industrial scenarios [11].

A recent contribution introduces an interferometric RX architecture capable of simultaneous data reception, AoA estimation, and polarization detection within a single front-end [99]. As shown in Fig. 2.8, utilizing multi-port interferometric structures, the design achieves low power consumption and avoids traditional mixers by performing analog-domain signal processing. A fabricated Ka-band prototype demonstrates accurate demodulation of QAM signals alongside precise AoA and polarization detection. This multifunctional approach aligns closely with the goals of ISAC, offering a compact and energy-efficient solution for future wireless systems requiring joint communication and sensing capabilities.

Recent systems have demonstrated advanced ISAC capabilities, such as polarization diversity and analog beamforming, all enabled through six-port interferometric designs [14, 15, 100–122]. These features, when combined with low-latency software-defined layers, make multi-port ISAC platforms particularly suitable for edge-AI environments like smart cities, V2X communication, and autonomous robotics.

2.5.4 Challenges in Concurrent Operations

Despite their advantages, concurrent-operation multi-port systems face several challenges. Signal isolation is a primary concern, especially when radar and communication functions share adjacent bands. Strong radar reflections may saturate detectors or ADCs, causing distortion in weaker communication signals.

Interferometric radar systems also face limitations in Doppler accuracy when the target's radar cross-section varies with angle, introducing bias in range estimation. Resource allocation—deciding how to divide waveform energy, time, or frequency between sensing and communication—is limited by the analog nature of signal decomposition in multi-port architectures. Hybrid analog-digital control layers are often necessary to coordinate concurrent functions. Thermal drift, parasitic coupling, and device mismatches can further degrade performance in broadband settings, especially under mobile or rapidly changing conditions. While calibration techniques exist, their speed and robustness remain areas of active research. Finally, regulatory compliance imposes constraints on shared-spectrum usage, requiring adherence to coexistence protocols and emission standards.

Nevertheless, the analog efficiency, reconfigurability, and compactness of multi-port systems continue to make them strong candidates for multifunctional RF platforms. Emerging solutions are expected to incorporate AI-driven calibration and intelligent waveform design to overcome existing limitations and unlock the full potential of concurrent multi-port architectures.

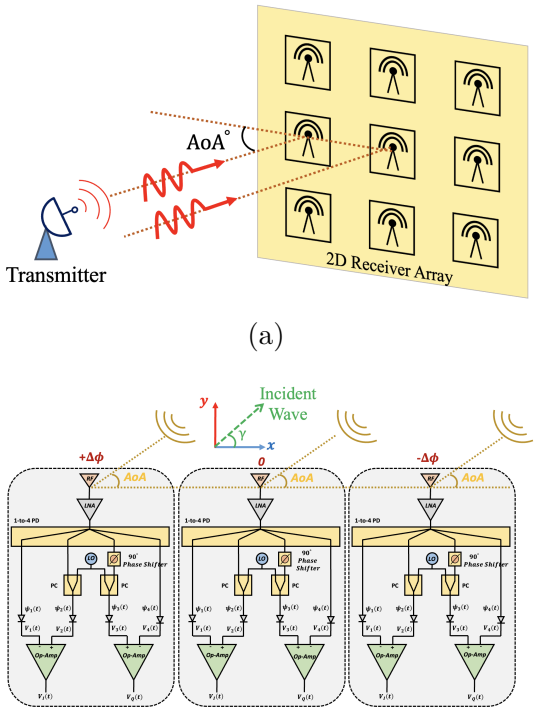

Figure 2.8 (a) Conceptual diagram of the proposed multifunction interferometric receiver architecture for simultaneous data reception, AoA detection, and polarization detection. (b) Block diagram of the proposed multifunction interferometric receiver architecture (PD is short for Power Divider and PC for Power combiner) [90].

With a full exploration of multifunctionality and concurrent operation complete, the next section introduces the paradigm of analog reconfigurability and their role in the evolution of multi-port front-ends.

2.6 Toward Programmability: Virtual Receiver and Transceiver Matrices (VRM & VTM)

2.6.1 Conceptual Framework of VRM and VTM

The evolution of multi-port RF front-ends has recently progressed toward a new design paradigm: analog programmability. This shift is embodied by the concepts of the VRM and VTM, which extend the functionality of passive RF hardware through dynamic signal routing, enabling simultaneous and selective processing of multiple signal paths. Unlike traditional fixed multi-port systems, VRM and VTM architectures can virtually reconfigure port mappings and spatial signatures without physical rewiring or frequency hopping. One

of the earliest backgrounds works that paved the way for this direction was the “Spatially Distributed Multi-Input Interferometric RX for 5G Wireless Systems and Beyond" [118].

In that work, the authors proposed a low-cost, low-complexity direct conversion RX architecture that replaced the conventional six-port junction with a spatially distributed array of four antennas, exploiting interferometric correlations for coherent demodulation. By combining the received signals with a shared LO through passive power dividers and processing them via power detectors, the system achieved full I/Q regeneration without mixers or complex RF circuitry. This architecture demonstrated successful demodulation of BPSK, QPSK, QAM-16, and QAM-32 signals, with experimental results validating simulation predictions. The approach preserved the benefits of six-port RXs while introducing spatial diversity and hardware simplification—principles that later influenced the conceptual development of VRM architectures.

Building on such spatially distributed interferometric concepts, the VRM framework generalizes the idea into a reconfigurable, two-dimensional lattice of interferometric unit cells that can be toggled in real time among active-RX, passive-sensor, or dummy states [20, 119]. In contrast to fixed-port or static-array configurations, any subset of two, four, or more cells can be dynamically grouped to form a “floating” virtual RX channel precisely matched to the incident signal’s AoA, polarization, or frequency, thereby unlocking a far greater number of spatial degrees of freedom than conventional arrays. This flexible cell allocation allows the system to execute multiple functions simultaneously—such as high-speed data reception, localization, and environmental sensing—while unused cells consume negligible power, preserving a low-energy footprint. Since signal demodulation is performed entirely in the analog domain through phase-difference processing, the matrix inherently supports advanced analog-domain operations, including adaptive beamforming, spatial filtering, and spectrum analysis, all maintained over wide operational bandwidths.

Advancing the VRM paradigm, the VTM integrates both transmission and reception capabilities into each unit cell, thereby transforming the lattice into a fully bidirectional architecture with concurrent sensing functionality (see Fig. 2.9) [21,120]. In this configuration, every unit cell can be reprogrammed in real time to operate in transmission, reception, or passive-sensing mode, with the allocation dynamically tailored to instantaneous signal parameters such as AoA and polarization. This fine-grained reconfigurability enables simultaneous high-precision estimation of 2D AoA and polarization while maintaining robust communication links that support high-order modulations (e.g., 64-/128-QAM). Measurements confirm that the VTM sustains low EVM and accurate sensing performance across a wide angular aperture, underscoring its suitability for multifunctional 5G/6G front-ends. By uniting reconfigurable

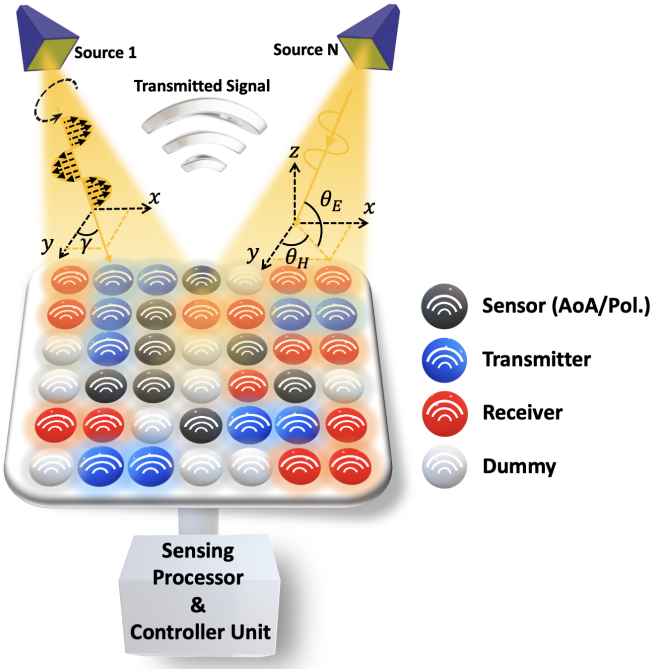

Figure 2.9 Conceptual diagram illustrating the proposed sensing and communication VTM front-end. This multifunctional system is designed to detect the AoA and polarization of arbitrary incident QAM signals, alongside facilitating both receiver (Rx) and transmitter (Tx) functions. A key feature is the multilayer LO feed network within the VTM, ensuring equal amplitude of LO signals with adjustable phases, tailored to accommodate both Rx and Tx operations. In addition, a controller unit is used to govern the dynamic operation of individual cells, allowing for an efficient power management through the activation or deactivation (dummy) of selected units [6].

hardware, wideband analog-domain processing, and intelligent control, the VTM represents a pivotal step toward compact, adaptive ISAC TRXs capable of operating reliably in complex, dynamic environments.

2.6.2 Mathematical Description of Floating Channels and I/Q Synthesis Imperfections

The VTM consists of a two-dimensional grid of passive reception cells that interfere incident electromagnetic waves through a fixed multi-port combining network. Each cell re-radiates or detects a portion of the impinging field, while the inter-cell phase differences—originating solely from the wave's angle of arrival—determine the spatial selectivity. No active phase shifters are required.

Floating-Channel Formation

Consider a narrowband plane wave of complex amplitude $A(\theta, \varphi)$ and carrier frequency f_c impinging on an $N_x \times N_y$ cell grid with spacings d_x and d_y. The complex voltage at cell (m, n) is

$$s_{m,n}(t) = A(\theta, \varphi)\, e^{j[2\pi f_c t + \psi_{m,n}(\theta,\varphi)]}, \tag{2.1}$$

where

$$\psi_{m,n}(\theta, \varphi) = k(m d_x \sin\theta\cos\varphi + n d_y \sin\theta \sin\varphi)\,, \quad k = \tfrac{2\pi}{\lambda}, \tag{2.2}$$

is the geometric phase determined by the wave incidence and cell position. Stacking all $M = N_x N_y$ cell responses into $\mathbf{s}(t) = [s_1(t), \ldots, s_M(t)]^T$ gives

$$\mathbf{s}(t) = A(\theta, \varphi) e^{j2\pi f_c t}\, \mathbf{d}(\theta, \varphi), \tag{2.3}$$

with array manifold $\mathbf{d}(\theta, \varphi) = [e^{j\psi_1}, \ldots, e^{j\psi_M}]^T$.

A passive combining matrix $\mathbf{W} \in \mathbb{C}^{N_v \times M}$ maps these M cell voltages to N_v detector outputs (termed *floating channels*) as

$$\mathbf{y}(t) = \mathbf{W}\mathbf{s}(t) = A(\theta, \varphi) e^{j2\pi f_c t}\, \mathbf{g}(\theta, \varphi), \tag{2.4}$$

where $\mathbf{g}(\theta, \varphi) = \mathbf{W}\mathbf{d}(\theta, \varphi)$ is the effective VTM manifold. For the kth output port,

$$y_k(t) = A(\theta, \varphi) e^{j2\pi f_c t}\, H_k(\theta, \varphi), \quad H_k(\theta, \varphi) = \sum_{i=1}^{M} w_{k,i} e^{j\psi_i(\theta,\varphi)}, \tag{2.5}$$

Here, $w_{k,i} \in \mathbb{C}$ denotes the complex coupling coefficient between the ith reception cell and the kth floating channel, defined by the passive combining network at the carrier frequency. It corresponds to the network transmission coefficient $S_{k,i}(f_c) = |S_{k,i}| e^{j\phi_{k,i}}$, where $|S_{k,i}|$ represents the power-division ratio and $\phi_{k,i}$ the fixed phase delay of the path connecting cell i to detector k. The matrix $\mathbf{W} = [w_{k,i}]$ therefore embodies the interferometric transfer function of the VTM and determines how the distributed cell responses are recombined to form the floating channels.

I/Q Synthesis Imperfections

Each floating channel is subsequently down-converted by an in-phase/quadrature (I/Q) detector that may exhibit gain and phase imbalance. Let $\epsilon_{A,k}$ denote the relative amplitude error and $\delta_{\phi,k}$ the quadrature phase deviation for channel k. The complex baseband voltage

is

$$r_{bb,k}(t) = (1+\epsilon_{A,k})e^{j\delta_{\phi,k}/2}y_k(t) + \eta_k e^{-j\delta_{\phi,k}/2}y_k^*(t), \tag{2.6}$$

where $\eta_k = \frac{1-\epsilon_{A,k}}{1+\epsilon_{A,k}}e^{-j\delta_{\phi,k}}$ represents the image-leakage coefficient. In vector form,

$$\mathbf{r}_{bb}(t) = \mathbf{\Phi}_{IQ}\mathbf{y}(t) + \boldsymbol{\eta}\mathbf{y}^*(t), \tag{2.7}$$

with diagonal matrices $\mathbf{\Phi}_{IQ} = \mathrm{diag}\{(1+\epsilon_{A,k})e^{j\delta_{\phi,k}/2}\}$ and $\boldsymbol{\eta} = \mathrm{diag}\{\eta_k\}$. These imperfections occur after the passive combination and do not modify the VTM's inherent spatial response.

Relations to Multifunction Performance

(1) Data Communication: The image term $\eta_k y_k^*(t)$ distorts the QAM/OFDM constellation. The corresponding image-rejection ratio (IRR) and error-vector magnitude (EVM) are

$$\mathrm{IRR}_k = \frac{1+\epsilon_{A,k}^2+2\epsilon_{A,k}\cos\delta_{\phi,k}}{1+\epsilon_{A,k}^2-2\epsilon_{A,k}\cos\delta_{\phi,k}}, \qquad \mathrm{EVM}_k \approx \sqrt{\tfrac{|\eta_k|^2}{1+|\eta_k|^2}}. \tag{2.8}$$

(2) Parametric Sensing: For multiple targets $(\theta_\ell, \varphi_\ell)$ with powers σ_ℓ^2, the ideal covariance is

$$\mathbf{R}_y = \sum_\ell \sigma_\ell^2 \mathbf{g}(\theta_\ell,\varphi_\ell)\mathbf{g}^H(\theta_\ell,\varphi_\ell) + \sigma_n^2\mathbf{I}, \tag{2.9}$$

where σ_n^2 is the noise variance. I/Q mismatch perturbs it as

$$\mathbf{R}_{bb} = \mathbf{\Phi}_{IQ}\mathbf{R}_y\mathbf{\Phi}_{IQ}^H + \boldsymbol{\eta}\mathbf{R}_y^*\boldsymbol{\eta}^H + \sigma_n^2\mathbf{I}, \tag{2.10}$$

slightly biasing the signal and noise subspaces and reducing angular-resolution accuracy.

(3) Wireless Power Transfer: For a single plane wave, the available power at the kth detector port is

$$P_k(\theta,\varphi) \propto |H_k(\theta,\varphi)|^2 = \Big|\sum_{i=1}^{M} w_{k,i}e^{j\psi_i(\theta,\varphi)}\Big|^2. \tag{2.11}$$

Hence, the harvested or rectified power follows the spatial interference pattern determined by the geometry-induced phases.

Discussion

In the VTM, all inter-cell phase relations originate from the incident wavefront, while $\mathbf{W}$ defines a fixed interferometric mapping that creates multiple floating channels. I/Q imperfections arise after this analog combining stage and primarily influence demodulation fidelity

or covariance accuracy, without altering the underlying angular selectivity. The same passive VTM manifold can therefore support high-fidelity communication, precise parametric sensing, and direction-selective power transfer within a single hardware platform.

2.6.3 Simultaneous Demodulation of Co-Frequency Signals via VRM

One of the most compelling implementations of the VRM demonstrates analog beam combination using simultaneous incident waves at a common carrier frequency (see Fig. 2.10) [22]. This work showcases the VRM's ability to enable concurrent reception and demodulation of multiple signals operating on the same frequency—a task that typically requires separate frequency channels or complex digital processing in conventional RXs. The VRM achieves this through a spatially distributed two-dimensional array of unit-cells, each composed of an antenna, LNA, 90-degree hybrid coupler, and differential power detectors, all coherently driven by a shared LO. By leveraging differences in the AoA of incoming signals, the system selectively activates specific combinations of unit-cells to extract either the in-phase or quadrature components of each signal. This analog interferometric approach, combined with precise control over phase shifts induced by AoA variations, allows the VRM to reconstruct and demodulate the individual I/Q components of multiple same-frequency signals in parallel.

To experimentally validate this concept, the authors developed and tested a 3×5 VRM prototype operating at Ka-band for 5G applications. The prototype successfully received and demodulated two distinct QPSK signals transmitted simultaneously at the same carrier frequency but arriving from different AoAs (60° and 75.5°). The resulting measurement showed clear constellation diagrams for both signals, with an EVM of less than 10%, confirming the effectiveness of the proposed architecture. This work marks a significant step forward in RF front-end design, introducing a scalable and reconfigurable RX solution that supports both high-capacity communication and real-time sensing. As future wireless systems such as 6G demand higher spectral efficiency and integrated multifunctionality, the VRM stands out as a promising architecture to meet those needs.

2.6.4 Application Scenarios: ISAC and 4D Automotive Sensing

VRM and VTM architectures are particularly valuable in ISAC systems, where rapid switching between communication and radar tasks or simultaneous dual-mode operation is required. These systems allow a single front-end to adaptively track motion, estimate position, and maintain communication—all within a shared analog pipeline.

One notable demonstration of this concept involves a 4D joint sensing-communication system

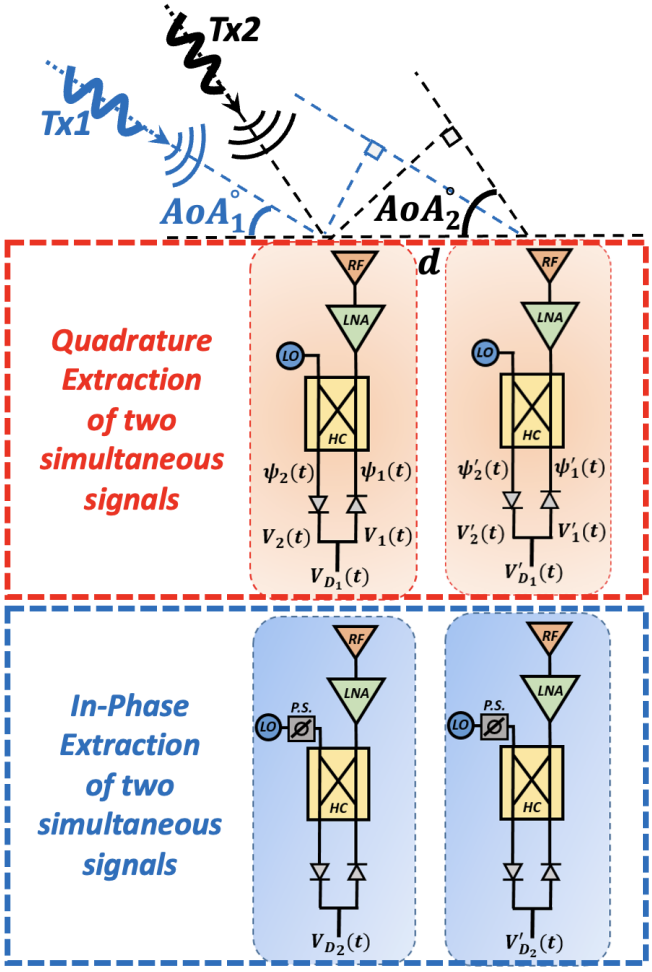

Figure 2.10 Block diagram of 2D VRM unit-cells, each containing an antenna, a LNA, a 90-degree hybrid coupler, and two power detectors connected in a differential and balanced form. Two different signals at the same carrier frequency are incident on the VRM unit-cells with different AoAs, simultaneously. (P.S. and HC are short for phase shifter and hybrid coupler, respectively) [7].

that integrates real-time inter-vehicle data exchange with high-resolution sensing of range, velocity, azimuth, and elevation (see Fig. 2.11) [23]. Using a dynamically reconfigurable matrix of TRX cells, the system activates specific units based on the environment and number of detected targets. Each cell is capable of both analog demodulation and interferometric sensing, enabling efficient extraction of in-phase and quadrature components of communication signals while simultaneously supporting precise AoA detection. This dual functionality, achieved through passive hardware and spatial diversity, highlights the potential of VRM/VTM-based platforms to replace bulky and power-hungry conventional architectures—paving the way for compact, multifunctional, and intelligent wireless front-ends suited for next-generation au-

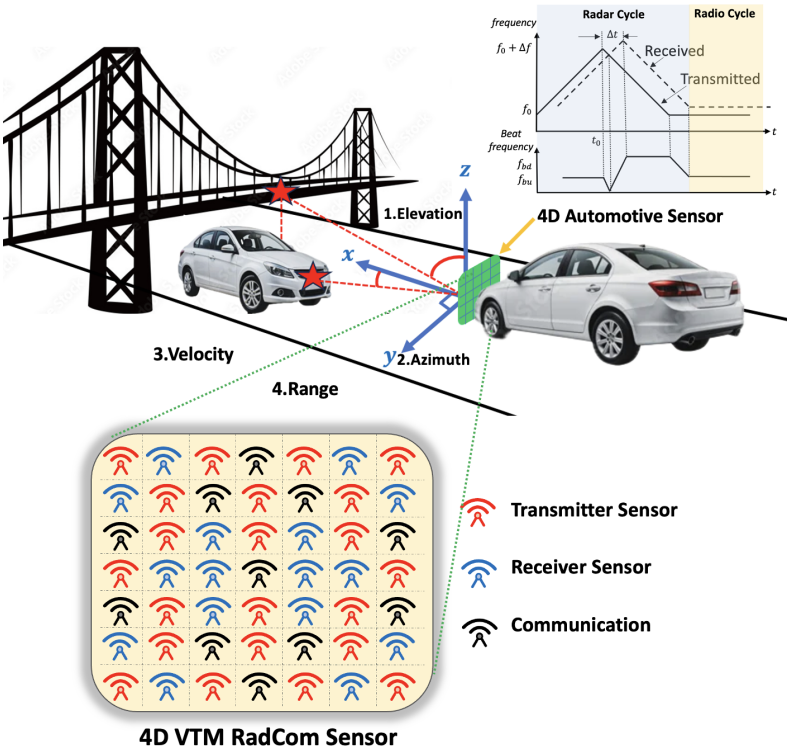

(a)

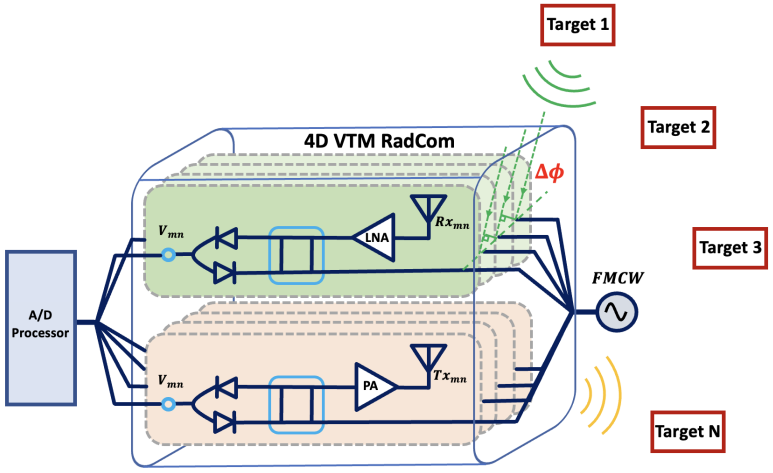

(b)

Figure 2.11 (a) Conceptual representation of the 4D automotive RadCom sensor, showcasing its ability to measure range, velocity, azimuth, and elevation angles. The integration of radar and communication functions is achieved through the coordinated radar and radio cycles of the transmitted signal in the VTM architecture. (b) Schematic diagram of VTM RadCom cells, comprising a hybrid coupler, a pair of differential power detectors, an antenna, a LNA, and a PA, all interconnected with a processing unit [8].

tonomous and connected systems. The passive and instantaneous nature of the VTM matrix allows for robust performance in high-speed, cluttered environments with minimal calibration overhead.

As spectrum sharing and system convergence intensify, VRM and VTM architectures are poised to become foundational elements in reconfigurable, cognitive, and multifunctional wireless front-ends. To realize their full potential, the next evolution lies in Machine-Learning-Enabled VTM architectures, where data-driven algorithms enable real-time reconfiguration and intelligent decision-making—an emerging paradigm explored in the following section.

2.7 Machine-learning-enabled VTM: A Futuristic Paradigm

The evolution of wireless front-end architectures has reached a pivotal stage with the development of VTM systems. As wireless environments grow increasingly dense, dynamic, and multifunctional, the fusion of ML and artificial intelligence (AI) with VTM architectures promises a transformative shift toward intelligent, autonomous RF platforms. This section outlines the emerging vision of Machine-Learning-Enabled VTM (ML-VTM), distinguishing it from prior ML applications in multi-port and six-port systems, and presents the conceptual framework, control logic, and design elements envisioned for this next-generation paradigm.

2.7.1 From ML-Assisted Multi-Port Systems to Intelligent ML-VTM

ML has already made significant contributions to traditional multi-port and six-port systems, particularly in areas such as calibration, impairment compensation, and adaptive demodulation. For instance, ANNs have been employed to map complex nonlinearities in direction-finding RXs, outperforming static calibration tables under hardware variability and noise [75]. Similarly, support vector machines and time-delay neural networks have been used to model amplitude and phase imbalances in wideband RXs, enhancing robustness in mobile and cognitive radio platforms [69].

In six-port architectures, ML techniques have enabled real-time adaptation of QAM constellation decision boundaries to mitigate distortion, resulting in improved EVM and BER performance [71]. Machine-learning-based DPD frameworks have also leveraged multi-port sensing for closed-loop linearization of high-frequency amplifiers [121]. Additionally, AI-driven resource management and beam control have been proposed for multi-channel systems to ensure spectral coexistence and dynamic channel allocation [122].

However, these implementations primarily treat ML as an auxiliary layer—an enhancer for static hardware configurations. In contrast, ML-VTM envisions a fundamentally different

model: one in which intelligence is deeply embedded into the physical architecture, enabling real-time, environment-aware reconfiguration of the TRX matrix itself. Rather than optimizing around fixed hardware constraints, the ML-VTM platform adapts its own structure and function continuously in response to changing signal, user, and environmental conditions.

2.7.2 Required Parameters and ML Data Inputs

ML-VTM systems rely on a rich set of real-time and historical data to support intelligent operation. Critical parameters include channel state information (CSI), Doppler spread, signal correlation, and multipath profiles. Environmental data such as user mobility, obstacle mapping, and RF interference patterns provide additional context. Internally, hardware-specific metrics—temperature fluctuations, gain settings, switching latency—must be monitored. Performance indicators like instantaneous SNR, EVM, BER, and spectral efficiency define the optimization objectives, while mission-specific goals (e.g., sensing resolution or communication throughput) guide function prioritization and resource allocation.

2.7.3 Software and Hardware Architecture of ML-VTM

The ML-VTM framework is structured across three key architectural layers. At the foundation is a matrix of reconfigurable RF unit cells, each capable of acting as a TX, RX, passive sensor, or dummy load. These cells integrate tunable mixers, programmable gain amplifiers, and phase shifters. Above this lies a cognitive control layer, powered by reinforcement learning and transformer-based models, which dynamically orchestrates the array's topology based on system objectives and real-time feedback. At the top level, an edge intelligence layer supports distributed inference and federated learning, allowing geographically dispersed VTMs to share model updates and operate collectively without centralized control.

This architecture is conceptually illustrated in Fig. 2.12, which highlights the dual-plane organization of ML-VTM systems. The physical layer, or hardware plane, comprises a reconfigurable VTM cell composed of an antenna, linear interferometric RF front-end, and baseband interface. These components perform the core analog processing required for sensing and communication, synchronized via RF and IF interfaces.

On the control and software layer, or cognitive plane, a ML core performs real-time mode classification, deciding whether the system operates in communication, sensing, or hybrid mode. Based on this classification, communication mode handles tasks such as beam selection and reconfiguration policy enforcement, while sensing mode executes AoA/Doppler estimation, calibration compensation, and data fusion. Both modes interact with a context-

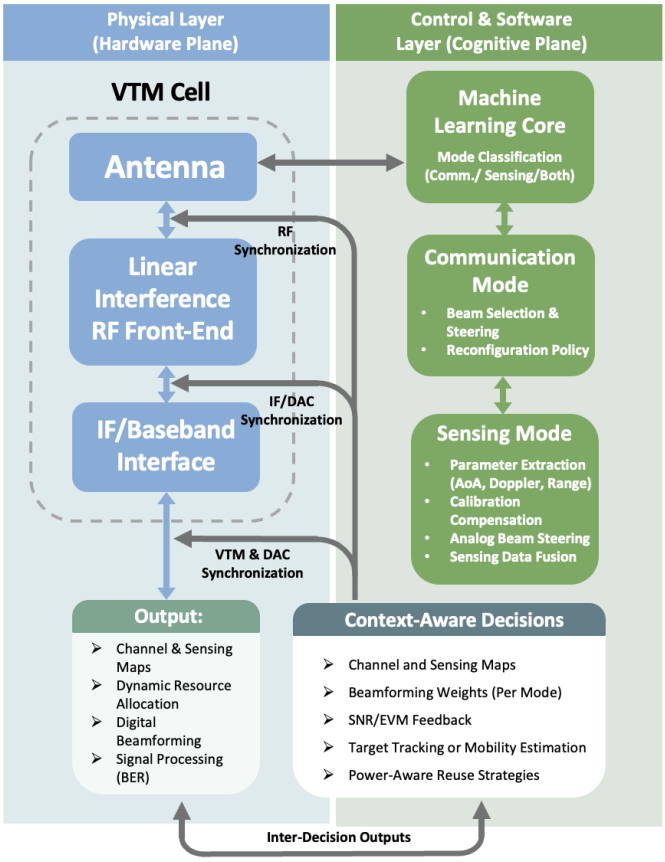

Figure 2.12 Conceptual architecture of a Machine-Learning-Enabled Virtual Transceiver Matrix (ML-VTM) system. The design integrates a physical-layer VTM cell with a cognitive-layer control engine, enabling dynamic mode classification, real-time beam control, and environment-aware sensing-communication adaptation. Outputs such as channel maps, beamforming weights, and resource allocation decisions are derived through iterative feedback across hardware and software planes.

aware decision engine that refines system behavior by feeding back outputs such as beamforming weights, channel maps, and mobility estimation data. This layered architecture enables continuous learning and intelligent adaptation, allowing ML-VTM systems to evolve and optimize their operation in response to changing environments and mission demands.

2.7.4 Functional Behavior at the Unit-Cell Level

In large-scale arrays, individual unit cells assume context-dependent roles dictated by AI inference. Some act as active sensing-communication TRXs, others as passive detectors extracting environmental features such as AoA or Doppler signatures, while certain cells remain inactive to minimize power or assist in beam shaping. ML models govern these transitions, optimize spectrum allocation, control beamforming patterns, and manage joint sensing-communication scheduling.

2.7.5 Conceptual Illustration and System-Level Vision

This forward-looking concept is illustrated through several envisioned models. One depicts a reconfigurable hexagonal VTM grid with real-time AI-determined cell roles. Another shows an AI control unit integrating spectrum analysis, mission objectives, and hardware feedback into a unified decision engine. A third highlights distributed intelligence across VTM arrays, enabling collaborative, low-latency inference via federated learning mechanisms.

2.7.6 Outlook: Why ML-VTM Defines the Future

Machine-Learning-Enabled VTM marks a convergence of adaptive signal processing, programmable hardware, and AI-driven intelligence. It facilitates autonomous, context-aware operation across diverse conditions, achieving real-time spectrum agility and multifunctionality. ML-VTM systems optimize energy efficiency by deactivating unnecessary hardware paths and reconfiguring analog circuitry based on environmental conditions and application goals. Moreover, they decouple hardware complexity from functional scalability by shifting intelligence to updatable software models—enabling continuous evolution over time.

As wireless systems migrate toward ISAC systems, ML-enabled VTMs are poised to play a foundational role in future RF architectures. Their ability to learn, adapt, and reconfigure at fine spatiotemporal granularity makes them ideal for next-generation 6G systems and beyond. While previous ML applications in multi-port systems laid important groundwork, ML-VTM offers a fundamentally new path—one where intelligence is not just an enhancement, but an intrinsic part of the RF fabric. This paradigm shift opens new avenues for innovation in

intelligent wireless front-ends.

Finally, while VRM and VTM represent a new frontier in analog-domain reconfigurability, they are complemented by emerging trends in passive reconfigurable platforms, such as RIS. These systems offer additional degrees of control over the propagation environment and will be discussed in Section 2.8.

2.8 Reconfigurable Intelligent Surfaces (RIS)-Enabled Receivers

2.8.1 Introduction to RIS and Metasurfaces

RIS represents a transformative approach to wireless system design, where the propagation environment itself is rendered programmable. Comprising arrays of passive or semi-passive unit cells—often implemented as metasurfaces—RIS can reflect, absorb, or refract incident electromagnetic waves with controlled phase and amplitude responses. Unlike conventional RF components, RIS structures operate without active RF chains, making them energy-efficient and scalable across mmW and THz frequencies. (see Fig. 2.13)

RIS systems are typically embedded with tunable elements such as varactors, PIN diodes, CMOS switches, or liquid crystals, which are externally programmed to create dynamic spatial transformations of the wavefront. These surfaces can be tailored to perform beam steering, focusing, spatial filtering, and even polarization conversion—all without generating additional noise or requiring active signal processing [24, 25].

In recent years, RIS has emerged as a key enabler of beyond-5G and 6G wireless technologies, offering a new layer of spatial control and spectrum reuse [123–134]. Its compatibility with existing TRX infrastructure, combined with low-cost implementation and channel shaping capabilities, positions RIS as a powerful tool for link enhancement, energy focusing, and coverage expansion.

2.8.2 Passive and Semi-Passive RIS-Based RF Front-Ends

RIS-based RXs can be broadly categorized into passive and semi-passive implementations. Passive RISs rely entirely on externally incident electromagnetic waves, without incorporating any active amplification or energy harvesting mechanisms. These configurations are typically controlled through low-speed digital interfaces and are optimized for low-latency, low-power applications.

Semi-passive RISs, in contrast, integrate amplifying or phase-reconfigurable components that enhance link robustness, extend the reflection phase range, and improve adaptability to dy-

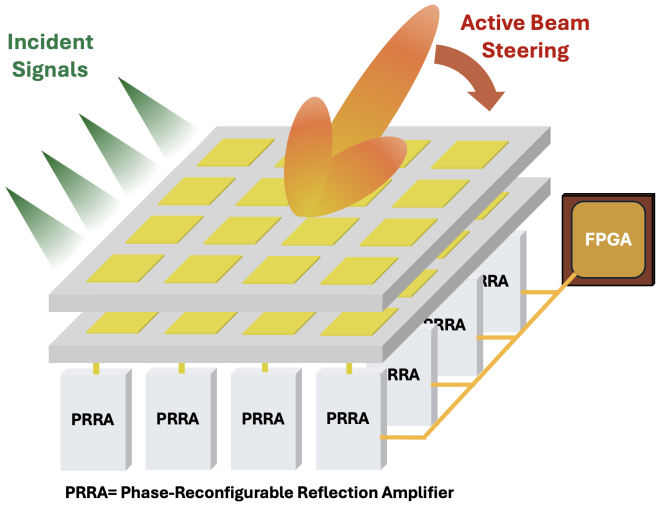

Figure 2.13 Conceptual illustration of an active RIS with beam steering and amplification capability.

namic environments. For instance, CMOS-integrated RIS tiles have demonstrated real-time beam reconfiguration with precise angle control at mmW and THz frequencies [135]. Active RIS variants have also employed reflection amplifiers to boost SNR and compensate for severe path loss, especially in indoor and non-line-of-sight conditions [136]. Recent prototypes of RIS-assisted RXs have incorporated energy harvesting modules, cognitive sensing elements, and on-board feedback sensors to enable self-sustaining operation and context-aware adaptation [137].

RIS-assisted direction-finding systems have utilized reconfigurable reflection patterns to emulate virtual phased arrays, achieving enhanced angular resolution without increasing hardware complexity [138]. In multiuser MIMO scenarios, RISs can assist in pre-shaping the wireless channel, enabling constructive signal combining at the multi-port front end. Such configurations reduce the burden on RF circuitry and simplify beamforming—particularly in the THz regime, where hardware constraints are especially stringent [139].

2.8.3 Synergies Between RIS and VTM Concepts

Although fundamentally different from multi-port analog front-ends, RIS shares philosophical and architectural synergies with VRM and VTM systems. Both paradigms aim to achieve functional reconfiguration with minimal power overhead and maximal spectral reuse.

One promising direction is the hybrid integration of RIS with VRM/VTM platforms, where the RIS acts as a programmable spatial front-end and the VRM/VTM serves as an analog

Table 2.1 Comparative Assessment Summary

Technology	Complexity	Calibration	Frequency Range	ISAC Capability	Reconfigurable
Six-Port	Low	Moderate	Excellent	Strong	Fixed
VRM–VTM	Medium	Moderate	Excellent	Excellent	High
RIS (Passive)	Low–Medium	Low	Moderate	Moderate	High
RIS (Active)	High	High	Limited by Design	High	High

baseband processor. This co-design enables joint control over the wireless channel and the RX chain, opening new possibilities for low-latency beam adaptation, spatial modulation, and collaborative ISAC.

Furthermore, RISs can assist in enhancing the spatial selectivity of VRM systems by pre-aligning reflected waveforms to optimal matrix paths. Conversely, VTM systems can exploit RIS feedback to adapt their TRX matrix modes in response to channel dynamics.

As RIS technology matures, its role will increasingly shift from being a passive enhancer to becoming a fully programmable RF boundary interface—complementing the core processing capabilities of virtualized multi-port RXs.

Having explored the capabilities of both VRM/VTM and RIS systems, the next section provides a comparative performance analysis of all major front-end architectures covered in this review.

2.9 Performance Benchmarking and Comparative Assessment

To evaluate the evolution and practical applicability of multi-port front-end architectures, including Six-Port, VRM/VTM, and RIS-enabled systems, it is essential to benchmark their performance across multiple dimensions. These include architectural complexity, calibration effort, frequency scalability, and their combined sensing and communication capabilities.

Table. 2.1 provides a comparative overview of four leading RF front-end technologies—Six-Port, VRM-VTM, Passive RIS, and Active RIS—based on their complexity, calibration needs, frequency range, ISAC capability, and reconfigurability. Six-Port systems offer low complexity and strong ISAC performance but are limited by fixed architectures. VRM-VTM systems balance moderate complexity and calibration with excellent performance in frequency coverage and multifunctionality, offering high reconfigurability. Passive RIS devices excel in reconfigurability with minimal calibration but are limited in frequency flexibility and ISAC integration. Active RIS, while the most complex and calibration-intensive, promises high

ISAC capabilities and dynamic adaptability, albeit with frequency limitations inherent to their active design.

Table. 2.2 summarizes representative implementations of multi-port and reconfigurable RF front-end technologies reported in the 2020s. The comparison highlights a broad spectrum of operation frequencies ranging from sub-GHz RFID and IoT systems up to 300 GHz terahertz (THz) integrated front-ends. Most reported prototypes are realized on PCB or hybrid PCB–waveguide platforms, while recent works demonstrate on-chip integration in CMOS and MMIC technologies to support higher data rates and miniaturized form factors. Data rates span from kilobits per second in low-power sensing applications to several gigabits per second for broadband THz transceivers, illustrating the scalability of multi-port architectures across vastly different communication and sensing regimes. The diversity in modulation formats—from QPSK and 16-QAM to 256-QAM and OFDM—demonstrates the increasing adaptability of these front-ends for advanced communication standards. Furthermore, the inclusion of sensing capability in recent designs signifies the convergence trend toward ISAC systems. These results collectively emphasize that multi-port, six-port, and virtual receiver/transceiver matrix architectures are not only evolving in complexity and integration level but also paving the way for next-generation programmable and multifunctional RF front-ends spanning from microwave to THz frequencies.

2.9.1 Architectural Complexity

Traditional six-port RXs offer minimal architectural complexity, relying on passive hybrid couplers, power detectors, and a calibration engine. This simplicity enables low-cost, compact implementations, particularly suitable for mmW and automotive applications. However, as functionalities are scaled—such as in dual-band, RadCom, or ISAC systems—the complexity increases non-linearly due to the need for precise symmetry and delay control.

VRM and VTM architectures retain passive core structures but introduce matrix-driven signal routing and reconfigurability. This increases design complexity, especially in analog-domain combinatory logic and timing synchronization, but provides unmatched programmability and reuse efficiency.

RIS-enabled RXs, though conceptually simple, require external control logic, reconfiguration hardware (e.g., FPGA or MCU), and increasingly sophisticated materials. When semi-passive or active components are included, their architectural burden begins to rival that of classical TRXs.

Table 2.2 Performance Summary of Multi-Port and Reconfigurable RF Front-End Technologies (2020s Journal Literature)

Ref.	Year Published	Fabrication Process	Freq. (GHz)	Data Rate	Modulation Mode	Comm. BW	Sensing
[19]	2021	PCB	3.5 & 3.8	10 MSps	256-QAM	200 MHz	NA
[91]	2021	PCB	3.6	NA	256-QAM	NA	NA
[90]	2021	PCB	24/28	4 MSps	64-QAM	300 MHz	NA
[111]	2021	PCB	2.4	NA	NA	NA	Yes
[58]	2021	MHMIC	57–64	100 kSps	QPSK	NA	NA
[112]	2022	PCB	0.915	NA	NA	NA	Yes
[15]	2022	PCB	24.5–26.5	NA	NA	NA	Yes
[89]	2022	PCB	5–6.5	15 MSps	64-QAM	150 MHz	Yes
[20]	2023	PCB	28	1 MSps	32-QAM	NA	Yes
[61]	2023	PCB	7.15	NA	NA	NA	Yes
[113]	2023	PCB	31	NA	NA	NA	Yes
[65]	2024	65 nm Chip	300	3 Gbps	32-QAM	NA	Yes
[93]	2024	PCB/Waveguide	28/30	1.2/0.8 Gbps	64/256-QAM	NA	NA
[60]	2024	MHMIC	60	500 kSps	16-QAM	NA	NA
[73]	2024	PCB	3.4 & 3.8	100 MSps	64-QAM	NA	NA
[94]	2024	PCB	5.8 & 150	240 Mbps	256-QAM	NA	Yes
[81]	2024	PCB	3.3	10 MSps & 100 MSps	256-QAM & OFDM	NA	NA
[96]	2024	PCB	24/28	5 MSps	64-QAM	NA	NA
[21]	2025	PCB	24.5–26.5	250 MSps	128-QAM	NA	Yes
[64]	2025	Waveguide/65 nm CMOS	28	1.2 Gbps	64-QAM	NA	Yes

2.9.2 Calibration Burden

Six-port systems require moderate calibration, typically through load/offset standards or dual-tone methods. Calibration frequency increases with bandwidth and integration level. In contrast, VRM/VTM platforms demand more advanced calibration schemes due to matrix routing and reconfigurable paths—often involving ML or self-correcting feedback.

RIS systems shift the calibration burden from the RX chain to the wireless channel. While the front-end may be passive, RIS-assisted systems must perform dynamic channel estimation and reflection mapping, which adds complexity at the system level.

2.9.3 Frequency Range Scalability

Six-port RXs have been implemented from sub-6 GHz to above 120 GHz using various fabrication technologies. Their broadband nature and minimal reliance on active circuitry make them highly scalable. VRM and VTM systems inherit this capability but face greater dispersion sensitivity in matrix configurations at THz frequencies. RIS technologies offer wideband manipulation in theory, but real-world performance is constrained by the material response time, unit-cell design, and parasitic coupling—especially at THz where Metasurface fabrication becomes more difficult.

2.9.4 Sensing and Communication Capabilities

Six-port and VRM/VTM systems naturally support both communication and sensing, thanks to their interferometric properties. Six-port architectures have demonstrated Doppler, range, and AoA sensing alongside communication demodulation. VRM/VTM adds dynamic reconfigurability to support concurrent ISAC.

RISs, although not originally designed as RXs, contribute by shaping the propagation environment. Their use in passive beam steering, reflection enhancement, and spatial filtering enhances both sensing accuracy and communication throughput. Combined RIS-VRM systems show potential for low-power, multifunctional operation with intelligent control.

These results show that while six-port systems remain a practical solution for compact sensing and communication, VRM/VTM and RIS technologies represent the next frontier—offering higher flexibility and integration potential at the cost of complexity and calibration effort.

With these benchmarking insights, we are now ready to explore future research directions and open challenges in the final thematic section.

2.10 Future Research Directions and Open Challenges

The continued evolution of multi-port RF front-ends will be shaped by emerging demands in ultra-broadband communication, pervasive sensing, and real-time adaptability. While six-port, VRM/VTM, and RIS-based systems have demonstrated their foundational viability, several unresolved challenges and future research opportunities remain.

Fig. 2.14 illustrates several pivotal future research directions and open challenges in the advancement of RIS-assisted RXs and related technologies. These directions reflect the growing complexity and interdisciplinary nature of next-generation wireless systems. Among the key areas identified are AI-integrated adaptive calibration and reconfiguration, which focuses on enabling real-time, intelligent adjustments for enhanced system performance. The integration of ultra-massive VTM and sub-THz front-end technologies represents another significant challenge, as it demands both scalability and high-frequency operation in compact, efficient designs.

Another emerging direction is the development of quantum-compatible and photonic multi-port systems, which aim to leverage novel physical layers and processing techniques for ultra-fast and secure communications. The co-design of RIS and VRM, along with the incorporation of hybrid RF intelligence, presents opportunities to jointly optimize control, reflection, and signal processing functionalities. Additionally, hardware-aware ISAC strategies,

combined with Size, Weight, and Power (SWaP) optimization, are identified as crucial for practical deployments—highlighted twice in the figure to emphasize their central importance.

In the following subsections, we provide a detailed discussion of each of these research directions, outlining current progress, existing limitations, and future possibilities.

2.10.1 AI-Integrated Adaptive Calibration and Reconfiguration

Future multi-port front-ends must transition toward fully adaptive systems capable of autonomous calibration and reconfiguration in dynamic environments. While neural networks and support vector machines have already demonstrated promise in reducing calibration effort, scalable implementations for real-time correction, drift compensation, and signal optimization are still under development. Future research should focus on integrating on-chip ML cores or analog neuromorphic processors directly into the front-end to minimize latency and power consumption.

2.10.2 Ultra-Massive VTM and Sub-THz Front-End Integration

Scaling to hundreds or thousands of matrix elements, as expected in ultra-massive VTM, demands new architectures that balance complexity, isolation, and calibration effort. VRM and VTM architectures are naturally suited for such scalability due to their combinatory routing potential. However, challenges remain in managing propagation dispersion, parasitic loading, and cross-channel leakage at sub-THz frequencies.

Materials and packaging for multi-port junctions above 300 GHz require innovation in low-loss waveguide structures, possibly leveraging silicon photonics or plasmonic transmission lines. Similarly, RIS designs at THz scales will need more efficient tunable materials and integration with THz -capable control electronics.

2.10.3 Quantum-Compatible and Photonic Multi-Port Systems

The convergence of RF engineering with quantum and optical domains opens another frontier. Recent studies have proposed interferometric architectures that could operate in photonic or hybrid electro-optical regimes, enabling extremely high-resolution sensing and secure communications. Multi-port analog processors could serve as quantum-compatible interfaces in environments requiring ultra-low latency and sub-photon-level sensitivity.

Moreover, photonic implementations of six-port or VRM structures could leverage wavelength-division multiplexing and high-speed phase detection, offering unprecedented levels of paral-

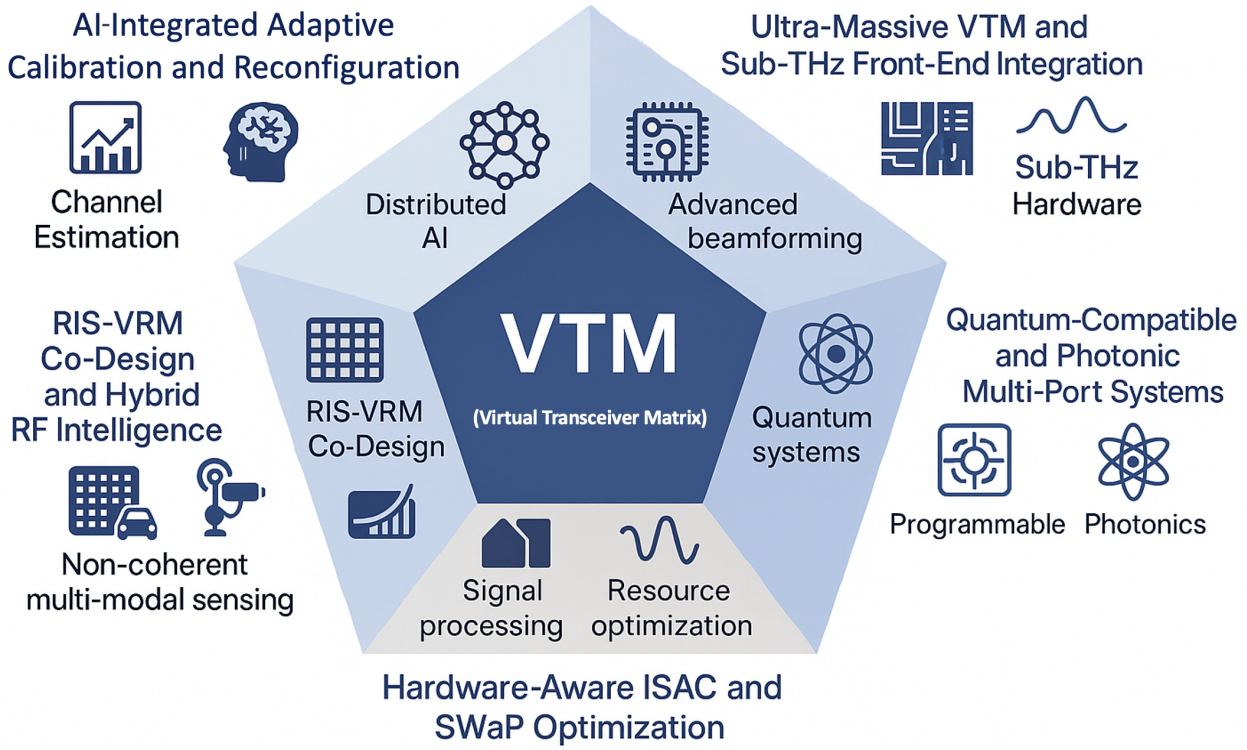

Figure 2.14 Conceptual illustration of future research directions in multi-port systems, including AI-based calibration, ultra-massive VTM, quantum and photonic integration, RIS-VRM co-design, and SWaP-optimized ISAC platforms.

lelism and bandwidth.

2.10.4 RIS-VRM Co-Design and Hybrid RF Intelligence

The synergy between RIS and VRM/VTM systems presents an exciting opportunity for distributed analog-digital cognition. A coordinated RIS-VRM network could jointly manipulate the wireless channel and RX matrix, enabling channel-aware front-end reconfiguration, multi-hop reflectivity routing, and spatial interference mitigation.

Future work should explore joint optimization frameworks where RISs adapt reflection parameters based on feedback from VRM sensing matrices, forming a closed-loop analog control system.

2.10.5 Hardware-Aware ISAC and SWaP Optimization

As ISAC platforms proliferate in UAVs, satellites, and wearable devices, constraints on SWaP will become critical. Multi-port systems must evolve to support intelligent resource allocation, low-power operation, and robust interference mitigation. Research must address analog-digital hybrid integration, packaging miniaturization, and context-aware energy control.

Moreover, new metrics for multi-functionality—such as sensing-to-communication efficiency ratio or joint utility score—should be developed to guide hardware and system optimization.

These directions underscore the fact that the future of RF front-ends is no longer bound by static hardware constraints. Instead, it will be defined by programmability, intelligence, and convergence—enabled by a new class of multifunctional, adaptive, and reconfigurable systems that integrate Six-Port, VRM/VTM, and RIS concepts.

With a vision for the future laid out, the review concludes with reflections on the technological journey and where these innovations are heading.

2.11 Conclusion and Future Outlook

The field of multi-port RF front-ends has evolved dramatically over the past four decades—from the initial conception of six-port reflectometric circuits to the emergence of complex, multifunctional, and reconfigurable analog matrix systems. What began as a passive technique for phase and amplitude detection has matured into a diverse family of RX and TRX architectures capable of supporting ISAC, dynamic beam steering, multi-band modulation, and intelligent spatial processing.

Six-port RXs have demonstrated enduring relevance by combining broadband analog performance with architectural simplicity and spectral efficiency. Their evolution into generalized multi-port configurations opened pathways for concurrent operation and dual-mode system design, particularly in software-defined and vehicular radar platforms. The transition from these fixed-port systems to reconfigurable platforms—embodied by the VRM and VTM—marks a pivotal shift. These analog matrix structures allow on-the-fly signal path adaptation, combinatory analog processing, and a higher degree of front-end programmability, aligning closely with the needs of future ISAC and AI-driven RF environments.

Complementing these RX-centric advancements, RIS redefine how the wireless channel itself can be controlled. As a novel layer of environmental reconfiguration, RIS enables spatial shaping, interference suppression, and energy-efficient communication enhancement—all achieved through programmable metasurfaces that operate in tandem with classical and virtual RF

front-ends.

This review has synthesized the historical foundations, hardware innovations, calibration trends, and application cases of multi-port front-ends while comparing their performance across key metrics. It has also laid out promising future directions, including the co-integration of RIS and VRM/VTM systems, sub-THz and photonic front-ends, and the incorporation of AI for adaptive calibration and operation.

Ultimately, the convergence of these innovations is steering the industry toward a new class of intelligent, compact, and multifunctional wireless systems—capable of fluidly transitioning between roles in communication, sensing, and environmental control. These advancements not only reflect technical progress but also redefine the very boundaries of what RF hardware can achieve in the next generation of connected and perceptive systems.

CHAPTER 3 ARTICLE 2: VIRTUAL RECEIVER MATRIX AND COMBINATORY ANALOG OPERATIONS FOR FUTURE MULTIFUNCTION RECONFIGURABLE SENSING AND COMMUNICATION WIRELESS SYSTEMS

Seyed Ali Keivaan, Pascal Burasa, and Ke Wu

Published in: *IEEE Transactions on Microwave Theory and Techniques*
Publication Date: Decemeber 20, 2022

This paper proposes and presents a topological receiver architecture, named Virtual Receiver Matrix (VRM), suitable for future smart multifunction wireless systems. This concept is devised and benefits from using combinatory analog operations with multiple distributed units in a receiver matrix or array. This mechanism of receiving data through spatially "floating" distributed virtual receiver channels, offers an unprecedented solution of providing unparalleled degrees of freedom to implement multiple functions such as data reception, angle-of-arrival (AoA) detection, radar, and imaging operations among many others in a single receiver architecture. Interestingly, the total number of possible virtual receivers from different combinations of unit-cells in a matrix is also significantly increased compared to a conventional "fixed" receiver array. Each virtual receiver, made of a combinatory set, depends on the characteristics of incoming signals and their illumination angle. A mathematical model is established and investigated for the design of unit-cells. Although a prototype of choice is studied and designed for the fifth generation (5G) wireless systems, it is anticipated that the VRM concept is applicable to the sixth generation (6G) and future wireless systems for enhancing their functionality, capacity, agility, and speed. In this paper, a multiport interferometric technique is used for each unit-cell of VRM as a proof-of-concept, however, any other receiver type that uses the phase difference of incoming signals can be deployed as the unit-cell for the realization of the VRM concept. First, experimental results of the fabricated proof-of-concept prototype for various modulation schemes including QPSK, 16-QAM, and 32-QAM are shown with data rates up to 1 mega symbol-per-second (MSps), having a maximum error vector magnitude (EVM) of 9%. Finally, a systematic scheme for 2D AoA detection using a special combination of unit-cells is proposed and demonstrated through the proposed VRM.

3.1 Introduction

Wireless communication and sensing systems have experienced and witnessed themselves tremendous innovation and transformation in recent decades. These developments are driven by ever-increasing demands of higher data rate, low latency, enormous capacity, smart agility, and super-connectivity among many others, necessitating the frequent introduction of new technologies to cope with these requirements [140]. Accordingly, high-density 5G network systems and connected devices are now proliferating across every imaginable industry and brought up a radical change in the development of the wireless system front-end architectures. The successful implementation and widespread deployment of such 5G-compatible platforms will obviously require receiving, transmitting, and processing data in a smart and multifunctional manner [141–143]. In this connection, upcoming wireless systems will benefit from multiple radios and sensors cohabitating in an autonomous or semi-autonomous way [144]. Indeed, the fusion and interplay of multi-functionalities are the foundation for future wireless intelligence [143]. Also, in anticipated robust point-to-point wireless communication systems, AoA detection becomes vital and necessary, since only a slight deviation may result in the loss of communication links [145]. Furthermore, by accurately detecting the direction of an unknown incoming signal, the signal-to-noise ratio (SNR) can be significantly improved, particularly in a multi-user wireless transmitting-receiving environment [146].

Phased-array receivers have been adopted for 5G millimeter-wave (mmW) wireless communications with high-speed data links, accurate location, and fast identification [147–149]. Their sensitivity and SNR are inherently enhanced by increasing the number of array elements, thus resulting in a high-quality demodulated digital signal and enabling high-speed data links for long-range communications [150–152]. However, they involve multiple "fixed" RF front-ends and antenna arrays. Ultra-dense networks using multiple base stations and access points based on multi-input-multi-output (MIMO) techniques have been also reported to further enhance the capacity and speed of wireless networks [153, 154]. In fact, MIMO exploits spatial multiplexing coding mechanism in multiple channels to provide high link-level gains to overcome path-related losses and enable super-high-speed data transmission [155–158]. They must typically rely on DSP to overcome inevitable interferences in the analog/RF front-end domain. This requires the implementation of high-dynamic-range and power-hungry analog-to-digital (A/D) converters and RF receiver front-ends [159]. In this connection, the existing mmW and THz receiver architectures may not be capable of the anticipated massive connections in 5G wireless systems and beyond. Hence, unparalleled futuristic solutions should be devised and considered to accommodate multi-functionalities in a smart, dense, and efficient manner with maximum capacity and speed.

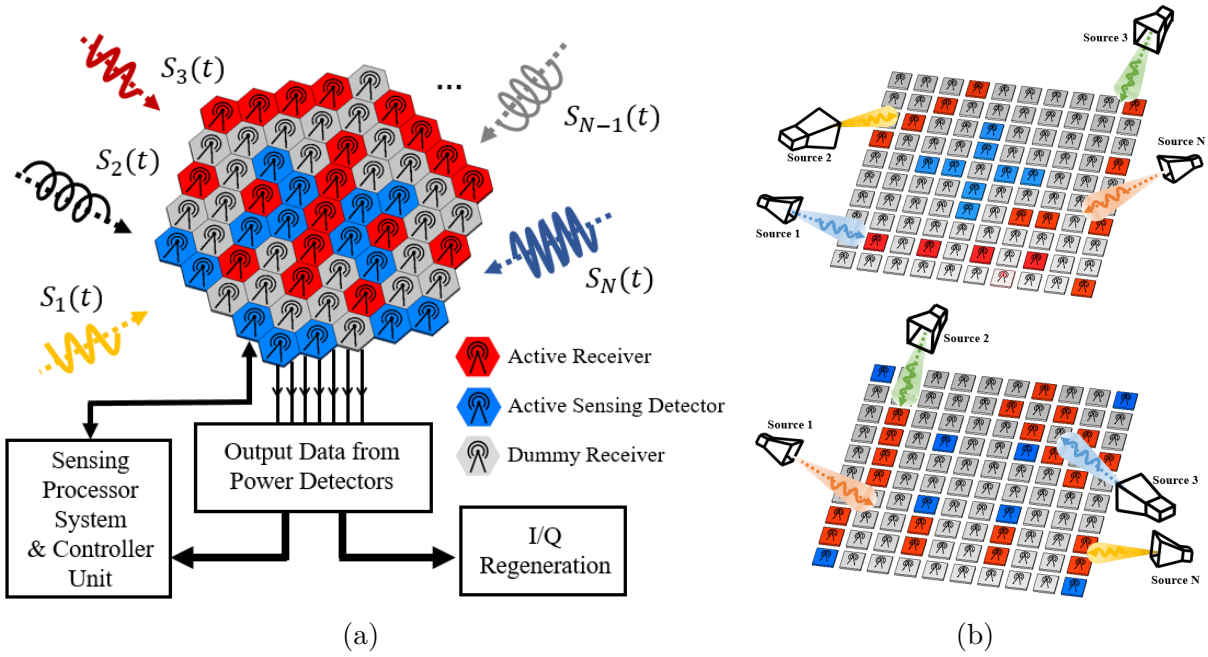

(a) (b)

Figure 3.1 (a) Illustration of VRM concept receiving from different sources with different signal properties. Three states of active receiver, active sensing detector, and dummy receivers are assigned to each unit-cell based on the sensing data and controller unit for a hypothetical scenario. The baseband output data of each unit-cell is used to regenerate demodulated signals. (b) The dynamic floating assignment of combinatory sets for creating virtual receiver channels for two different hypothetical scenarios with different sources at different incident angles. The allocation of such receiving channels depends on the AoA, polarization, and frequency of incident signals.

In this paper, a concept of Virtual Receiver Matrix (VRM) is proposed, studied, and demonstrated for the first time. As opposed to the conventional "fixed" receiver arrays, the proposed receiver makes use of "dynamic" receiving units, floating around over a two-dimensional (2D) matrix, where their states are determined based on incoming signal properties such as the AoA, polarization, and frequency. As conceptually illustrated in Fig. 3.1(a), "virtual" receiver channels are created through a dynamic floating assignment and combinatory sets of receiving units, physically distributed in the matrix. The VRM uses the phase difference of incident waves on distinct cells to extract the quadrature amplitude modulated (QAM) signals. Any combination of two or more cells is set to form a receiver, resulting in a considerable total number of possible virtual receivers in comparison with conventional receiver architectures. The most significant advantage of VRM topology compared to the conventional "fixed" receiver arrays is the number of possible virtual receivers.

The proposed virtual receiver topology would enable unprecedented degrees of freedom in implementing multiple functionalities and operations in a single receiver module, while preserving low-power consumption, particularly in a large array architecture. In parallel, the baseband recovered data from each unit cell, can be reused for different functions and data processing, therefore leading to its high capacity and efficiency of power and data management. Furthermore, the SNR can be significantly improved by using multiple cells, provided that the phase differences of distinct cells are equal with respect to the incident waves. It is worth mentioning that, the proposed topological receiver matrix also represents a good candidate for the development of large-scale THz systems, particularly for compact range and line-of-sight. Besides, as shown in Fig. 3.1(a) and (b), the geometrical architecture is not limited to a square or hexagonal matrix, and any 2D spatially distributed topology can be considered. Interferometric receiver, as a promising low-power single down-conversion to baseband or IF receiver [6,8,10,16,19,115,118,160,161], is used for the purpose of our proof-of-concept in this work. However, any other receiver type that uses the phase difference of incoming waves to demodulate a signal can be employed.

This paper presents more details and analyses of the innovative topological architecture of the VRM reported in [162]. In Section 3.2, the detailed theoretical modeling of VRM unit-cells is presented for data reception and AoA detection system. The unit-cell design of VRM and simulation results of demodulated quadrature amplitude modulation (QAM) signals and the unambiguity range of receiver are also studied. As a proof-of-concept, an experimental prototype is fabricated and measured at Ka-band for 5G multifunction applications in Section 3.3. Simulation and measurement results confirm the feasibility and viability of the proposed multifunctional VRM technique.

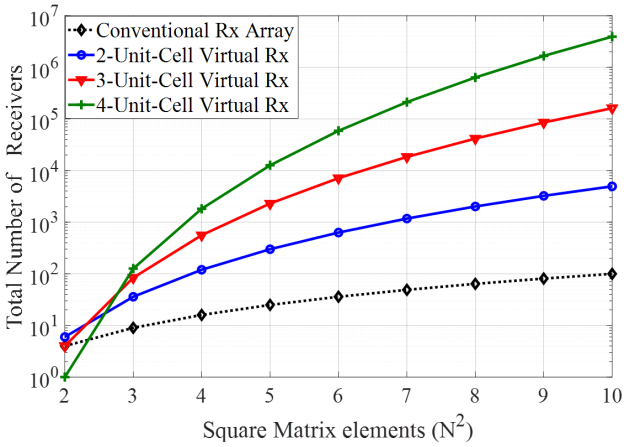

Figure 3.2 Total number of possible virtual receivers for a matrix with NxN elements in comparison with the conventional fixed receiver arrays, considering different values of p. (Each p-unit-cell can form a virtual receiver channel.)

3.2 Virtual Receiver Matrix Analysis And Modeling

Each unit-cell of VRM is controlled or managed dynamically with "activated", "sensing detector", and "dummy" states, as illustrated in Fig. 3.1(a). For any unknown incident wave, first of all, the 2D AoA detector system (detailed in Section 3.2.2) is set to determine the illumination angle, and accordingly, allocates specific unit-cells to receive data from the detected AoA. The VRM is a set of receiving units spatially distributed in a 2D array, and it uses the phase difference of incoming signals to demodulate them. By changing the incident angle of incoming signals, the states of unit-cells change, making them floating around in the VRM, as illustrated in Fig. 3.1(b). This dynamic and floating property of receivers in VRM is the prominent characteristic that makes it smart and power efficient.

The number of unit-cells that form a complete virtual receiver depends on the design principle and the received power. Based on the proposed unit-cells employed in the VRM, two scenarios can be considered depending on the power of an incoming signal compared to the injected local oscillator (LO) power. First, if the power of LO is much larger than the RF power, only two unit-cells can form a virtual receiver channel. Also, in case that RF and LO powers are approximately in the same range, four unit-cells are then combined to play the role of data reception. More theoretical investigations for the number of unit-cells that form a complete virtual receiver are explained in Section 3.2.1.

The most significant advantage of VRM compared to the conventional fixed receiver arrays is the number of possible virtual receivers. Assuming a receiver matrix with M x N elements, the total number of possible virtual receivers can be calculated using the combination of any

two or four unit-cells out of M x N elements. This is much more than the conventional case of using each unit-cell as an individual static receiver, which can be M times N receivers maximum. In general, it is worth mentioning that, this virtual receiver matrix is not limited to the proposed block diagram (detailed in Section 3.2.1), and each unit-cell can be redesigned or arranged based on the design requirements. For instance, instead of using two or four unit-cells as a virtual receiver, as demonstrated in this paper, it is also possible to redesign the unit cells to form a receiver from three or more units. If we consider that, any p unit-cells from a complete virtual receiver, in a matrix with M x N elements, the total number of possible virtual receivers (T) can be calculated readily using the following formula

$$T = \binom{N \times M}{p} = \frac{(N \times M)!}{p! \times (N \times M - p)!} \quad , p = 2, 3, 4, \ldots \tag{3.1}$$

Fig. 3.2 compares the total number of possible virtual receivers with conventional fixed receiver arrays, for a square matrix with N^2 elements. As it can be seen in this figure, by increasing the number of elements forming a virtual receiver (p), the total number of possible virtual receivers increases considerably. In the following, the theoretical modeling of unit-cell design based on multi-port interferometric technique is presented. Also, the AoA detection function is investigated using the same unit-cell design, but with different spatial combination of unit-cells.

3.2.1 Virtual Receiver: Unit-Cell Modeling

In this proposed VRM "topology", any type of receiver (from the well-known six-port to heterodyne receiver architectures) that uses the phase difference of incident waves to demodulate a QAM signal can be employed as a unit-cell of VRM. In the following, we use multi-port interferometric techniques for the purpose of VRM unit-cells realization, as a proof-of-concept.

The block diagram of Fig. 3.3 shows the interferometric design of VRM unit-cells, each containing an antenna, a low noise amplifier (LNA), a power combiner, and a power detector. In fact, these unit-cells receivers behave like well-known homodyne receivers with a single-ended diode mixer. By designing maximum isolation between the ports of power combiner, the challenge of leakage is alleviated in this type of receiver.The received RF signal after LNA can be considered as,

$$S_{RF}(t) = a_{RF}.\alpha(t)e^{j(\omega_{RF}t+\theta(t)+\theta_0)} \tag{3.2}$$

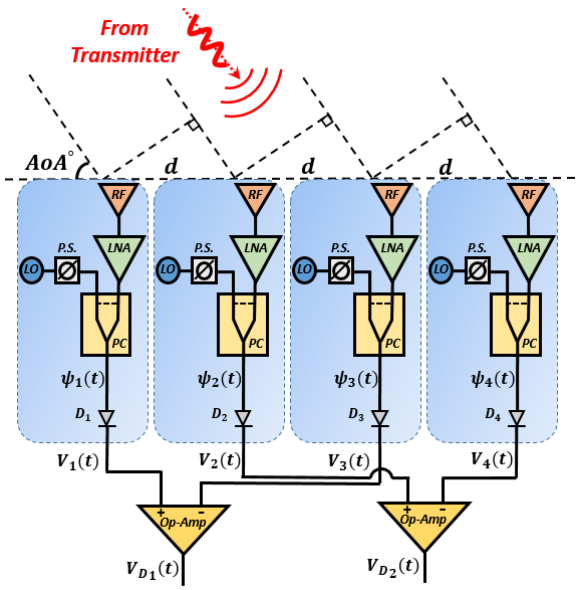

Figure 3.3 Block diagram of VRM unit-cell design, including antenna, low noise amplifier (LNA), power detectors and operational amplifiers. Four equally distanced unit-cells form a complete virtual receiver. In the case of $a_{LO} \gg a_{RF}$, only two unit-cells can form a virtual receiver (P.S. is short for phase shifter).

where, a_{RF} is the amplitude of the received signal after LNA. $\alpha(t)$ and $\theta(t)$ are the modulated amplitude and phase of transmitted baseband signal, respectively. θ_0 is the phase difference between the RF and LO signals, if considering the injected LO signal as the following expression

$$S_{LO}(t) = a_{LO}.e^{j\omega_{LO}t} \tag{3.3}$$

where a_{LO} is the amplitude of the LO signal. For a coherent receiver design of VRM, frequencies of RF and LO should be considered the same $\omega_{LO} = \omega_{RF} = \omega$. Also, if we consider $\Delta\theta(t) = \theta(t) + \theta_0$, then the signal after the power combiner for the first unit-cell can be written as

$$\psi_1(t) = a_{LO}.e^{j\omega t}[1 + \frac{a_{RF}}{a_{LO}}.\alpha(t)e^{j\Delta\theta(t)}] \tag{3.4}$$

In a receiver matrix where its unit-cells are equally distributed, the phase difference of an incoming signal between each two unit-cells with an incident angle of AoA and an inter-element distance of d can be expressed as

$$\Delta\phi = \frac{2\pi d}{\lambda}\cos(AoA) \tag{3.5}$$

where λ is the operational wavelength of the incoming signal. It is also worth mentioning that, the VRM is considered in the far-field zone of transmitters, where the incident waves are considered as plane waves. If we consider the phase reference at the first unit-cell, then signals of other three adjacent unit-cells with equal inter-element distances can be described as

$$\psi_2(t) = a_{LO}e^{j\omega t}[1 + \frac{a_{RF}}{a_{LO}}.\alpha(t)e^{j(\Delta\theta(t)+\Delta\phi)}] \tag{3.6}$$

$$\psi_3(t) = a_{LO}e^{j\omega t}[1 + \frac{a_{RF}}{a_{LO}}.\alpha(t)e^{j(\Delta\theta(t)+2\Delta\phi)}] \tag{3.7}$$

$$\psi_4(t) = a_{LO}e^{j\omega t}[1 + \frac{a_{RF}}{a_{LO}}.\alpha(t)e^{j(\Delta\theta(t)+3\Delta\phi)}] \tag{3.8}$$

The output of each power combiner in the block diagram of Fig. 3.3 is connected to a power detector. The output voltages of power detectors are proportional to the square magnitude of their input signals.

$$V(t) = K\,|\psi_i(t)|^2, \quad i = 1, 2, 3, 4. \tag{3.9}$$

where K is a constant related to the characteristics of power detectors. Accordingly, the output voltages of each unit-cell can be obtained as follows

$$V_1(t) = K{a_{LO}}^2[1 + 2\frac{a_{RF}}{a_{LO}}\alpha(t)\cos(\Delta\theta(t)) + (\frac{a_{RF}}{a_{LO}})^2\alpha(t)^2] \tag{3.10}$$

$$V_2(t) = K{a_{LO}}^2[1 + 2\frac{a_{RF}}{a_{LO}}\alpha(t)\cos(\Delta\theta(t) + \Delta\phi) + (\frac{a_{RF}}{a_{LO}})^2\alpha(t)^2] \tag{3.11}$$

$$V_3(t) = K{a_{LO}}^2[1 + 2\frac{a_{RF}}{a_{LO}}\alpha(t)\cos(\Delta\theta(t) + 2\Delta\phi) + (\frac{a_{RF}}{a_{LO}})^2\alpha(t)^2] \tag{3.12}$$

$$V_4(t) = K{a_{LO}}^2[1 + 2\frac{a_{RF}}{a_{LO}}\alpha(t)\cos(\Delta\theta(t) + 3\Delta\phi) + (\frac{a_{RF}}{a_{LO}})^2\alpha(t)^2] \tag{3.13}$$

Now, if we set the variables of inter-element distance, operational wavelength, and incident angle of the incoming signal (AoA) to make (3.5) equal to $2n\pi + \frac{\pi}{2}$, where n is an integer number ($n = 0, 1, 2, \cdots$), the output voltages of power detectors in (3.11) to (3.13) can be simplified to the following expressions.

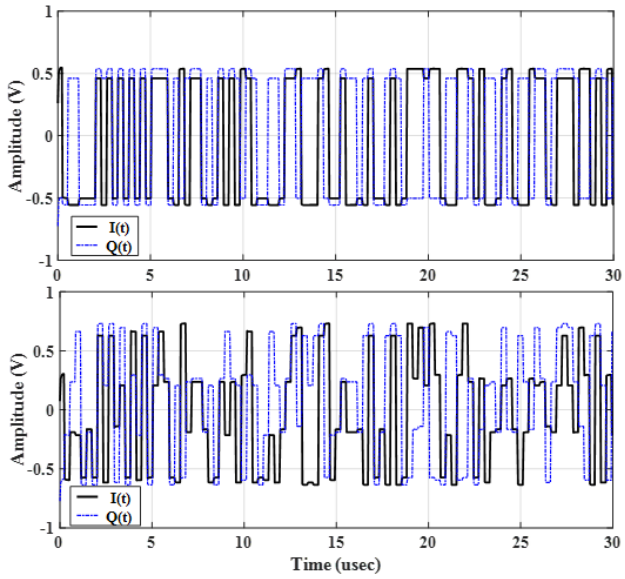

Figure 3.4 Simulation results for recovered in-phase and quadrature components of (a) QPSK (b) 16-QAM signals at data rate of 2 MSps.

$$V_2(t) = K{a_{LO}}^2[1 - 2\frac{a_{RF}}{a_{LO}}\alpha(t)\sin(\Delta\theta(t)) + (\frac{a_{RF}}{a_{LO}})^2\alpha(t)^2] \tag{3.14}$$

$$V_3(t) = K{a_{LO}}^2[1 - 2\frac{a_{RF}}{a_{LO}}\alpha(t)\cos(\Delta\theta(t)) + (\frac{a_{RF}}{a_{LO}})^2\alpha(t)^2] \tag{3.15}$$

$$V_4(t) = K{a_{LO}}^2[1 + 2\frac{a_{RF}}{a_{LO}}\alpha(t)\sin(\Delta\theta(t)) + (\frac{a_{RF}}{a_{LO}})^2\alpha(t)^2] \tag{3.16}$$

Then, the in-phase and quadrature components of a received QAM signal can be obtained using the two operational amplifiers (Op-Amps) shown in Fig. 3.3.

$$I(t) = V_{D_1}(t) = V_1(t) - V_3(t) = K^{'}\alpha(t)\cos\theta(t) \tag{3.17}$$

$$Q(t) = V_{D_2}(t) = V_4(t) - V_2(t) = K^{'}\alpha(t)\sin\theta(t) \tag{3.18}$$

where $K^{'} = 4Ka_{LO}a_{RF}$. If we define a complex vector of $S(t) = I(t) + jQ(t)$, the magnitude of this expression would be proportional to the amplitude of transmitted baseband signal. Finally, using a phase shifter before LO, we can set θ_0 equal to zero to remove the mismatch between the phases of RF and LO signals. Fig. 3.4(a) and (b) show the simulation results of demodulated in-phase and quadrature components of QPSK and 16-QAM signals with a data rate of 2 MSps, respectively.

In the VRM, by knowing the amplitude of received signals compared to the injected LO

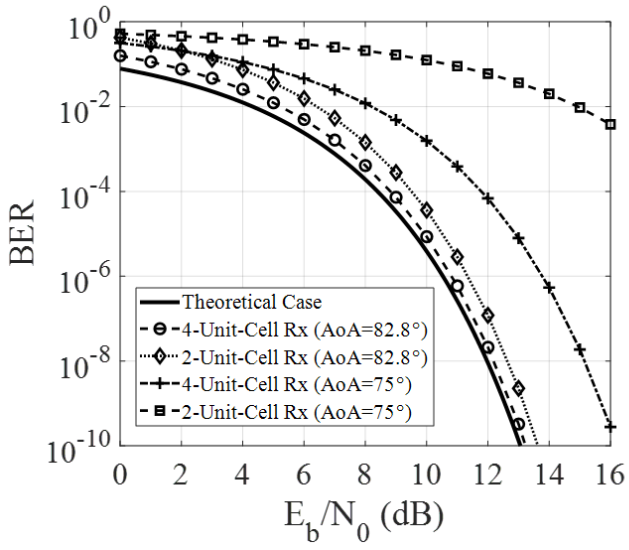

Figure 3.5 BER of virtual receivers for two AoAs of 82.8° and 75°, in two cases of 4-unit-cell receiver and 2-unit-cell receiver. QPSK modulation with data rate of 2MSps is chosen for simulation.The two scenarios of 2- and 4- unit-cell receivers are simulated individually.

power, we can neglect the term of $(a_{RF}/a_{LO})^2$in (3.10) and (3.14), provided that a_{LO} is much larger than a_{RF}. Then, the simplified version can be written as,

$$V_1(t) \cong K{a_{LO}}^2[1 + 2\frac{a_{RF}}{a_{LO}}\alpha(t)\cos(\Delta\theta(t))] \tag{3.19}$$

$$V_2(t) \cong K{a_{LO}}^2[1 - 2\frac{a_{RF}}{a_{LO}}\alpha(t)\sin(\Delta\theta(t))] \tag{3.20}$$

By using a filter, we can remove the DC parts of (3.19) and (3.20), and as a result, the in-phase and quadrature components can be obtained using only two unit-cells.

The bit error rate (BER) for a QPSK modulation with an input white Gaussian noise is defined as

$$P_b = \frac{1}{2}erfc\left(\sqrt{\frac{E_b}{N_0}}\right) \tag{3.21}$$

where E_b is the bit energy, N_0 / 2 is the variance of the additive white Gaussian noise, and the $erfc$ is the complementary error function. A white Gaussian noise source is added to the ADS simulations to compare the BER of virtual receivers with the ideal case of 3.21. Fig. 3.5 shows the BER for two different scenarios of the virtual receivers formed by four and two unit-cells for two different incident angles of 82.8 and 75 degrees, respectively (for a VRM with d / $\lambda = 2$). Since, the inter-element distances between the unit-cells are chosen to be

two wavelengths, the AoA for satisfying the 90-degree phase shift is 82.8 degrees. As it can be seen, when the AoA is deviated by 7.8 degrees from the desired one, the BER is distorted, since the phase difference between cells ($\Delta\phi$) is no longer equal to 90 degrees.

3.2.2 Angle-of-Arrival (AoA) Detection System

In the previous subsection, the unit-cell design procedure of the VRM concept is investigated, and in the following, one application of such 2D distributed configuration of virtual receivers is presented. One important function that determines the stability and robustness of a point-to-point wireless communication link is the AoA detection that can be used to compensate for the probable deviations and distortions. In the proposed VRM, using exactly the same unit-cells design, the AoA can be detected using only four unit-cells in a line arrangement, as shown in Fig. 3.6. In this figure, the inter-element distances between the unit-cells are the same, as in the data reception function, with this difference that the zero reference for phase is the central unit-cell (ψ_{mn}). For any unknown incident wave with arbitrary AoA, two sets of perpendicular activated AoA detector units can determine the 2D AoA. In Fig. 3.6, the signals after power combiners in activated AoA detectors in the x-direction can be described as

$$\psi_{m-2k,n}(t) = a_{LO}.e^{j\omega t}[1 + \frac{a_{RF}}{a_{LO}}.\alpha(t)e^{j(\Delta\theta(t)-2\Delta\phi)}] \tag{3.22}$$

$$\psi_{m-k,n}(t) = a_{LO}.e^{j\omega t}[1 + \frac{a_{RF}}{a_{LO}}.\alpha(t)e^{j(\Delta\theta(t)-\Delta\phi)}] \tag{3.23}$$

$$\psi_{m+k,n}(t) = a_{LO}.e^{j\omega t}[1 + \frac{a_{RF}}{a_{LO}}.\alpha(t)e^{j(\Delta\theta(t)+\Delta\phi)}] \tag{3.24}$$

$$\psi_{m+2k,n}(t) = a_{LO}.e^{j\omega t}[1 + \frac{a_{RF}}{a_{LO}}.\alpha(t)e^{j(\Delta\theta(t)+2\Delta\phi)}] \tag{3.25}$$

As a result, the output voltages of power detectors related to each unit-cell can be calculated as

$$V_{m-2k,n}(t) = K{a_{LO}}^2[1 + 2\frac{a_{RF}}{a_{LO}}\alpha(t)\cos(\Delta\theta(t) - 2\Delta\phi) + (\frac{a_{RF}}{a_{LO}})^2\alpha(t)^2] \tag{3.26}$$

$$V_{m-k,n}(t) = K{a_{LO}}^2[1 + 2\frac{a_{RF}}{a_{LO}}\alpha(t)\cos(\Delta\theta(t) - \Delta\phi) + (\frac{a_{RF}}{a_{LO}})^2\alpha(t)^2] \tag{3.27}$$

$$V_{m+k,n}(t) = K{a_{LO}}^2[1 + 2\frac{a_{RF}}{a_{LO}}\alpha(t)\cos(\Delta\theta(t) + \Delta\phi) + (\frac{a_{RF}}{a_{LO}})^2\alpha(t)^2] \tag{3.28}$$

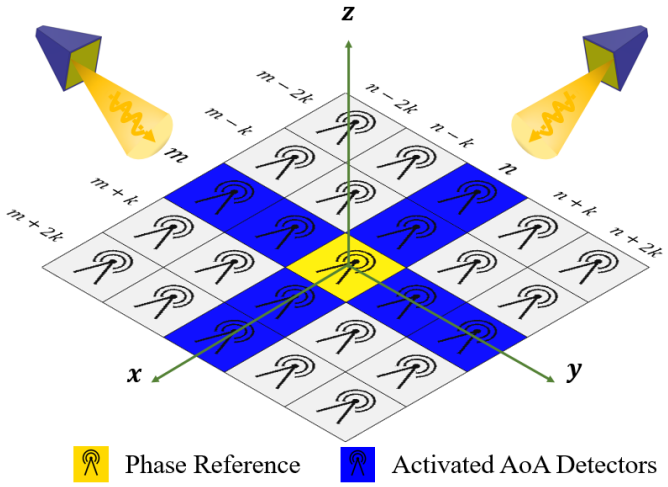

Figure 3.6 Two-dimensional Angle-of-Arrival (AoA) detection using four unit-cells in a line arrangement for both x and y directions.

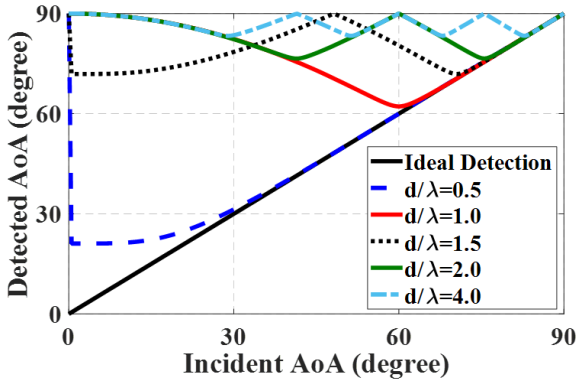

Figure 3.7 Simulation results of AoA for an incident beam using the AoA detector system for different ratios of inter-element distances over wavelength.

$$V_{m+2k,n}(t) = K{a_{LO}}^2[1 + 2\frac{a_{RF}}{a_{LO}}\alpha(t)\cos(\Delta\theta(t) + 2\Delta\phi) + (\frac{a_{RF}}{a_{LO}})^2\alpha(t)^2] \tag{3.29}$$

By subtracting the output voltages of the activated AoA detectors, the following formulas are obtained.

$$V_{m-2k,n}(t) - V_{m+2k,n}(t) = 8Ka_{LO}a_{RF}\alpha(t)\sin\theta(t)\sin 2\Delta\phi \tag{3.30}$$

$$V_{m-k,n}(t) - V_{m+k,n}(t) = 8Ka_{LO}a_{RF}\alpha(t)\sin\theta(t)\sin\Delta\phi \tag{3.31}$$

After some trigonometric simplifications, we can generate the following formula for obtaining the $\Delta\phi$.

$$\Delta\phi = \cos^{-1}\left(\frac{V_{m-2k,n} - V_{m+2k,n}}{2(V_{m-k,n} - V_{m+k,n})}\right) \tag{3.32}$$

In order to find the AoA we can use 3.5, and use another inverse cosine function on (3.32) as below

$$AoA = \cos^{-1}\left(\frac{\lambda}{2\pi d}\cos^{-1}\left(\frac{V_{m-2k,n} - V_{m+2k,n}}{2(V_{m-k,n} - V_{m+k,n})}\right)\right) \tag{3.33}$$

Fig. 3.7 shows the simulated and detected AoA compared to the ideal case for different ratios of wavelength over inter-element distances. As illustrated in this figure, by increasing the ratio of inter-element distance over wavelength, the unambiguous range of AoA detectors are become narrower, which is rooted in the nature of inverse cosine function.

3.2.3 Ambiguity Analysis of Virtual Receiver

As mentioned in the modeling of virtual receivers, the AoA is the key factor in the data receiving operation, which determines the required phase difference between cells. Therefore, it is important to analyze and investigate the operational unambiguous range of virtual receivers. If we extract the output voltages of VRM unit-cells in a matrix form, the following equation would be obtained after some trigonometric calculations.

$$\begin{bmatrix} I(t) \\ Q(t) \end{bmatrix} = 4Ka_{LO}a_{RF}\bar{\bar{M}}\begin{bmatrix} \alpha(t)\cos(\Delta\theta(t)) \\ \alpha(t)\sin(\Delta\theta(t)) \end{bmatrix} \tag{3.34}$$

where$\bar{\bar{M}}$ is the transformation matrix relating to the received and transmitted signals.

$$\bar{\bar{M}} = \begin{bmatrix} \sin^2\Delta\phi & -\sin\Delta\phi\cos\Delta\phi \\ 2\cos\Delta\phi - 2\cos^3\Delta\phi & -\sin\Delta\phi + 2\sin^3\Delta\phi \end{bmatrix} \tag{3.35}$$

If we calculate the determinant of (36), it would be simplified to the following equation.

$$det(\bar{\bar{M}}) = \sin^3\Delta\phi \tag{3.36}$$

If $\bar{\bar{M}}$ is an invertible matrix,$(det(\bar{\bar{M}}) \neq 0)$, the receiver can still demodulate the received signals. The determinant of $\bar{\bar{M}}$ is a periodic function and it is depicted in Fig. 3.8 for different ratios of inter-element distances to operational wavelength. As it can be seen, by increasing this ratio, the ambiguous points in which their determinant is equal to zero is increased and consequently the number of AoAs that cannot be used for data reception is increased.

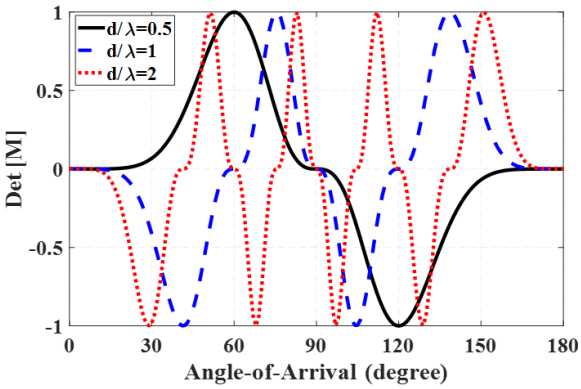

Figure 3.8 Determinant of transformation matrix (M) with respect to Angle-of-Arrival for different ratios of inter-element distances over operational wavelength.

Therefore, at a constant operational frequency, the least value for inter-element distances of unit-cell in VRM results in a wider unambiguity range for data reception. However, extremely small inter-element distances would increase the mutual couplings between the antennas of each unit-cell, and a compromise between the unambiguity range and destructive effects of mutual coupling should be considered.

3.2.4 Polarization Detection Analysis

In this final sub-section, using exactly the same unit-cell design for both data reception and AoA detection, the analysis of detecting the polarization rotation angle of any unknown linearly polarized signal is also investigated. As shown in Fig. 3.9, the first and third antennas of VRM unit-cells have perpendicular polarized radiations with respect to the second and fourth ones. Here we assume horizontal and vertical polarized antennas with acceptable co-to-cross level ratios. For the linearly polarized radiation with a rotation angle of γ, shown in Fig. 3.9, the unit-cells with horizontal and vertical radiations receive signals proportional to $\cos(\gamma)$ and $\sin(\gamma)$, respectively. Also, considering the phase difference of incident signal, the following expressions can be written as the output voltages in Fig. 3.9.

$$V_1(t) = K{a_{LO}}^2[1 + 2\frac{a_{RF}}{a_{LO}}\cos(\gamma)\alpha(t)\cos(\Delta\theta(t)) + (\frac{a_{RF}}{a_{LO}})^2\alpha(t)^2] \tag{3.37}$$

$$V_1(t) = K{a_{LO}}^2[1 + 2\frac{a_{RF}}{a_{LO}}\sin(\gamma)\alpha(t)\cos(\Delta\theta(t) + \Delta\phi) + (\frac{a_{RF}}{a_{LO}})^2\alpha(t)^2] \tag{3.38}$$

$$V_1(t) = K{a_{LO}}^2[1 + 2\frac{a_{RF}}{a_{LO}}\cos(\gamma)\alpha(t)\cos(\Delta\theta(t) + 2\Delta\phi) + (\frac{a_{RF}}{a_{LO}})^2\alpha(t)^2] \tag{3.39}$$

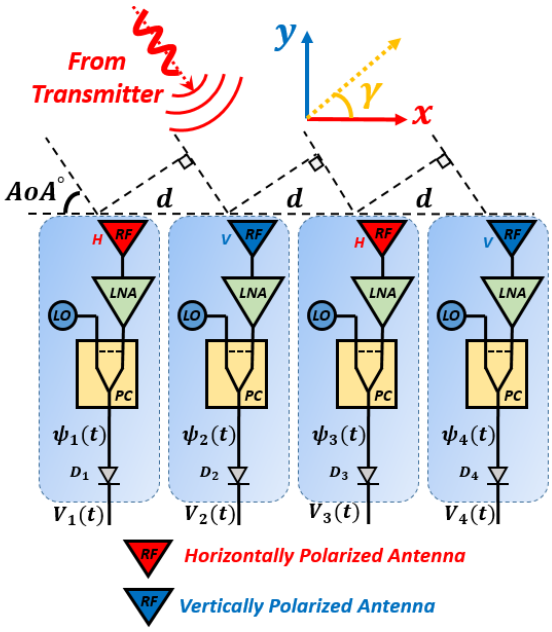

Figure 3.9 Polarization detection system with horizontally and vertically polarized radiations using four adjacent unit-cells.

$$V_1(t) = K{a_{LO}}^2[1 + 2\frac{a_{RF}}{a_{LO}}\sin(\gamma)\alpha(t)\cos(\Delta\theta(t) + 3\Delta\phi) + (\frac{a_{RF}}{a_{LO}})^2\alpha(t)^2] \tag{3.40}$$

Again, considering $\Delta\phi$ equal to 90 degrees, we can have

$$V_1(t) + V_3(t) = 2Ka_{LO}^2[1 + \cos^2(\gamma)(\frac{a_{RF}}{a_{LO}})^2\alpha^2(t)] \tag{3.41}$$

$$V_2(t) + V_4(t) = 2Ka_{LO}^2[1 + \sin^2(\gamma)(\frac{a_{RF}}{a_{LO}})^2\alpha^2(t)] \tag{3.42}$$

Now, after removing the DC parts in (3.41) and (3.42), we have

$$V_1^{'}(t) = 2K\cos^2(\gamma)a_{RF}^2\alpha^2(t) \tag{3.43}$$

$$V_2^{'}(t) = 2K\sin^2(\gamma)a_{RF}^2\alpha^2(t) \tag{3.44}$$

Therefore, by dividing 3.43 over 3.44, we can obtain the rotation angle of any linearly polarized radiation

$$\frac{V_1^{'}(t)}{V_2^{'}(t)} = \tan^2(\gamma) \quad \rightarrow \quad \gamma = \tan^{-1}\left(\sqrt{\frac{V_1^{'}(t)}{V_2^{'}(t)}}\right) \tag{3.45}$$

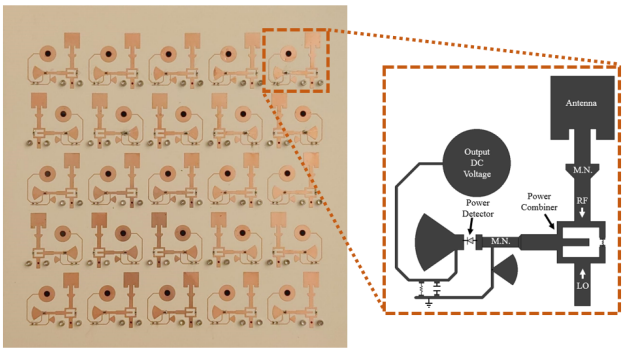

(a)

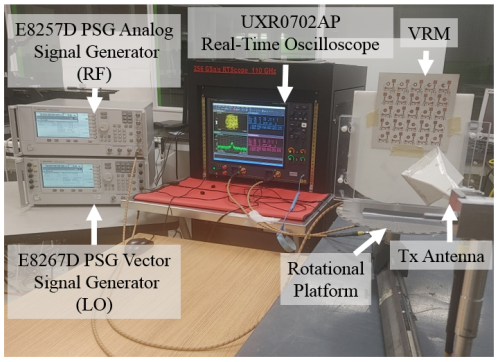

(b)

Figure 3.10 (a) Multifunction Virtual Receiver Matrix (VRM) prototype demonstration. M.N. is short for matching network. (b) Photograph of the measurement setup test bench for the fabricated VRM prototype. The measurement equipment is synchronized with 10 MHz reference signal.

3.3 Demonstration And Experimental Results

To validate and evaluate the performance of the proposed VRM and theoretical foundation, a proof-of-concept prototype is fabricated with an inter-element distance of two wavelengths on Rogers RO3003 substrate with $\epsilon_r = 3$ and thickness of 20 mils to operate at 28 GHz for 5G mmW systems, as shown in Fig. 3.10(a). This prototype is designed, simulated, and optimized in both full-wave simulators of CST Studio and Keysight Advanced Design System (ADS) software. A fed-through microstrip antenna is used to receive the RF modulated signal from the transmitter. Then, the RF signal is connected to the power combiner using a matching network, while the LO signal is injected through the other port of power combiner. Both RF and LO signals are combined and applied to a Schottky diode power detector, SMS 7621-040LF. A matching network ensures detectable output voltage levels. By the way, the principle of the proposed VRM technique is not limited to the printed circuit board (PCB)

and can be extended for an integrated circuit (IC) implementation for large-scale THz receiver arrays.

The distribution of LO signal to each unit-cell of VRM, however, poses challenges from equal distribution to in-phase excitation. In this connection, self-oscillating mixers would be a good candidate for LO signal generation [163]. For the purpose of our proof-of-concept prototype, in the experimental setup, only the selected unit-cells in Table. 3.1 are excited with the LO signal to work as an activated receiver. Since each unit-cell of the proposed VRM is similar, the injected LO power is connected to the receiving units using external power dividers and a phase shifter to ensure the in-phase excitation of each unit-cell. In Table. 3.1 two cases of four-unit-cell ($M_{11}, M_{12}, M_{13}, M_{14}$) and two-unit-cell receivers (M_{32}, M_{35}) are selected to demodulate a QAM signal for specific AoAs, at a data rate of 1 MSps. The second is using only two unit-cells but with different input RF power and incident angle. As can be seen in 3.1, the extracted EVM from the oscilloscope is increased when only using two unit-cells, but still below 9%.

The measurements of the receiver are conducted with Keysight UXR0702AP Real-Time Oscilloscope, an Agilent E8257D PSG Analog Signal Generator, an Agilent E8267D Vector Signal Generator, and an Agilent N1914A power meter. In order to synchronize the RF and LO signals, a 10 MHz synchronization signal is applied to both signal generators and analyzers. The fabricated prototype is a matrix with 5x5 elements, located on a rotational platform displaying the rotated degrees, as shown in Fig. 3.10(b). The RF transmitter is a diagonal horn antenna FR6413 from ORBIT/FR with 17 dBi gain at 28 GHz. The receiver antenna was designed in a way that receives for any incident angles similar to an omni-directional pattern with a gain of about 6.7 dBi and 7.3% of bandwidth. The fabricated prototype is a matrix with 5x5 elements. As stated in Section 3.1, numerous combinations of unit-cells can form a virtual receiver. Fig. 3.11 shows the output EVM for AoA deviations for the first case of Table. 3.1 for 32-QAM signal with a data rate of 1 MSps. As can be seen in this figure, by changing about ± 5 degrees around the exact AoA, the EVM of the demodulated signal is still below 10%, which is acceptable.

3.4 Conclusion

In this work, the concept of VRM architecture suitable for future multifunction wireless systems is proposed, presented, and demonstrated for the first time. The most significant advantage of VRM topology compared to the conventional “fixed” receiver arrays is the number of possible virtual receivers. The incoming signal properties in the 2D distributed units of VRM, determines the dynamic allocations of activated receiving units to demodulate

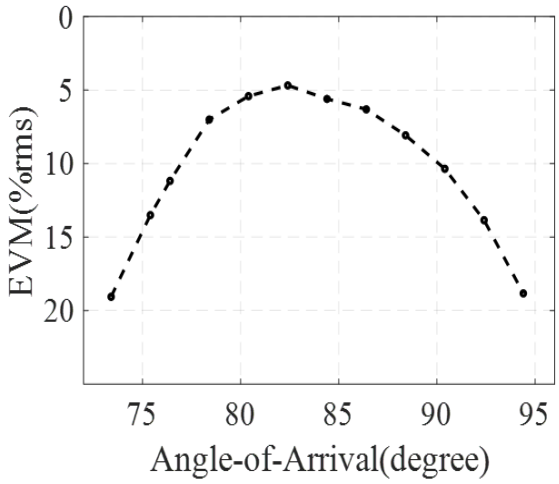

Figure 3.11 Measured EVM for different AoAs of 4-unit-cell Rx in Table 3.1.

a QAM signal. This floating and dynamic feature of virtual receivers enables the seamless integration of multifunctionalities while significantly enhancing the capacity and agility of receiver topology compared to prior-art architectures. The implemented unit-cell in this paper is not limited to interferometric receiver architectures as demonstrated in this work and in fact any other receiver type that uses the phase difference of incoming signals can be used. The mathematical formulations and the proof-of-concept prototype measurements confirm the validity of VRM operations. The proposed VRM solution is believed to be a paradigm shift in the design and development of 5G, 6G, and future multifunction wireless techniques and systems.

Table 3.1 Measured Normalized Constellation Diagrams With Different Orders of Modulation (M-QAM) And For Different Analog Combinations of Virtual Receivers.

Modulation Order (M-QAM)	Four-Unit-Cell Rx ($M_{11}, M_{12}, M_{13}, M_{14}$) (Data Rate= 1MSps & AoA = 82.8°)	Two-Unit-Cell Rx (M_{32}, M_{35}) (Data Rate= 1MSps & AoA = 86.4°)
4-QAM	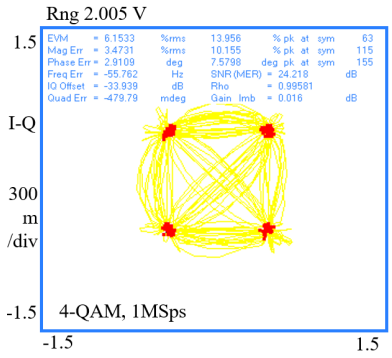	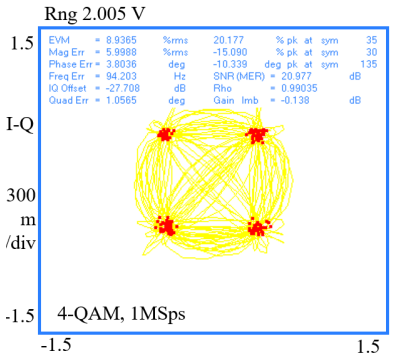
16-QAM	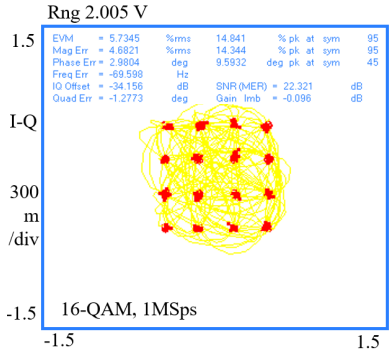	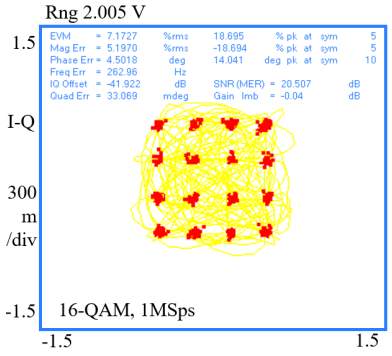
32-QAM	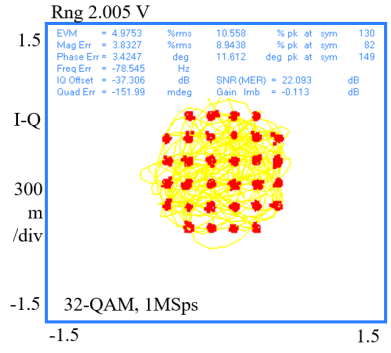	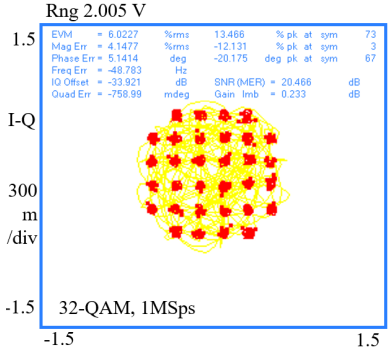

CHAPTER 4 ARTICLE 3: CONCURRENT DETECTION OF 2-D ANGLE-OF-ARRIVAL AND POLARIZATION ENABLED BY VIRTUAL TRANSCEIVER MATRIX ARCHITECTURE

Seyed Ali Keivaan, Pascal Burasa, Jie Deng and Ke Wu
Published in: *IEEE Transactions on Microwave Theory and Techniques*
Publication Date: March 21, 2025

This paper introduces and demonstrates an integrated concurrent sensing and communication system characterized by multifunctionality and reconfigurability, underpinned by dynamic cell allocation within a topologically distributed matrix. Unlike traditional Angle-of-Arrival (AoA) or polarization detection systems, this approach offers a vastly expanded range of matrix cell combinations, facilitating the integration of diverse and simultaneous operations in a single transceiver architecture. Our proposed programmable front-end is set to synthesize transmitter (Tx) / receiver (Rx) channels by adapting to the instantaneous characteristics of incoming signals from various sources. We establish and explore a mathematical model of unit cells and conduct modulation tests utilizing 64-/128- Quadrature Amplitude Modulation (QAM), achieving data rates of up to 250 Msps, with a maximum error vector magnitude (EVM) of 4.56%. The AoA measurements demonstrate an error of approximately 0.9° in a range of -12° to 12°. Also, the polarization rotation measurements show an error of maximum 2.8° for an entire spanning range of zero to 90 degrees. The results underscore the efficacy of proposed VTM for its possible deployment across a spectrum of applications including base stations and user terminals for next generation 5G/6G communications, sensing systems, and beyond.

4.1 Introduction

In the realm of wireless communications and sensing systems, precision detection of signal parameters such as Angle of Arrival (AoA) and polarization is crucial for enhancing system application, performance, and reliability [145]. These parameters provide essential information for real-world applications ranging from radar-based target tracking to spatial multiplexing in emerging and future multiple-input multiple-output (MIMO) communication and sensing systems. Leveraging polarization diversity can mitigate signal fading and polarization mismatch losses as well as improve signal discrimination in a crowded and interference-prone environment. Additionally, polarization-aware systems would bolster channel estimation,

spatial multiplexing gain, and enhanced link reliability. Consequently, different techniques for AoA and polarization detection have garnered significant attention through recent research and development efforts [61, 102, 104, 113, 164]. Indeed, future-generation wireless communication systems demand integration and synergy of multifunctionalities within an integrated front-end architecture [141].

Early and current generations have relied on Distributed Antenna Systems (DAS) [165], but challenges are persisting on how to effectively distribute received signals. Large-scale phased array transceivers have emerged as promising components in 5G/6G systems due to their high-speed data rate, precise location capabilities, and rapid scanning identification [147,148]. However, implementing low-loss broadband phase shifters becomes increasingly complex as system scale expands, thus limiting system performance and application range [149]. Another approach involves ultra-dense networks with multiple base stations and access points based on MIMO, offering high link-level gains and mitigating path-related losses [155–157]. However, analog/RF front-end interference remains a concern in MIMO systems [158]. In this context, prevailing millimeter-wave (mmW) and/or terahertz (THz) transceiver architectures may prove inadequate to support the anticipated mega-connections in future wireless systems.

Emerging techniques have been studied for AoA and polarization detection, which include metasurface structures [166] and multi-port devices. For instance, a compact broadband six-port junction was proposed for AoA detection [61], yet it primarily operates in one dimension due to its limited input channels. Efforts to extend detection coverage into two and three dimensions include integrating down-converted mixers [167] and measuring time differences of arrival [168], though these approaches may not be cost-effective or scalable. Recent advancements underscore unconventional systematic schemes like expanding six-port junctions to eight-port or sixteen-port interferometers for improved 2-D AoA estimation [102, 113], yet scalability and integration with other functionalities like polarization detection remain challenging. Therefore, future solutions must enable efficient multifunctionalities based on smart, dense, AoA-agile, and polarization-agile transceivers, thus maximizing capacity and speed [20].

This work derives and explores the concept of multifunction Virtual Transceiver Matrix (VTM) to meet the demand for next-generation wireless communication and sensing systems. The proposed VTM topology offers unprecedented flexibility in implementing concurrent functionalities and operations within a unified front-end wireless system. This transceiver architecture enables dynamic allocation of unit-cells to synthesize channels in support of transmission, reception, and sensing functions, as illustrated in Fig. 4.1. Baseband-recovered data from each unit-cell can be repurposed for various functionalities and data processing,

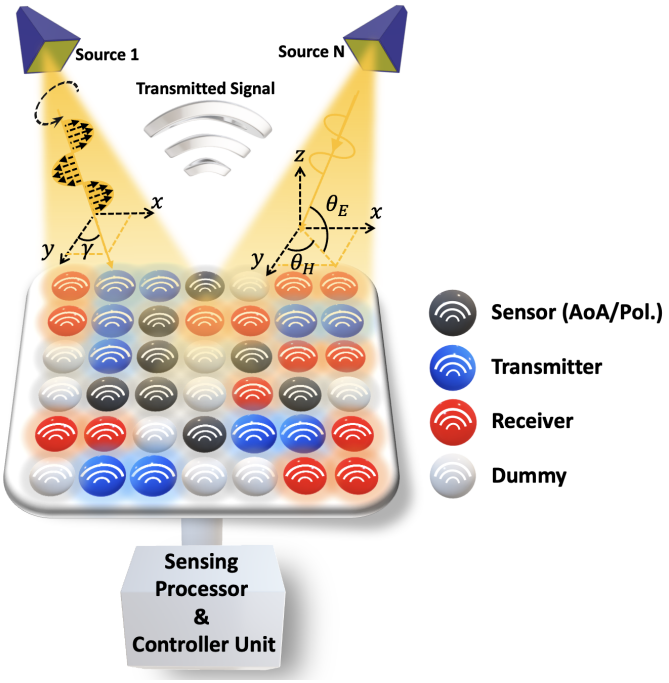

Figure 4.1 Conceptual diagram illustrating the proposed sensing and communication VTM front-end. This multifunctional system is designed to detect the Angle of Arrival (AoA) and polarization of arbitrary incident QAM signals, alongside facilitating both receiving (Rx) and transmitting (Tx) functions. A key feature is the multi-layer LO feed network within the VTM, ensuring equal amplitude of LO signals with adjustable phases, tailored to accommodate both Rx and Tx operations. Additionally, a controller unit is used to govern the dynamic operation of individual cells, allowing for an efficient power management through the activation or deactivation (dummy) of selected units.

thereby enhancing capacity, sensing, and power/data management efficiency. Unlike traditional systems that are set to prioritize either AoA or polarization detection, the VTM facilitates a multifunctional wireless communication and sensing system capable of performing these operations simultaneously, while maintaining high data rate communication with robust performance. The multi-port interferometer, recognized as an effective low-power solution for single down conversion to baseband or IF [6,8,10,16,19,43,87,91,96,115,118,120,161,169–171], is considered in this work to demonstrate our proof-of-concept.

The remainder of this paper is organized as follows: Section II discusses the theoretical modeling of a multi-layer Local Oscillator (LO) feed network and VTM unit-cells, highlighting their applications in transceiver functionality, AoA detection, and polarization analysis. It presents simulation and measurement results for aforementioned applications. Section III introduces the measurement setup for an experimental prototype tailored for 5G multifunc-

tional applications, providing validation through comprehensive simulation and measurement results.

4.2 VTM Theoretical Modeling and Implementation

This section introduces a theoretical framework for modeling the proposed transceiver unit-cells, depicted in Fig. 4.1, encompassing functions such as AoA and polarization detection. While traditional sensing systems prioritize either AoA or polarization detection, this work, as mentioned earlier, proposes a multifunctional wireless communication and sensing system capable of simultaneously performing all these operations. The flowchart in Fig. 4.2 summarizes the necessary steps for the operations of VTM. According to this flowchart, the 2D AoA detectors and polarization detectors are initially activated to track the characteristics of incoming sources in a hypothetical scenario illustrated in Fig. 4.1. Subsequently, this data is transferred to a processor to decide the activation of specific receiving cells for demodulating QAM signals corresponding to the identified AoA and polarization. Meanwhile, other cells may serve for transmitting QAM signals. The activation of transmitter cells depends on achieving the necessary signal gain, while the number of receiver cells is determined by a desired SNR. Generally, a higher count of activated transceiver cells results in improved SNR (for Rx) or directivity of radiated patterns (for Tx). If sensors do not detect any incident signal, the VTM cells will be deactivated (dummy) to reduce the power consumption.

Before exploring the mathematical modeling of VTM cells, it is necessary to conduct a comparative analysis between VTM, phased array, and MIMO systems in terms of Bit Error Rate (BER) and SNR. If we consider, for simplicity, a Single-input-single-output (SISO) channel as an example with a binary phase shift keying (BPSK) modulation source signal, we have $x[n] = hs[n] + r[n]$, where h is the fading channel, $s[n] \in \{+1, -1\}$ is the transmitted symbols, and $r[n] \sim CN(0, \sigma^2)$ is the Additive White Gaussian Noise (AWGN) ($\sigma^2$is variance). In the VTM scheme, since a Rx channel is formed by the combination of at least two cells in a floating manner, we can model the channel as depicted in Fig. 4.3(a) for the combination of N two-cell receivers. If the channels h_i are faded independently, the probability that the VTM channel is in a deep fade will be approximately described by:

$$\begin{aligned} P_r(C(M^2,2)(|h_1|^2 SNR < 1)\&\ldots\&C(M^2,2)(|h_N|^2 SNR < 1)) &= (P_r((|h|^2 SNR < 1)))^N \\ &\approx 1/(C(M^2,2).SNR^N) \end{aligned} \tag{4.1}$$

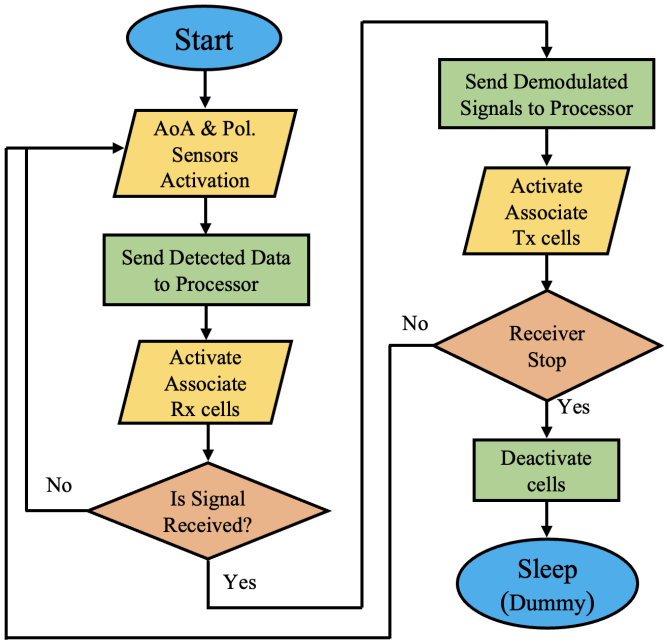

Figure 4.2 Flowchart illustrating the proposed sensing and communication VTM, initiating with AoA and polarization detection of arbitrary incident signals. Subsequently, specific cells are activated for Tx and Rx functions, contingent upon Signal-to-Noise Ratio (SNR) and gain criteria.

where $C(M^2, 2)$ represents the combination formula, which calculates the number of possible pairwise combinations within a square matrix containing $M \times M$ elements. It is mathematically defined as $M^2!/(2! \times (M^2 - 2)!)$. The channel estimation process for a MIMO system is detailed in [151]. In this context, for VTM since each channel is formed by at least two cells, the probability of each fading channel from a Tx is scaled by a factor of $C(M^2, 2)$. Fig. 4.3(b) shows the BER calculations for different scenarios of phased array, MIMO and VTM architectures for one and two transmitters. The VTM has a better performance when compared to the SISO and 2Tx1Rx systems requiring a lower SNR for a determined BER. This is rooted in the combination behavior of channels that becomes apparent in the denominator of Eq.1. $C(M^2, 2)$. It is worthwhile to mention that in the VTM, based on the design of unit-cells, instead of two cells to form a Rx channel, three, four or even a higher number of elements can get involved in the Rx operation, thus leading to even more possible combinations and better SNR. Next, we will discuss about the proposed LO feed network and its implementation in the VTM.

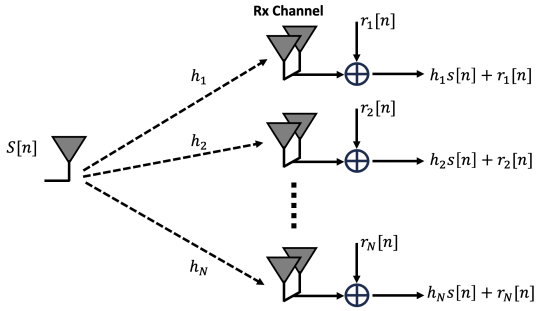

(a)

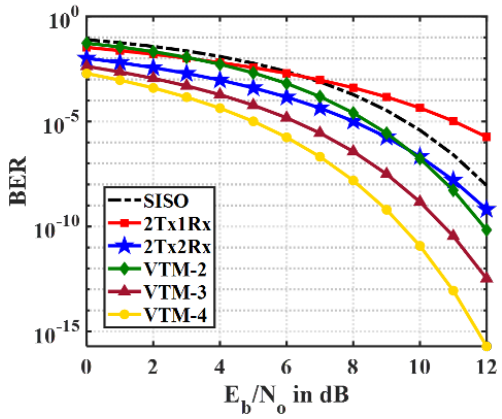

(b)

Figure 4.3 (a) Channel model implemented in the proposed multifunction sensing and communication VTM front-end. (b) Comparative analysis showcasing BER across SISO, phased array, MIMO, and VTM technologies in cases of one and two transmitters. (VTM with two-, three-, and four-cells to form a Rx channel.)

4.2.1 LO Feed Network Distribution

In the proposed TRx system, the LO signal needs to be evenly distributed across all cells within the matrix. To achieve this, we suggest making use of a LO feed network characterized by high isolation properties, facilitated by individual Field-Effect Transistor (FET) oscillators localized in each unit-cell and synchronized by a reference LO signal. Additionally, to achieve the necessary 90-degree phase shift, a hybrid coupler is incorporated into the feed network, segregating cells into two principal sections representing 0 and 90 degrees, respectively.

This segregation is essential for transmitting a QAM signal in the VTM. Specifically, two cells involved in the transmission functions are selected such that one is driven by a local oscillator (LO) at 0 degrees and the other by an LO at 90 degrees. Consequently, a QAM signal is transmitted, as detailed in the subsequent section II.B.

Fig. 4.4(a) illustrates a multi-layer LO feed network of the VTM, encompassing a matrix comprising 64 elements. Upon application of the input reference LO signal, the coupled LO signal is transmitted to the second layer housing the VTM cells and antennas (depicted in yellow color in Fig. 4.4(a)). To verify the required 90-degree phase shift of the LO signal across the VTM cells, we fabricated a prototype as depicted in Fig. 4.4(b). The FET oscillators' power source is connected to a load, rendering them unstable at 25.4 GHz. The frequency of all these FET oscillators is adapted to the reference input LO and their phase is dictated by the implemented hybrid coupler. Fig. 4.4(c) shows the simulated output voltages of the FET oscillators showing a 90-degree phase shift. The measured scattering parameters of the FET oscillators are illustrated in Fig. 4.4(d).

The individual local oscillators do not require tuning since they are all injection-locked to the reference LO, as shown in Fig. 4.4(a). The injection-locking mechanism inherently pulls the oscillator's frequency toward that of the external signal. Consequently, as long as the injection signal remains within the locking range, the oscillator stays locked, eliminating the need for tuning. In the fabricated prototype of the VTM, the injected power is exclusively for the injection locking reference signal, resulting in a relatively low requirement of around -10 dBm to drive the entire network.

To demonstrate the robustness of the proposed injection-locked oscillator, we performed an analysis of the variations in the free-running oscillation frequency. First, Fig. 4.5(a) illustrates the impact of a $\pm 5\%$ variation in the electrical length of the stub connected to the transistor source, resulting in a frequency shift of ± 400 MHz. Another critical factor investigated is temperature, particularly relevant during the transmit mode when the power amplifier (PA) is active. Simulation result in Fig. 4.5(b) shows that higher input power from the injection-locking signal effectively compensates for temperature-induced frequency variations. Additionally, we analyzed the effect of supply voltage fluctuations on the free-running frequency. A $\pm 5\%$ variation in supply voltages V_{DS} and V_{GS} caused maximum frequency shifts of ± 50 MHz and ± 12.5 MHz, respectively, both of which remain within the locking range. Measurements of the locking bandwidth were conducted for the implemented oscillator with an input power of -30 dBm, as shown in Fig. 4.5(e). The injection-locking mechanism compensates for all these frequency variations, as depicted in Fig. 4.5(f). The oscillator maintains locking for input power levels exceeding -31 dBm, and the locking bandwidth improves accordingly. It is important to note that phase noise is particularly pronounced in mixer-based architecture, unlike the multiport linear interferometric architecture used in this work.

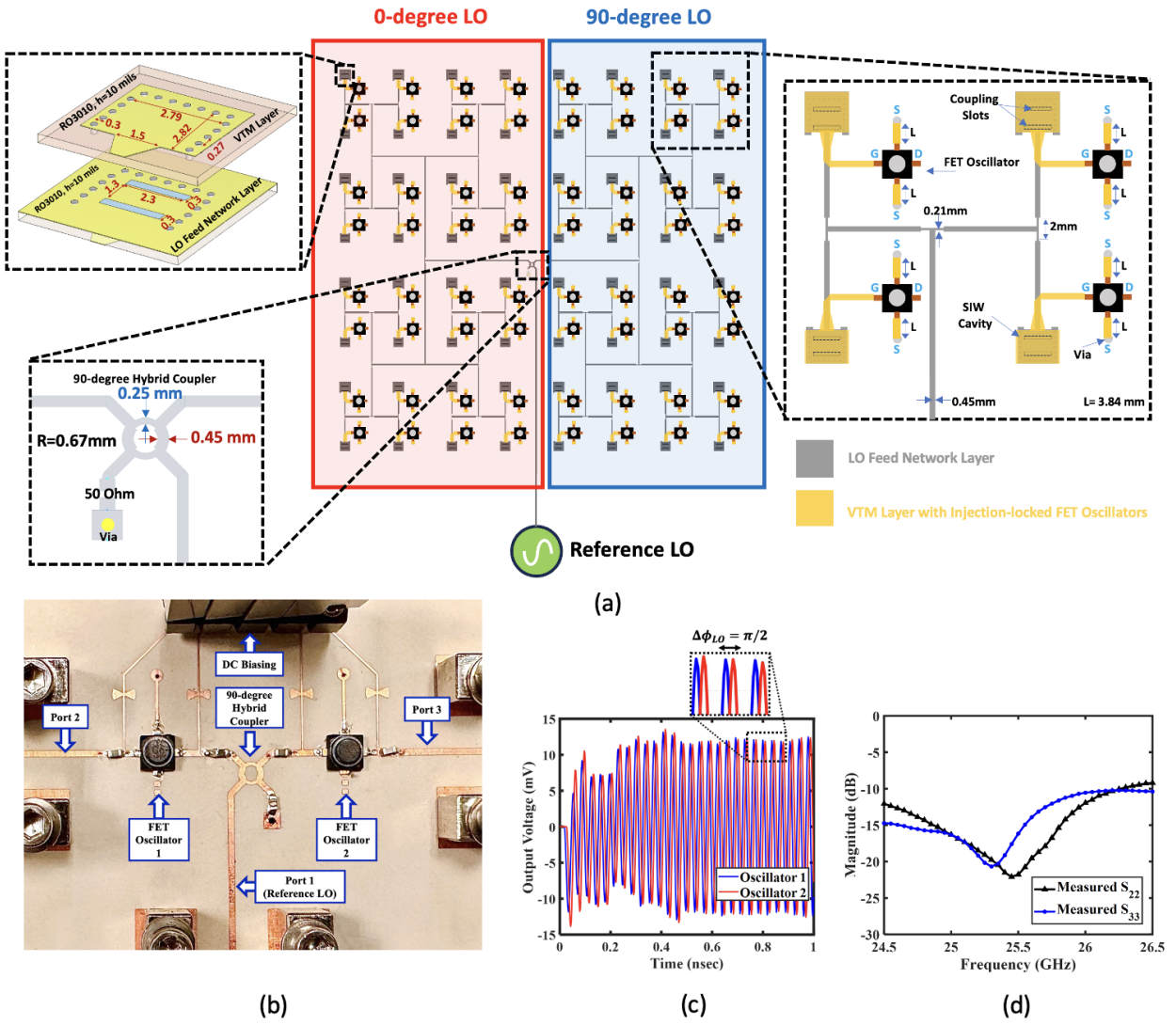

Figure 4.4 (a) The proposed two-layer LO feed network includes a 90-degree hybrid coupler dividing VTM cells into two regions with a 90-degree phase shift relative to each other. A low-power reference LO signal ensures frequency and amplitude synchronization. This signal is distributed via microstrip lines and SIW coupling cavities to stabilize FET oscillators to the desired LO signal. Additionally, biasing of these FET oscillators allows for cell activation/deactivation. (b) Fabricated prototype of two injection-locked oscillators with a 90-degree phase shift. (c) Simulated output voltages of the oscillators. (d) S-parameters of the oscillators.

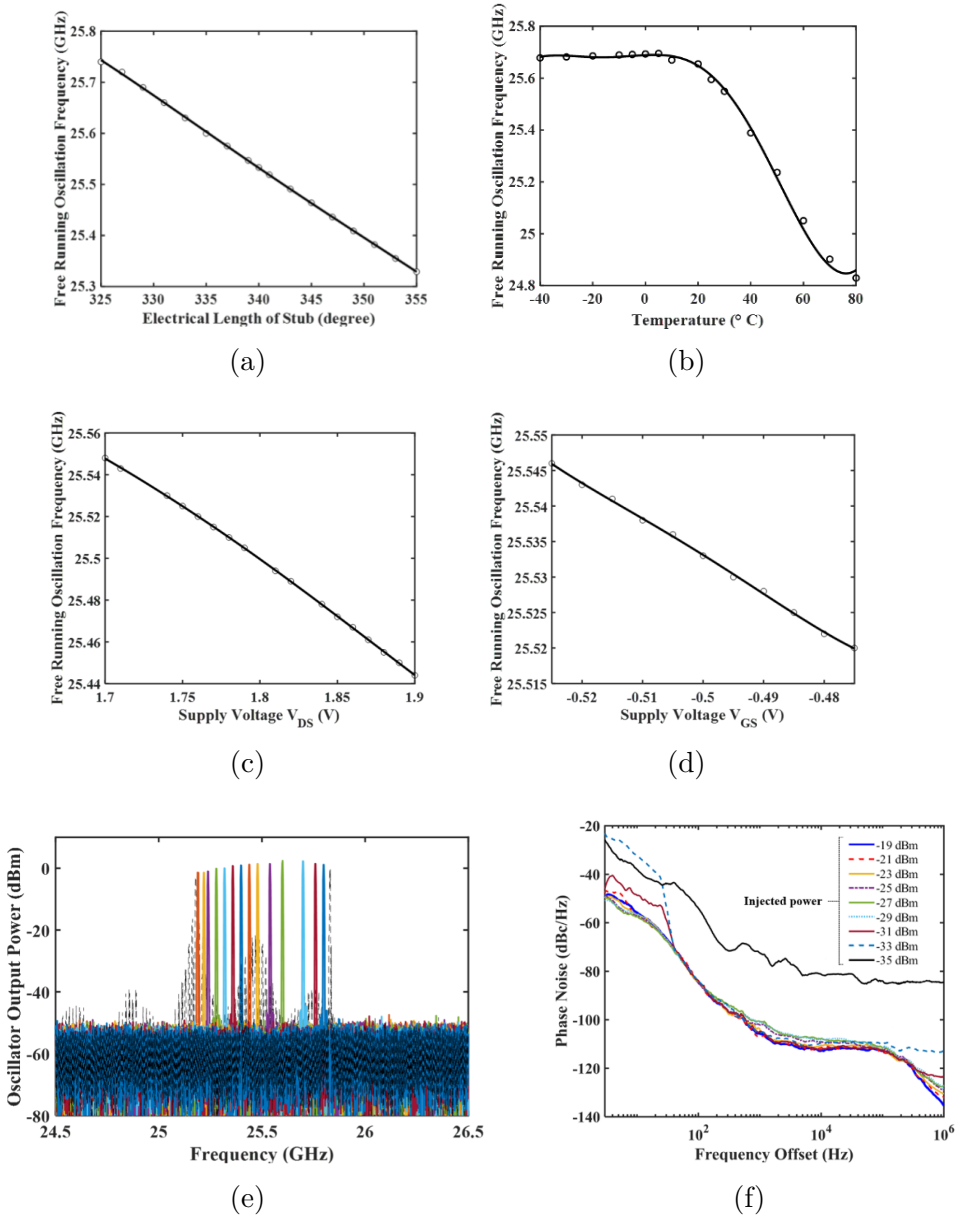

Figure 4.5 Simulation result of parametric study of the proposed oscillator. Variation in free running oscillation frequency considering the change in (a) electrical length of stub. (b) temperature. (c) DC supply voltage V_{DS}, and (d) V_{GS}. (e) Measured injection-locking bandwidth of oscillator for an input power of -28 dBm.(f) Measured phase noise for different power levels of the injected LO signal.

4.2.2 Transmitter Unit-cell (Tx) Modelling

The proposed unit-cell of VTM, as shown in Fig. 4.6, consists of an antenna, a hybrid coupler, an oscillator, and two zero biased power detectors. The FET oscillator in each unit-cell is connected and locked to a reference LO. Consider the following expression for the input LO signal of the first unit-cell

$$S_{LO}(t) = a_{LO}e^{j\omega t} \tag{4.2}$$

where a_{LO} is the amplitude of LO signal and ω is the operational angular frequency and is equal to $2\pi f$. (f is the operational frequency of VTM which in this equations are assumed to be a coherent communication where LO and RF frequencies are the same.) t is also representing time. Then, the output RF signal can be calculated using reflection coefficients from the two ports of the hybrid coupler connected to the power detectors $(\Gamma_1(t), \Gamma_2(t))$ with reference to the injected LO power, which can be obtained as

$$S_{RF_I}(t) = Ka_{LO}[\Gamma_1(t) + \Gamma_2(t)]e^{j\omega t} \tag{4.3}$$

where K is a constant factor identified by the type of power detectors used in the design. Therefore, we can assign the summation of the reflection coefficient in (3) equal to the in-phase component of QAM signal,

$$\Gamma_1(t) + \Gamma_2(t) = \alpha(t)\cos(\theta(t)) = I(t) \tag{4.4}$$

where $\alpha(t)$ and $\theta(t)$ are the modulated amplitude and phase of baseband signals, respectively. As discussed previously, the LO phase of the second unit-cell is set to have a 90-degree phase shift, with the aid of a hybrid coupler. Therefore, the LO signal at the second unit-cell is obtained as follows

$$S_{LO}(t) = ja_{LO}e^{j\omega t} \tag{4.5}$$

Similarly, we can assign the reflection coefficients of the connected power detectors of the second unit-cell $(\Gamma_3(t), \Gamma_4(t))$ to the quadrature component of QAM signal, and the output RF signal can be also calculated as

$$S_{RF_Q}(t) = jKa_{LO}[\Gamma_3(t) + \Gamma_4(t)]e^{j\omega t} \tag{4.6}$$

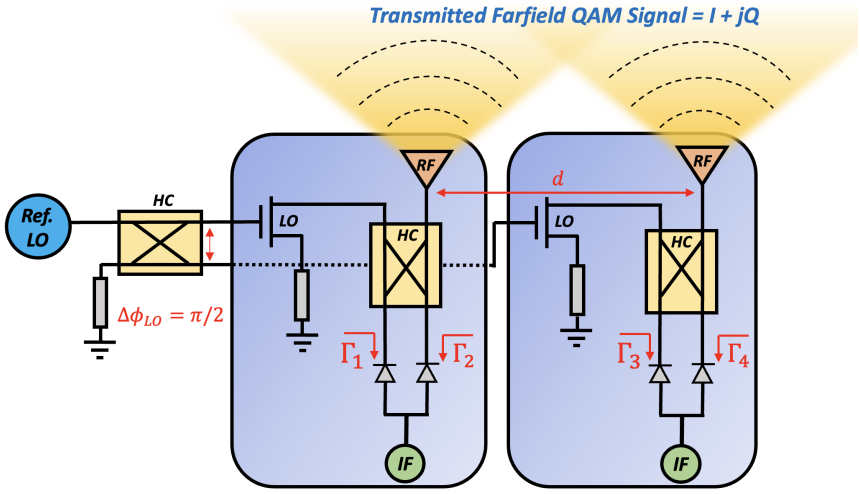

Figure 4.6 Block diagram of VTM unit-cell design for Tx function, including a RF antenna, a hybrid coupler (HC), power detectors, and a local FET oscillator locked to a reference LO signal divided by a 90-degree hybrid coupler. The summation reflection coefficients from each IF source should be equal to in-phase or quadrature components to radiate a total QAM signal.

$$\Gamma_3(t) + \Gamma_4(t) = \alpha(t)\sin(\theta(t)) = Q(t) \tag{4.7}$$

Consequently, each unit-cell will transmit either the in-phase or quadrature components and the summation of both signals will be radiated as a QAM signal. In our proposed transceiver architecture, where IQ signals are combined in the air, the distance d between transmitters or receivers is critical for preventing interference and ensuring effective signal combining. Ideally, this distance should be sufficient to preserve the integrity of individual signal paths and minimize crosstalk. In the designed VTM, we have set the inter-element distance d between cells to one wavelength. This approach helps to minimize coupling effects while enabling a wide range of AoA detection without ambiguity.

4.2.3 Receiver Unit-cell (Rx) Modelling

Fig. 4.7 describes the demodulator design of VTM for a signal with incident angle of AoA. This cell design occupies half the space of a conventional multi-port interferometric receiver. Consequently, two cells forming a channel are approximately the same size as a traditional multi-port receiver. While it may seem that using two antennas and LNAs for a channel increases power consumption, a broader perspective reveals significant advantages in large arrays. The increased number of channels offered by this design outweighs the power costs

when compared to conventional receiver and transmitter architectures. As illustrated in Fig. 4.1, only a few cells are activated for receiving or transmitting functions, allowing the others to remain deactivated and conserve power. Additionally, by employing distributed Rx and Tx cells, we can simultaneously conduct multiple functions, such as AoA detection and polarization detection.

In the case of a coherent receiver, the frequency of carrier on both transmitter and receiver is considered the same. Let's consider the received signal after the LNA of the first unit-cell as

$$S_{RF}(t) = a_{RF}\alpha(t)e^{j(\omega t+\theta(t))} \tag{4.8}$$

where a_{RF} is the amplitude of the received RF signal. If we also consider the injected LO signal as (2), the output signals of 90-degree hybrid coupler ports can then be obtained by

$$\psi_1(t) = \frac{-a_{LO}}{\sqrt{2}}e^{j\omega t}[j\frac{a_{RF}}{a_{LO}}\alpha(t)e^{j\theta(t)} + 1] \tag{4.9}$$

$$\psi_2(t) = \frac{-a_{LO}}{\sqrt{2}}e^{j\omega t}[\frac{a_{RF}}{a_{LO}}\alpha(t)e^{j\theta(t)} + j] \tag{4.10}$$

These two signals are connected to power detectors where their output baseband signals are extracted, which are proportional to their input RF power

$$V(t) = K\left|\psi_i(t)\right|^2, \quad i = 1, 2, 3, 4. \tag{4.11}$$

where K is a constant, determined by the type of power detectors. Accordingly, the output voltages of power detectors are described as follows,

$$V_1(t) = \frac{K{a_{LO}}^2}{2}[1 + (\frac{a_{RF}}{a_{LO}})^2\alpha(t)^2 - 2(\frac{a_{RF}}{a_{LO}})\alpha(t)\sin(\theta(t))] \tag{4.12}$$

$$V_2(t) = \frac{K{a_{LO}}^2}{2}[1 + (\frac{a_{RF}}{a_{LO}})^2\alpha(t)^2 + 2(\frac{a_{RF}}{a_{LO}})\alpha(t)\sin(\theta(t))] \tag{4.13}$$

Using an operational amplifier, the subtraction of the two output voltages will result in the quadrature component of a QAM signal

$$V_D(t) = Q(t) = 2Ka_{LO}a_{RF}[\alpha(t)\sin\theta(t)] \tag{4.14}$$

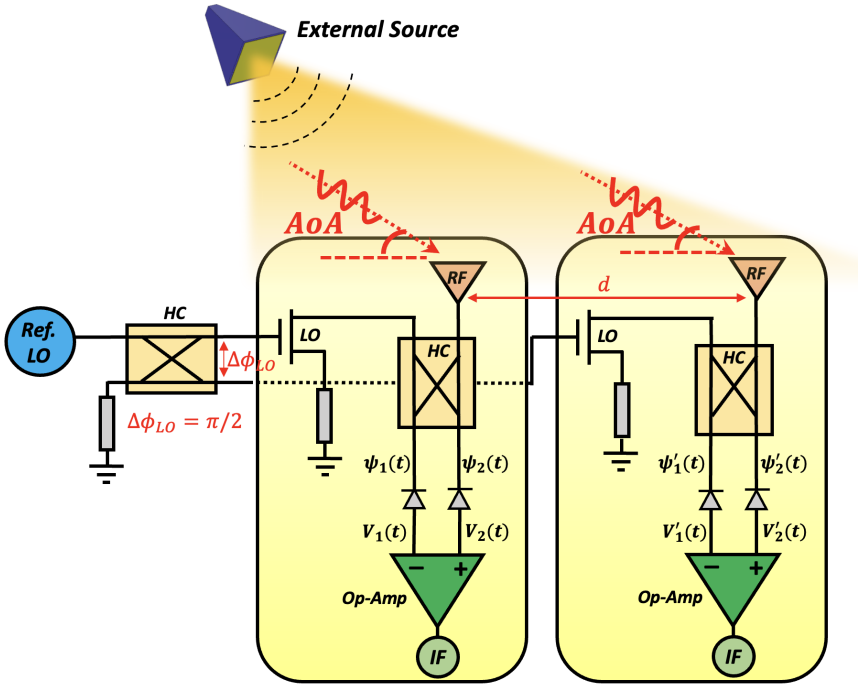

Figure 4.7 Block diagram of VTM unit-cell design for Rx function, including a RF antenna, a hybrid coupler (HC), power detectors, an operational amplifier (Op-Amp), and a local FET oscillator locked to a reference LO signal divided by a 90-degree hybrid coupler. The phase difference of received RF signals between cells should be $2n\pi$ to demodulate the QAM signal.

The phase differences between received signals over two distinct antennas in different cells can be formulated as follows,

$$\Delta\phi_{RF} = \frac{2\pi}{\lambda} d\cos(AoA) \tag{4.15}$$

where d is the inter-element distance between any two cells distributed in the matrix, λ is the operational wavelength, and AoA are the angle of arrivals of the two incident waves. Therefore, we can obtain the RF signal after the antenna of the second unit-cell as

$$S'_{RF}(t) = a_{RF}\alpha(t)e^{j(\omega t+\theta(t))}.e^{j\Delta\phi_{RF}} \tag{4.16}$$

$$S'_{LO}(t) = ja_{LO}.e^{j\omega t} \tag{4.17}$$

Again, after injecting LO power to the hybrid coupler of the second unit-cell, the signals before the power detectors can be obtained as

$$\psi_1^{'}(t) = \frac{-ja_{LO}}{\sqrt{2}} e^{j\omega t}[1 + \frac{a_{RF}}{a_{LO}}\alpha(t)e^{j(\theta(t)+\Delta\phi_{RF})}] \tag{4.18}$$

$$\psi_2^{'}(t) = \frac{a_{LO}}{\sqrt{2}} e^{j\omega t}[1 - \frac{a_{RF}}{a_{LO}}\alpha(t)e^{j(\theta(t)+\Delta\phi_{RF})}] \tag{4.19}$$

Therefore, the output voltages of the power detectors can be calculated by

$$V_1^{'}(t) = \frac{K{a_{LO}}^2}{2}[1 + (\frac{a_{RF}}{a_{LO}})^2\alpha(t)^2 + 2(\frac{a_{RF}}{a_{LO}})\alpha(t)\cos(\theta(t) + \Delta\phi_{RF})] \tag{4.20}$$

$$V_2^{'}(t) = \frac{K{a_{LO}}^2}{2}[1 + (\frac{a_{RF}}{a_{LO}})^2\alpha(t)^2 - 2(\frac{a_{RF}}{a_{LO}})\alpha(t)\cos(\theta(t) + \Delta\phi_{RF})] \tag{4.21}$$

The differential output of the second unit-cell can be written as

$$V_D^{'}(t) = V_1^{'}(t) - V_2^{'}(t) = 2Ka_{LO}a_{RF}[\alpha(t)\cos(\theta(t) + \Delta\phi_{RF})] \tag{4.22}$$

By setting $\Delta\phi_{RF} = 2n\pi$, we can readily find the in-phase components of the QAM signal

$$V_D^{'}(t) = I(t) = 2Ka_{LO}a_{RF}[\alpha(t)\cos(\theta(t))] \tag{4.23}$$

Now, considering a complex vector of $S(t) = I(t) + jQ(t)$, the demodulated signal can be extracted.

The AoA and polarization detection are fundamental to enhancing spatial and polarization diversity, allowing communication systems to harness both dimensions to maximize signal quality, reliability, and SNR while effectively mitigating multipath fading. In environments characterized by significant multi-path propagation, these detection techniques enable the precise differentiation of signal paths, leading to more accurate channel estimation and reduced interference. Furthermore, they significantly enhance channel capacity by facilitating the utilization of multiple independent communication channels, a critical factor for advanced wireless technologies such as 5G and beyond. Additionally, awareness of AoA and polarization plays a pivotal role in interference mitigation by enabling the suppression of unwanted signals, particularly in densely deployed networks. Moreover, by integrating spatial and polarization diversity, these techniques improve spectrum efficiency through more effective frequency reuse, ultimately optimizing the overall network performance. The following two subsections present concurrent polarization and 2-D AoA detection, respectively, which is the first attempt to address this need for simultaneous detection. In summary, concurrent

polarization and AoA detection is key to building robust, efficient, and high-capacity communication systems, addressing the increasing needs for spectrum efficiency and signal reliability in modern wireless networks.

4.2.4 Polarization Detection

The illustrated polarization detection method is outlined in Fig. 4.8. Within the VTM framework, we assume that the antenna polarizations of neighbouring cells are orthogonal to each other, simplistically categorized as horizontal-polarization (H-pol.) and vertical-polarization (V-pol.). This categorization aids in minimizing the coupling between VTM cells during various operations, facilitating polarization detection. Four identical cells, representing H-pol and V-pol configurations, are selected, as depicted in Fig. 4.8. Let's now consider a scenario where a linearly polarized (LP) QAM signal is normally incident on the VTM and is emitted from a source with an arbitrary polarization angle (γ). In VTM cells, employing two orthogonal antennas necessitates the consideration of incident wave components in both horizontal and vertical directions, dictated by the $\cos(\gamma)$ and $\sin(\gamma)$ functions, for horizontally and vertically polarized antennas, respectively. In the polarization detection system, configured with activated H-pol and V-pol cells, the computation of the differential output voltages of activated cells is depicted as follows:

$$H_1(t) = 4Ka_{LO}a_{RF}\cos(\gamma)\alpha(t)\cos(\Delta\theta(t) - \Delta\phi_x - \Delta\phi_z) \tag{4.24}$$

$$H_2(t) = 4Ka_{LO}a_{RF}\cos(\gamma)\alpha(t)\cos(\Delta\theta(t) + \Delta\phi_x + \Delta\phi_z) \tag{4.25}$$

$$V_1(t) = 4Ka_{LO}a_{RF}\sin(\gamma)\alpha(t)\cos(\Delta\theta(t) - \Delta\phi_x - \Delta\phi_z) \tag{4.26}$$

$$V_2(t) = 4Ka_{LO}a_{RF}\sin(\gamma)\alpha(t)\cos(\Delta\theta(t) + \Delta\phi_x + \Delta\phi_z) \tag{4.27}$$

where $\Delta\phi_x$ and $\Delta\phi_z$ are phase shifts alongside the x and z axis, respectively. Consequently, the subtraction and division of 4.24 to 4.27 determines the rotation angle of incident signal as follows

$$\frac{V_1(t) - V_2(t)}{H_1(t) - H_2(t)} = \tan\gamma \tag{4.28}$$

One crucial determinant of accuracy in estimating the polarization is the co-to-cross ratio of the designed antenna within VTM cells. The proposed wideband microstrip antenna comprises an array of rectangular patches arranged in a log-periodic configuration, leveraging the proximity coupling between the microstrip feeding line and the patches (see Fig. 4.9(a)). To enhance operational bandwidth, a scaling factor of k = 1.05 is applied to the patch dimensions ($k = W_i/W_{(i-1)} = L_i/L_{(i-1)} = D_{(i,i+1)}/D_{(i-1,i)}$). Additionally, a loss-free stub

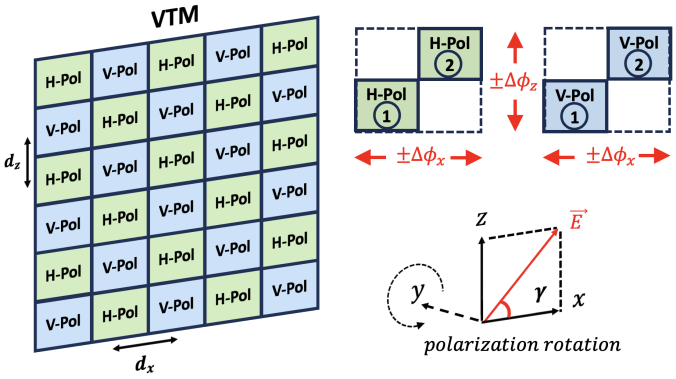

Figure 4.8 Zigzag configuration of antennas in adjacent unit-cells of VTM for polarization detection, aimed at minimizing coupling effects. Four diagonal H-pol and V-pol cells are activated.

with two shorting pins serves as the absorbing terminal, enabling a wide bandwidth operation. The gaps between patches and the feeding line are adjusted with a scaling factor of $k_2 = 1.03$ ($k_2 = G_i/G_{(i-1)}$). While increasing the number of rectangular patches could further broaden the bandwidth, practical considerations, particularly in large-scale designs such as VTM, necessitate a careful dimensioning. Thus, we have limited our design to four patches, striking a balance between bandwidth and scalability.

Figures 4.9(b) and 4.9(c) present the antenna's bandwidth and radiation pattern, respectively. The simulated scattering parameter S11 in Fig. 4.9(b) is related to four patches that are coupled to the narrow transmission line depicted in Fig. 4.9(a). The simulation results of the proposed antenna demonstrate a co-to-cross ratio of 11 dB, sufficiently robust for polarization detection. Additionally, Fig. 4.9(d) demonstrates the measurement results of polarization rotation angle in the entire range of 0 to 90 degrees, with maximum error of 2.8 degrees. The measurement setup will be presented in detail in Section 4.3.

4.2.5 Two-Dimensional (2D) Angle-of-Arrival (AoA) Detection

Based on the design of VTM cells for Tx and Rx functions, AoA detection can be achieved by activating specific cells as depicted in Fig. 4.10 for both horizontally (H-pol) and vertically (V-pol) polarized incident waves. For AoA detection along the z-direction, four cells with H-pol antennas and four cells with V-pol antennas are selectively activated as shown in the green box. The middle cells serve as phase references set to zero, ensuring that the phase differences with the associated cells are equal to $\pm\Delta\phi_z$ and $\pm 2\Delta\phi_z$. This activation scheme is mirrored for cells oriented along the x-direction, shown in red box. Considering first the AoA detection in z-direction, the received RF signals for the activated unit-cell have phase

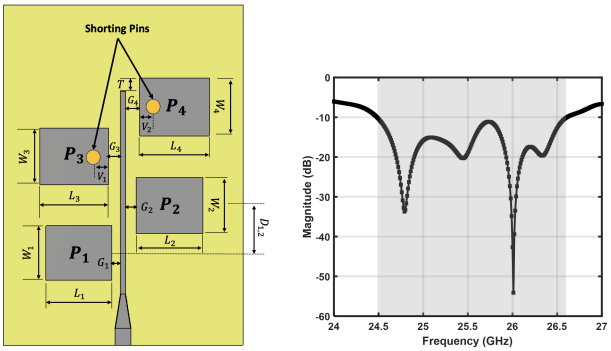

(a) (b)

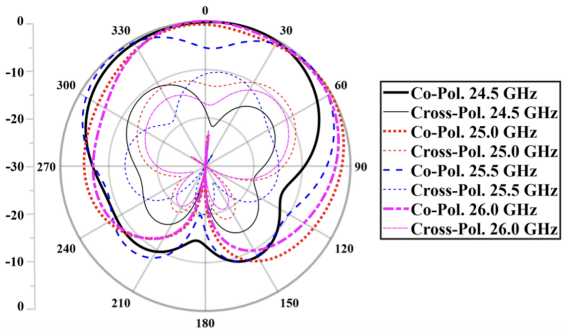

(c)

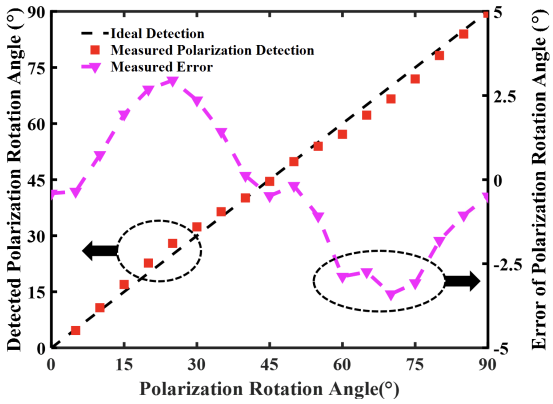

(d)

Figure 4.9 (a) Proposed microstrip antenna with shorting pins. (b) Scattering parameter of the proposed antenna. (c) Radiation pattern of co- and cross-polarization radiations at different frequencies (d) Measurement results with error of polarization detection of arbitrary incident QAM signal.

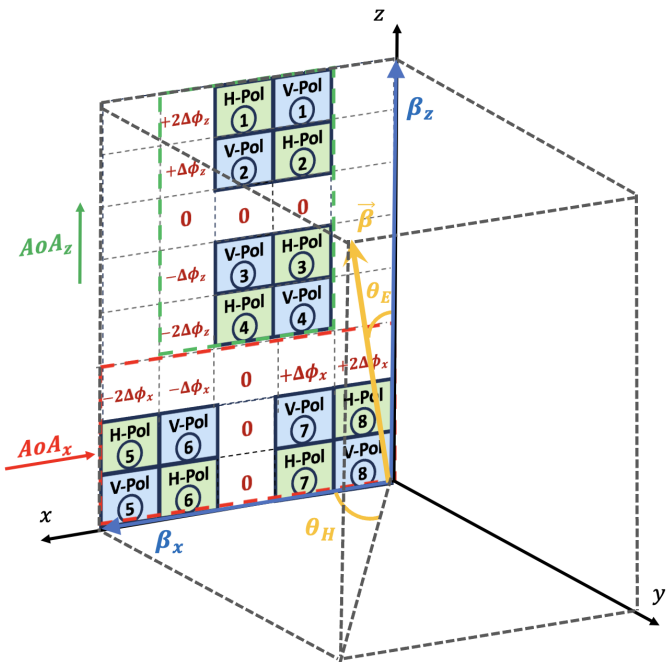

Figure 4.10 Cells activated for 2D AoA detection in the VTM for any arbitrary incident QAM signal.

shifts with reference to the reference unit-cell, which can be obtained as

$$S_{RF,i}(t) = a_{RF}\alpha(t)e^{j(\omega t+\theta(t)+i\Delta\phi_{RF})} \tag{4.29}$$

where $i = -2, -1, +1, +2$. Therefore, the output signals of 90-degree hybrid coupler ports of each unit-cell can be obtained as

$$\psi_{1,i}(t) = \frac{-a_{LO}}{\sqrt{2}}e^{j\omega t}[j\frac{a_{RF}}{a_{LO}}\alpha(t)e^{j(\theta(t)+i\Delta\phi_{RF})} + 1] \tag{4.30}$$

$$\psi_{2,i}(t) = \frac{-a_{LO}}{\sqrt{2}}e^{j\omega t}[\frac{a_{RF}}{a_{LO}}\alpha(t)e^{j(\theta(t)+i\Delta\phi_{RF})} + j] \tag{4.31}$$

Consequently, their output voltages of power detectors can also be generated as

$$V_{1,i}(t) = \frac{K{a_{LO}}^2}{2}[1 + (\frac{a_{RF}}{a_{LO}})^2\alpha(t)^2 + 2(\frac{a_{RF}}{a_{LO}})\alpha(t)\sin(\theta(t) + i\Delta\phi_{RF})] \tag{4.32}$$

$$V_{2,i}(t) = \frac{K{a_{LO}}^2}{2}[1 + (\frac{a_{RF}}{a_{LO}})^2\alpha(t)^2 - 2(\frac{a_{RF}}{a_{LO}})\alpha(t)\sin(\theta(t) + i\Delta\phi_{RF})] \tag{4.33}$$

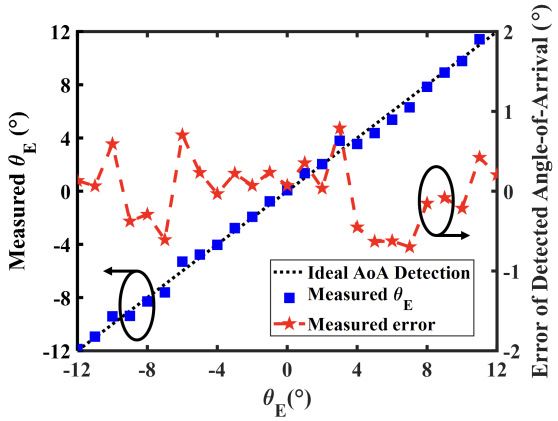

(a)

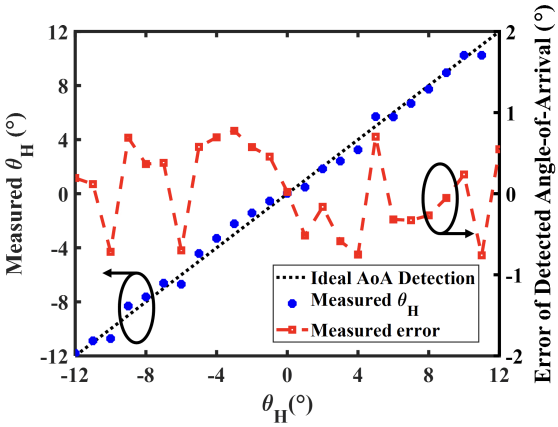

(b)

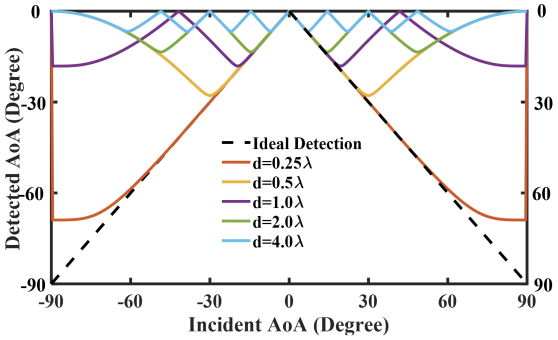

(c)

Figure 4.11 Measurement results of 2D AoA detection for both (a) altitude and (b) azimuth angles. (c) Unambiguity range of AoA detection for different inter-element distances of cells.

Therefore, the differential form of these voltages are

$$V_{D,i}(t) = 2Ka_{LO}a_{RF}[\alpha(t)\sin(\theta(t) + i\Delta\phi_{RF})] \quad , i = -2, -1, 1, 2 \tag{4.34}$$

After some trigonometric calculations, we can obtain the phase difference of RF signal between adjacent activated unit-cells of the AoA detector system

$$\Delta\phi_z = \cos^{-1}\left(\frac{V_{D,+2} - V_{D,-2}}{2(V_{D,+1} - V_{D,-1})}\right) \tag{4.35}$$

This phase difference is dependent on three factors of the inter-element distance of VTM unit-cells (d), wavelength (λ) and AoA, as expressed in (15). Hence, according to Fig. 4.10, the detected AoA in one direction can be simply obtained by

$$AoA_z = \cos^{-1}\left(\frac{\lambda}{2\pi d}\cos^{-1}\left(\frac{V_{D,4} - V_{D,1}}{2(V_{D,3} - V_{D,2})}\right)\right) \tag{4.36}$$

Using the similar procedure, the AoA in x-direction can be obtained as

$$AoA_x = \cos^{-1}\left(\frac{\lambda}{2\pi d}\cos^{-1}\left(\frac{V_{D,8} - V_{D,5}}{2(V_{D,7} - V_{D,6})}\right)\right) \tag{4.37}$$

Fig. 4.11(a) and Fig. 4.11(b) show the measurement results of AoA detection in both azimuth and elevation angles, in the range of -12 to 12 degree with a maximum detected error of 0.9 degree. The specified range of measurement for both azimuth and elevation angles represents the achievable unambiguous range. This ambiguity beyond this range arises from the mathematical properties of the inverse cosine function 4.36 and 4.37, rather than any limitations of the fabricated prototype. To increase the unambiguous range with acceptable detection error, we need to decrease the inter-element distance d between VTM cells as illustrated in Fig. 4.11(c).

In this proof-of-concept design, LNAs and PAs were not included. Incorporating these components would require an additional area. In a practical end-user product, where LNAs and PAs are integrated, it is essential to balance the trade-off between the unambiguous AoA detection range for sensing and the mutual coupling between antennas in adjacent unit cells. Fig. 4.12 presents the relationship between the unambiguous AoA detection range and mutual coupling for different inter-element distances. The findings suggest that an inter-element spacing close to one wavelength is ideal for achieving robust and simultaneous communication and sensing.

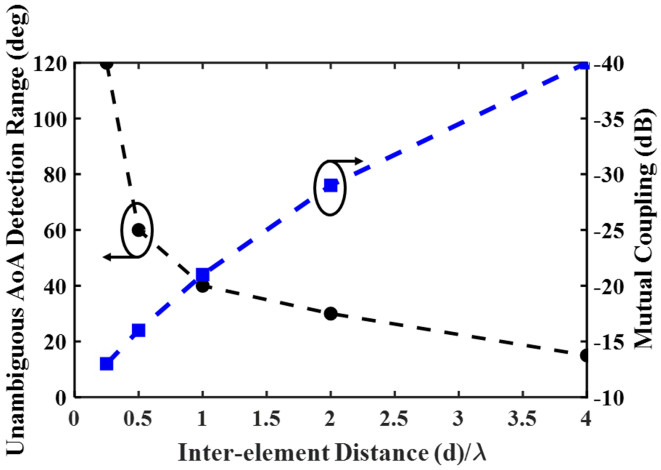

Figure 4.12 Trade-off analysis between unambiguous range of AoA detection and mutual coupling for different inter-element distances (d/λ).

4.2.6 Polarization Mismatch Calibration Method

In cases of polarization mismatch, applying a calibration factor is essential to optimize the demodulation process. Referring to the horizontal and vertical cells illustrated in Fig. 4.8, we can derive the following equations for their signal powers, taking into account a polarization rotation of γ.

$$S_{H_1}(t) = a_{RF}\alpha(t)e^{j(\omega t+\theta(t)-\Delta\phi_x+\Delta\phi_z)}.\cos\gamma \tag{4.38}$$

$$S_{V_1}(t) = a_{RF}\alpha(t)e^{j(\omega t+\theta(t)+\Delta\phi_x+\Delta\phi_z)}.\sin\gamma \tag{4.39}$$

$$S_{H_2}(t) = a_{RF}\alpha(t)e^{j(\omega t+\theta(t)+\Delta\phi_x-\Delta\phi_z)}.\cos\gamma \tag{4.40}$$

$$S_{V_2}(t) = a_{RF}\alpha(t)e^{j(\omega t+\theta(t)-\Delta\phi_x-\Delta\phi_z)}.\sin\gamma \tag{4.41}$$

Then, the output voltages for each cell can be expressed as follows

$$V_{H_1}(t) = 2Ka_{LO}a_{RF}[\cos\gamma.\alpha(t)\cos(\theta(t)-\Delta\phi_x+\Delta\phi_z)] \tag{4.42}$$

$$V_{V_1}(t) = 2Ka_{LO}a_{RF}[\sin\gamma.\alpha(t)\cos(\theta(t)+\Delta\phi_x+\Delta\phi_z)] \tag{4.43}$$

$$V_{H_2}(t) = 2Ka_{LO}a_{RF}[\cos\gamma.\alpha(t)\cos(\theta(t)+\Delta\phi_x-\Delta\phi_z)] \tag{4.44}$$

$$V_{V_2}(t) = 2Ka_{LO}a_{RF}[\sin\gamma.\alpha(t)\cos(\theta(t)-\Delta\phi_x-\Delta\phi_z)] \tag{4.45}$$

By subtracting these output voltages, we obtain

$$V_{H_1}(t) - V_{H_2}(t) = 4Ka_{LO}a_{RF}[\cos\gamma.\alpha(t)(\sin\Delta\phi_x+\Delta\phi_z)] \tag{4.46}$$

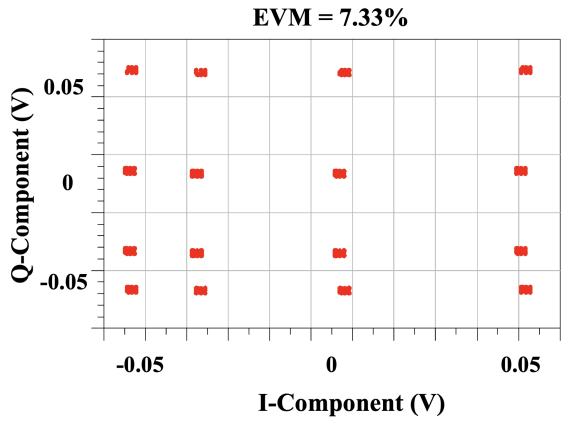

(a)

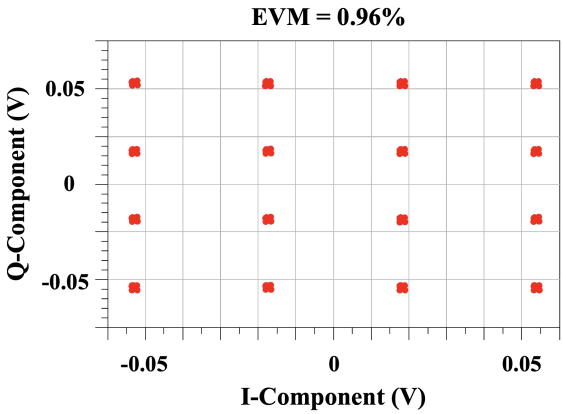

(b)

Figure 4.13 Simulation results of demodulated 16-QAM constellations when Rx process data at 200-MS/s data rate, and for incident polarization with rotation angle of 30 degrees. (a) Without calibration. (b) With calibration.

$$V_{V_2}(t) - V_{V_1}(t) = 4Ka_{LO}a_{RF}[\sin\gamma.\alpha(t)(\sin\Delta\phi_x - \Delta\phi_z)] \tag{4.47}$$

Now, using the calibration factors of ξ_1 and ξ_2, we can recover demodulation of quadrature component of incident QAM signal

$$Q(t) = \xi_1(V_{H_1}(t) - V_{H_2}(t)) - \xi_2(V_{V_2}(t) - V_{V_1}(t)) \tag{4.48}$$

where calibration factors are defined as

$$\xi_1 = \frac{1}{\cos\gamma}, \quad \xi_2 = \frac{1}{\sin\gamma} \quad for \quad 0 < \gamma < \pi/2 \tag{4.49}$$

For the in-phase component, another set of four horizontal and vertical cells are required with LO phase of 90-degrees.

$$I(t) = \xi_1(V_{H_1}^{'}(t) - V_{H_2}^{'}(t)) - \xi_2(V_{V_2}^{'}(t) - V_{V_1}^{'}(t)) \tag{4.50}$$

Fig. 4.13 shows the constellation of demodulated incident 16-QAM signal before and after calibration technique for a polarization rotation of $\gamma = \pi/6$.

4.3 Measurement Setup and Experimental Results

In this section, we present the experimental setup, methodologies employed, and detailed measurement results obtained for the proposed sensing and communication VTM front-end developed for AoA and polarization detection. First, the geometric configuration of the utilized power detector is presented in Fig. 4.14(a), which is designed on a thin Rogers RO3010 substrate with ϵ_r=10.2 and thickness of 10 mils with 17μm metallization. This power detector circuit consists of an input impedance matching network, a zero-biased GaAs Schottky diode, and a low pass (LP) filter. Harmonic balance (HB) simulator of Keysight Advanced Designed System (ADS) and the full-wave simulator of Computer Simulation Technology (CST) were utilized to accurately model and predict the behavior of the power detector. Fig. 4.14(b) shows the output voltages of power detector versus its input power for different operational frequencies. The linear increment of output power from -40 to 0 dBm for almost all the frequency points shows the practical dynamic range of the proposed system. The limited dynamic range of receivers is inherent in the interferometric technology we implemented. This limitation can be addressed by integrating other common receiver architectures within the VTM cell. However, it is important to note that the cost of fabricating a VTM remains relatively low since it is based on mostly passive interferometric-based technique.

The primary function of the VTM is to dynamically adjust the configurations of associated sensors, transmitters, and receivers within the reconfigurable matrix. This adaptability enables the VTM to respond in real-time to the changing conditions and characteristics of incoming signals. Fig. 4.15(a) provides a 3D perspective of the VTM, illustrating a hypothetical scenario of cell associations at a specific moment, which will evolve over time. To facilitate a deeper understanding of the proposed architecture's operation, we illustrate the allocation of cells in conjunction with their associated applications.

According to the proposed block diagram in section II, the designed VTM cell, (Fig. 4.15(d)), contains a microstrip antenna with $\pm 45^{\circ}$ rotation to receive and transmit QAM signals with two perpendicular polarizations in adjacent VTM cells, a hybrid coupler, an oscillator

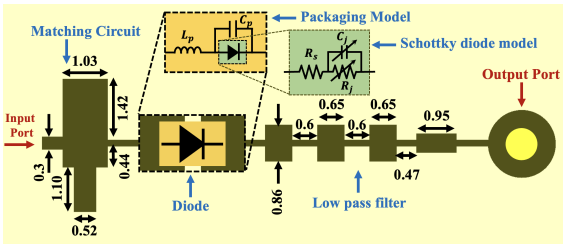

(a)

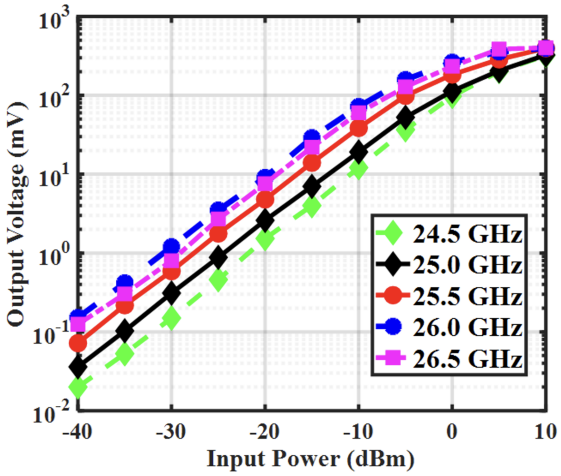

(b)

Figure 4.14 (a) Geometric configuration of the designed microwave power detector. (b) Output voltage of power detector with sweeping input power from -40 to 10 dBm.

using CE3520K3-C1 RF FET transistor, two power detectors, and a Substrate Integrated Waveguide (SIW) coupling cavity for distributing reference LO signal. A matching network before the power detectors ensures detectable output voltage levels, and a low pass filter after the power detector is provided to suppress high order harmonics. Fig. 4.15(b) and Fig. 4.15(c) show the fabricated prototype of the LO feed network and VTM layers, respectively.

The measurement setup of the VTM, as shown in Fig. 4.15(e) and Fig. 4.15(f), are conducted with Keysight UXR0702AP Real-Time Oscilloscope, an Agilent E8257D PSG Analog Signal Generator, and a Keysight Arbitrary Waveform Generator (AWG) M8196A. To synchronize the RF and reference LO signals, a 10 MHz synchronization signal is applied to both signal generators and analyzers. The fabricated prototype is located on a 2D rotational platform displaying the rotated degrees in both azimuth and elevation angles for 2D AoA detection purposes. As stated in Section I, numerous combinations of unit-cells can form a virtual transceiver channel. For the measurement results, arbitrary combinations of two-cells are considered for receiving and transmitting QAM signals with different modulation orders at a

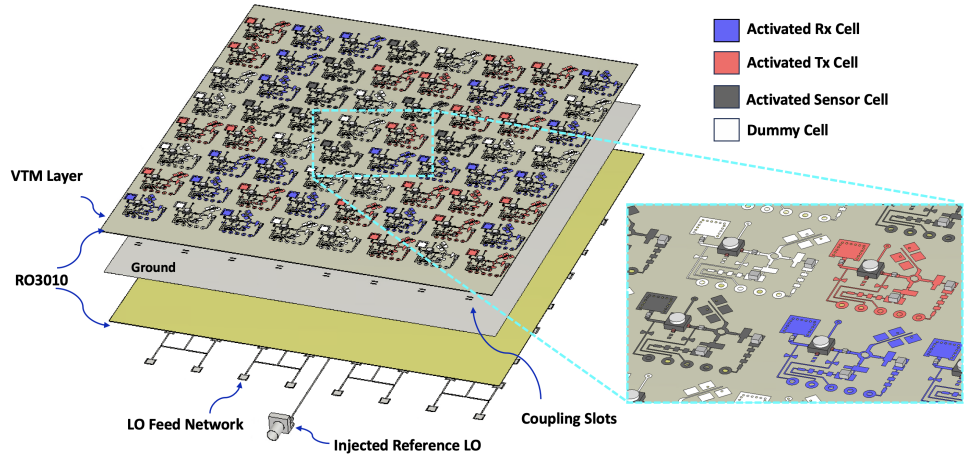

(a)

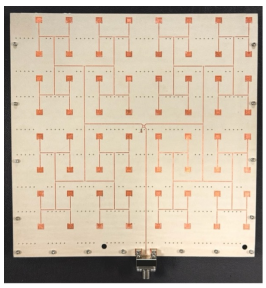

(b)

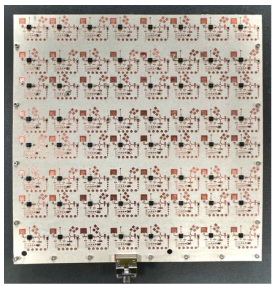

(c)

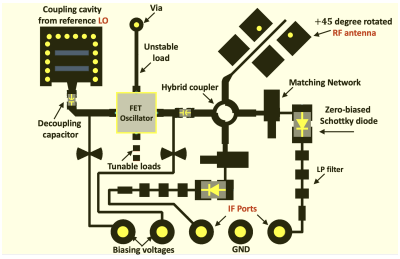

(d)

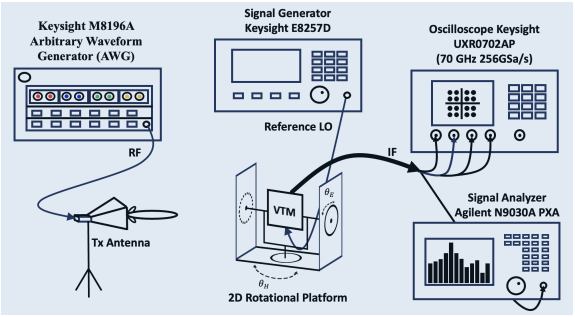

(e)

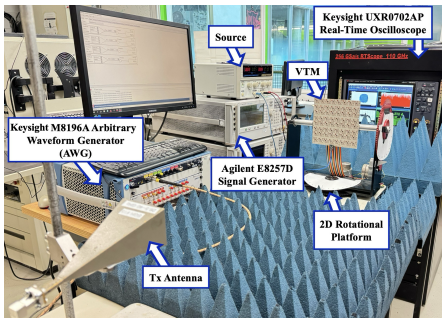

(f)

Figure 4.15 (a) 3D perspective of interferometric design of VTM and LO feeding network with activated Rx, Tx, and sensor cells. Fabricated prototype of the proposed sensing and communication VTM front-end (b) bottom view (c) top view. (d) Designed VTM unit-cell comprising ±45 degree rotated antenna. Measurement setup test bench for the fabricated VTM prototype (e) block diagram (f) photograph of the test setup.

maximum symbol rate of 250 Msps. As can be seen in Table. 4.1, the extracted EVM of less than -29.95 dB is achieved for the cases of 64-QAM and 128-QAM receiving and transmitting functions. The power consumption primarily stems from the DC biasing of injection-locked oscillators, with each activated cell consuming approximately 15 mW. The final dimensions of the 64-element VTM array are 15 cm x 15 cm, and the measured sensitivity of the VTM sensors is approximately -48 dBm which is comparable with other reported interferometric-based receivers [65], considering the fact that low noise amplifier (LNA) is not included in this design.

In the fabricated proof-of-concept prototype of the multifunctional VTM, the LNA and PA were not included. However, their inclusion would affect both the total power consumption and the occupied area. Based on a footprint analysis of commercially available mmW LNAs and PAs, the total area occupied by each unit cell of the VTM on a single-layer PCB would be 450 mm^2. Regarding power consumption, since receiving and transmitting QAM signals require two cells, the total power consumption for the Rx operation would be 1.3 W, while for the Tx function, it would be 7.5 W. The transmitted output power from one unit-cell of the VTM is measured -3 dBm which can be improved by utilizing a PA to increase the range of sensing and communications. Considering the gain of each antenna 4.96 dBi, the EIRP is calculated as 1.96 dBm. It is worth mentioning that the proposed work is a proof-ofconcept that leverages the multifunctional VTM concept. In a real application scenario, however, the above-reported EIRP of each unit-cell can be significantly improved by implementing appropriately a PA. In the same connection, the link distance would be improved by implementing a LNA on the Rx side.

Fig. 4.16 shows the simulation and measurement results for noise figure of the VTM. It is observed that that the simulated NF are about 13.5 and 8.3 at 25.0 and 26.0 GHz, respectively. Measured NF are also 14.3 and 11.7 dB at 25.0 and 26.0 GHz, respectively. Table. 4.2 summarizes the measured results and provides a comparison with other state-of-the-art interferometric and phased array transceivers. The proposed architecture is the first interferometric-based multifunctional transceiver that integrates both communication and sensing capabilities simultaneously. By leveraging the advantages of the VTM, the proposed transceiver supports the realization of multiple channels. As a result, it enables the concurrent detection of 2D AoA and polarization, setting it apart from conventional transceivers as shown in references [172–175]. Furthermore, the VTM-based transceiver delivers acceptable performance in terms of data rates, EVM, and BER, all without the need for post-processing. It also achieves high power efficiency through its interferometric architecture. These results alongside with the measurement results of polarization and 2D AoA detection system, confirm the good performance of the proposed concurrent sensing and communication VTM

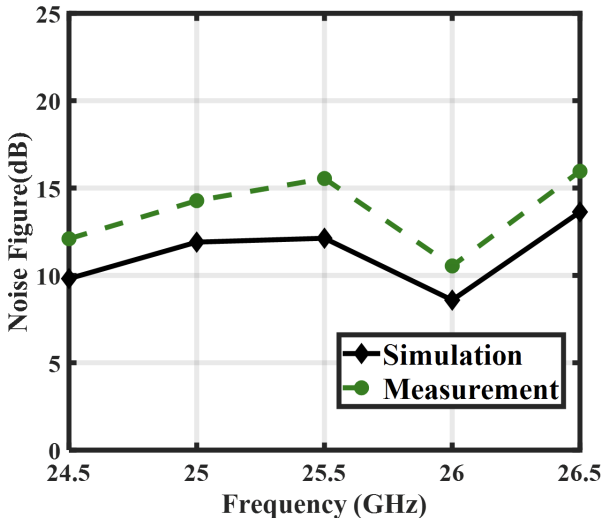

Figure 4.16 Simulated and measured noise figure (NF) of the proposed VTM.

architecture. The table also includes some advanced chip-level phased array transceivers for comparison. Notably, the principle of the proposed VTM technique is not limited to the printed circuit board (PCB) and can be extended for an integrated circuit (IC) chip implementation for large-scale THz transceiver arrays, offering potential for even higher performance [176]. The operational BW is another important factor which is measured at 24.5 to 26.5 GHz. This limitation is not coming from the VTM itself, rather it is just related to interferometric design of VTM cells and can be improved by properly incorporating ultra-wideband interferometric multi-port junctions.

4.4 Conclusion

In summary, the introduction of VTM (Virtual Transceiver Matrix) topology represents a paradigmatic advancement in wireless communication architectures. By distributing transceiver cells across a 2D matrix space and leveraging phase differentials in RF and LO signals, the VTM architecture facilitates efficient modulation/demodulation of QAM signals, alongside pivotal functionalities such as AoA and polarization detection. The dynamic synthesis of channels and virtual transceiver capabilities are set to promise a seamless integration of multiple functionalities, remarkedly enhancing transceiver capacity and agility compared to conventional architectures. Mathematical formulations and proof-of-concept experiments have robustly validated the operational efficacy of VTM, underscoring its transformative potential for next-generation wireless systems, including 5G/6G and beyond.

Table 4.1 Measured Normalized Constellation Diagrams With Different Orders of Modulation (M-QAM) for Receiver and Transmitter Functions

Modulation Order	**Rx**	**Rx**	**Tx**	**Tx**
Activated Cells	M_{11}&M_{12}	M_{42}&M_{62}	M_{14}&M_{15}	M_{23}&M_{26}
4-QAM	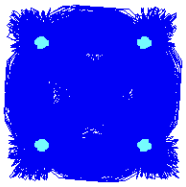	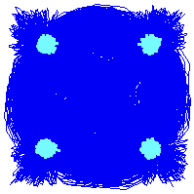	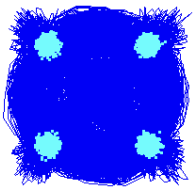	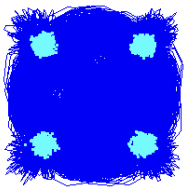
EVM (rms)	4.49 %	6.12 %	8.58 %	8.45 %
Activated Cells	M_{33}&M_{73}	M_{88}&M_{85}	M_{74}&M_{75}	M_{45}&M_{46}
16-QAM	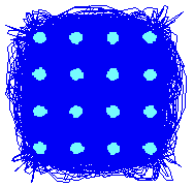	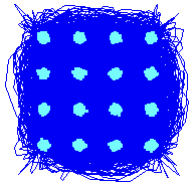	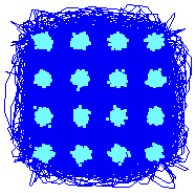	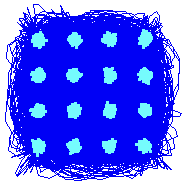
EVM (rms)	3.54 %	3.84 %	5.57 %	4.57 %
Activated Cells	M_{61}&M_{71}	M_{77}&M_{37}	M_{62}&M_{66}	M_{24}&M_{25}
32-QAM	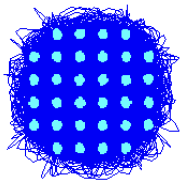	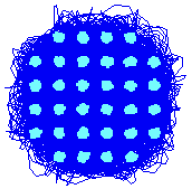	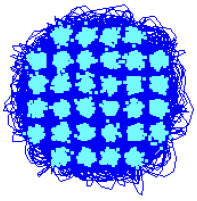	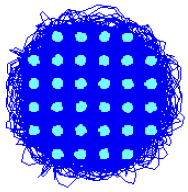
EVM (rms)	2.93 %	3.09 %	5.87 %	2.97 %
Activated Cells	M_{81}&M_{83}	M_{44}&M_{54}	M_{84}&M_{88}	M_{64}&M_{65}
64-QAM	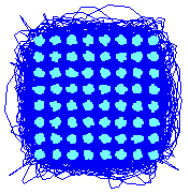	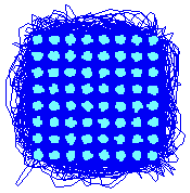	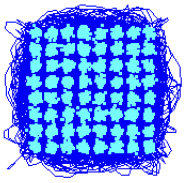	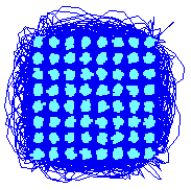
EVM (rms)	2.97 %	2.93 %	4.56 %	3.18 %
Activated Cells	M_{14}&M_{24}	M_{32}&M_{36}	M_{55}&M_{57}	M_{37}&M_{33}
128-QAM	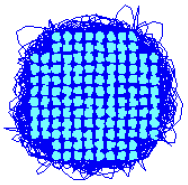	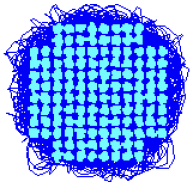	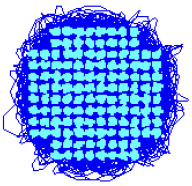	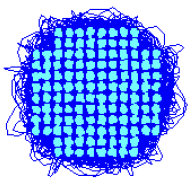
EVM (rms)	2.59 %	2.74 %	2.76 %	2.53 %

Table 4.2 Performance Summary and Comparison with the State-of-the-Art Receivers/Transmitters/Sensors

Reference	**Architecture**	**Modulation Type**	**Frequency (GHz)**	**Symbol Rate**	**EVM (dB)**	**Communication Function (Rx & Tx)**	**Sensing Function (AoA & Pol.)**
[161], TMTT 2013	Interferometric-based PCB	16-QAM/64-QAM	2.5/3.0	2 Msps	-34.89/-34.42	Single Rx	No
		LTE/WCDMA	2.5/3.0	3 Msps/3.84 Msps	-33.97/-34.42		
[91], TMTT 2021	Interferometric-based PCB	M{4,16,64,256}	3.38/3.82	5 Msps	-33.97	Single Rx	No
[169], MWCL 2009	Interferometric-based PCB	QPSK	2.45	200 Ksps	-24.58	Single Rx	No
[118], TMTT 2019	Interferometric-based PCB	4-QAM	5	2 Msps	-26.93	Single Rx	No
		16-QAM	5	4 Msps	-22.49		
		32-QAM	5	5 Msps	-19.9		
[20], TMTT 2023	Interferometric-based PCB	4-QAM	28	1 Msps	-24.22	5×5 Rx	Yes
		16-QAM			-28.83		
		32-QAM			-26.19		
[96], TCSI 2023	Interferometric-based PCB	4-QAM	24/28	5 Msps	-29.52/-28.26	Single Rx	No
		16-QAM			-30.47/-30.73		
		32-QAM			-30.12/-30.31		
		64-QAM			-28.81/-29.37		
[170], TMTT 2013	Interferometric-based PCB	64-QAM	2.5	-/-	-21.94	Single Rx	No
[19], TMTT 2022	Interferometric-based PCB	4-QAM	3.6	10 Msps	-27.62	Single Tx	No
		16-QAM			-27.86		
		32-QAM			-27.67		
		64-QAM			-27.66		
[171], MOTL 2010	Interferometric-based PCB	16-QAM	6–9	100/500 Mbit/s	-/-	Single Rx/Tx	No
		64-QAM					
[16], MWCL 2018	Interferometric-based PCB	4-QAM	2.9 / 2.68	10/20 Mbd	-33.98	Single Rx/Tx	No
		16-QAM					
[151], TMTT 2021	Mixer-based Phased Array Chip	QPSK	37.5–39.5	1.6 Gb/s	-22.11	8×4Tx & 4×4Rx	NA
		16-QAM		3.2 Gb/s	-22.23		
		64-QAM		3.6 Gb/s	-27.79		
		256-QAM		1.6 Gb/s	-34.38		
[172], TMTT 2023	Mixer-based Phased Array Chip	QPSK	33.5–37.5	200 Msps	-26.07/-28.22	4 TRx	NA
		16-QAM			-28.16/-29.66		
		64-QAM			-28.83/-30.40		
[173], TMTT 2021	Mixer-based Phased Array Chip	64-QAM	24–28	2.4 Gb/s	-31.4	4 TRx	NA
		256-QAM			-30.8		
[174], TMTT 2023	Mixer-based Phased Array Chip	NA	28	NA	NA	4 TRx	NA
[102], TMTT 2017	Interferometric-based PCB	–	55–62	–	–	No	Yes
[61], TIM 2023	Interferometric-based PCB	–	6.0–8.25	–	–	No	Yes
[113], TIM 2023	Interferometric-based PCB	–	30	–	–	No	Yes
[This work]	**Interferometric-based PCB**	**64-QAM (Rx)**	**24.5–26.5**	**250 Msps**	**-30.54**	**8×8 TRx**	**Yes**
		128-QAM (Rx)		**120 Msps**	**-31.24**		
		64-QAM (Tx)		**250 Msps**	**-26.82**		
		128-QAM (Tx)		**120 Msps**	**-31.18**		

CHAPTER 5 A MILLIMETER-WAVE 4D AUTOMOTIVE JOINT RADAR COMMUNICATION FOR ACCURATE MULTI-TARGET DETECTION IN HIGH DENSITY ENVIRONMENTS

In this paper, a millimeter-wave (mmW) 4D joint radar-communication system leveraging the Virtual Transceiver Matrix (VTM) architecture is proposed and presented. This system is developed for accurate detection, separation, and tracking of multiple automotive targets in high-density scenarios such as urban traffics and intersections. The VTM-based approach enhances spatial diversity and enables multi-dimensional sensing using compact passive RF front-ends. Our system simultaneously extracts 2D angle-of-arrivals (AoA), range, Doppler velocity, and communication symbols using a unified analog circuitry. Through both simulation and experimentation, we demonstrate that the proposed architecture achieves superior angular resolution, robust velocity estimation, and reliable communication under dense cluttered conditions. Key performance results include multi-target separation below 5° angular spacing, Doppler accuracy under 1.7 m/s error, and low bit error rate in 64-QAM communication recovery. The results confirm the VTM-RadCom paradigm as a promising direction for scalable, energy-efficient, and high-accuracy sensing and communication in next-generation connected automotive platforms and integrated sensing and communication (ISAC) systems.

5.1 Introduction

Radar systems have emerged as a cornerstone technology in the evolution of advanced driver assistance systems (ADAS) and autonomous vehicles, offering reliable sensing capabilities that enhance safety, perception, and navigation performance in diverse environmental conditions. Among the sensing modalities—including LiDAR, optical cameras, and ultrasonic sensors—millimeter-wave (mmW) radar has demonstrated distinct advantages such as compactness, robustness to adverse weather, high velocity resolution, and long-range target detection, making it indispensable in modern vehicular sensing platforms [177–179]. Conventional automotive radar systems, typically based on 3D sensing architectures, are proficient in detecting object range, Doppler velocity, and azimuth angle. However, their inability to accurately resolve the elevation angle constrains the system's ability to fully reconstruct a target's spatial location. This limitation becomes critical in congested urban environments or multi-level roadways, where vertical discrimination is essential for obstacle differentiation and safety-critical decision-making [180]. The rise of 4D radar systems—defined by their capacity to detect range, azimuth, elevation, and velocity—has thus become a key enabler

for high-resolution environmental perception [181, 182].

Recent advances in multiple-input multiple-output (MIMO) technology and array signal processing have made high-resolution 4D radar systems feasible. High-density virtual antenna arrays have been employed to achieve finer angular resolution, often through uniform planar arrays (UPAs) or sparse array configurations [183]. Despite their enhanced performance, these systems typically suffer from excessive hardware complexity, increased power consumption, and large data throughput, which challenge the real-time signal processing requirements of embedded automotive platforms [184]. Meanwhile, classical implementations for radar and communication often lack the spatial diversity required for accurate direction-of-arrival (DoA) estimation and rely heavily on digital post-processing, which introduces latency and demands high computational power.

The more recently proposed Virtual Transceiver Matrix (VTM) addresses these challenges by performing spatial combining and signal decomposition directly in the analog domain, minimizing power consumption and simplifying the digital baseband interface while supporting simultaneous sensing and communication functions [20, 21]. By unifying these roles within a single front-end, the VTM naturally enables integrated sensing and communication (ISAC) operation, which is increasingly important for 5G/6G-connected vehicles and cooperative automotive perception systems [1].

This paper introduces a multifunctional 4D joint radar and communication (RadCom) system based on the VTM architecture, experimentally validated at 24 GHz for automotive sensing and connectivity, as conceptually illustrated in Fig. 5.1. The proposed platform combines a reconfigurable 2D matrix of passive transceiver cells, enabling simultaneous range, Doppler, and 2D angle-of-arrival (AoA) detection along with high-order QAM demodulation. The proposed distributed topology leverages spatial interference across analog cells, eliminating the need for phase shifters, active switching, or digital beamforming, while maintaining compactness, low power consumption, and scalability.

A distinctive advantage of the proposed VTM-based RadCom lies in its inherently large number of possible sensing and communication channels that arise from the matrix interconnection of its analog cells. Unlike conventional RadCom systems, where the number of independent channels is limited by the number of transmit and receive elements, the VTM leverages both combinatorial coupling and phase diversity among its distributed passive cells.

Each cell within the matrix receives an incident signal with a specific phase shift determined by the wave's AoA. These natural phase differences across the matrix are not digitally synthesized but rather directly exploited in the analog domain. The analog interference among these phase-shifted signals produces a variety of correlation patterns that encode both ampli-

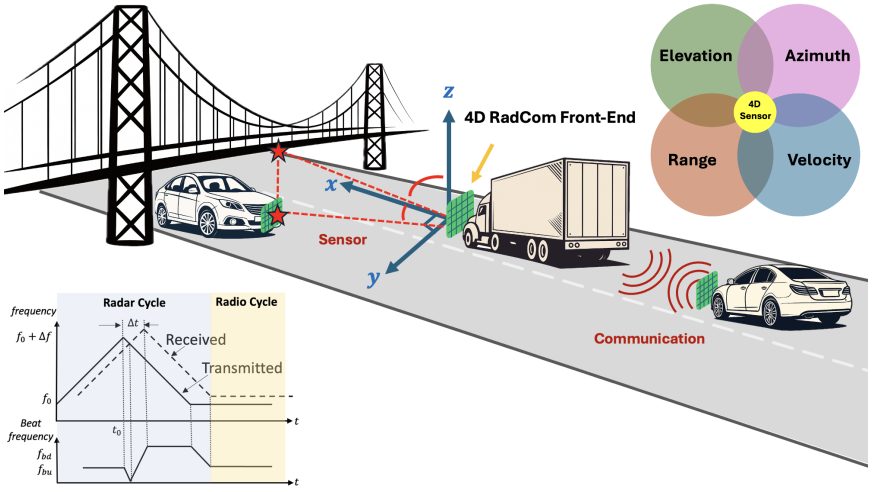

Figure 5.1 Conceptual representation of the 4D automotive RadCom sensor, showcasing its ability to measure range, velocity, azimuth, and elevation angles. The integration of radar and communication functions is achieved through the coordinated radar and radio cycles of the transmitted signal.

tude and phase information. By dynamically pairing or grouping cells, the proposed RadCom system effectively generates a vast set of virtual transceiver paths, each corresponding to a unique combination of incident phases and coupling configurations.

This phase-driven analog diversity expands the number of independent correlation channels far beyond what is achievable with conventional antenna arrays, creating a high-dimensional signal space without adding active circuitry or digital processing complexity. Consequently, the system can simultaneously detect and separate multiple targets, mitigate interference, and sustain concurrent communication links across spatially distinct nodes. The resulting scalability in both sensing and communication domains allows the proposed radar sensor to achieve superior multi-target resolution and data throughput using a compact, passive, and low-power front-end—marking a fundamental shift in how multifunctional RF architectures scale with system size.

Rooted in classical multi-port and interferometric architectures—including six-port receivers, hybrid coupler networks, and N-port reflectometers—the proposed virtualized and reconfigurable radar elevates these principles into a matrix-based front-end that performs joint analog-domain sensing and digital-domain communication [6, 8, 10, 16, 17, 19, 23, 43, 64, 65, 77, 87, 91, 93, 96, 101, 106, 115, 169, 170, 185–188]. By unifying these functions within a common hardware layer, the system eliminates redundant RF chains and mixers, significantly reducing cost, footprint, and power consumption while maintaining high spatial resolution and

communication fidelity, making it particularly well suited for next-generation automotive and wireless platforms.

The results confirm the potential of the proposed RadCom system as a low-complexity, reconfigurable solution for future ISAC systems in automotive and wireless networks. The remainder of the paper is structured as follows. Section 5.2 describes the system architecture and mathematical framework underpinning the 4D RadCom system. Section 5.3 presents the system architecture and design methodologies. Section 5.4 presents the experimental setup and measured results across all sensing and communication modes. Section 5.5 concludes the paper.

5.2 Multi-Target Detection Theory and Mathematical Modeling of Spatially Distributed Virtualized RadCom Cells

As illustrated in Fig. 5.2, the proposed 4D RadCom sensor is constructed from passive building blocks that convert incident RF fields into measurable baseband voltages. Two cell types define the architecture. The hybrid cell employs a 90° hybrid coupler connected to two square-law detectors, thereby extracting quadrature correlations between the received RF signal and a known reference. The power combiner cell implements a simple power summation, followed by a single detector, providing an in-phase correlation output with improved signal-to-noise ratio. By arranging these cells in an array, the system achieves high-dimensional projections of the incident wavefront that are suitable for demodulation, AoA estimation, and joint range–velocity detection.

A. Unit-Cell Level Representation

Let the complex baseband received signal at the p^{th} RadCom cell be denoted by $r_p(t)$, and the distributed reference signal by $s_p(t)$. In a hybrid cell, the hybrid coupler produces two orthogonal combinations,

$$\begin{aligned} u_{p,1}(t) &= \frac{1}{\sqrt{2}}\Big(r_p(t) + j s_p(t)\Big), \\ u_{p,2}(t) &= \frac{1}{\sqrt{2}}\Big(r_p(t) - j s_p(t)\Big). \end{aligned} \tag{5.1}$$

Square-law detectors with responsivities $\kappa_{p,1}$ and $\kappa_{p,2}$ yield output voltages

$$v_{p,1}(t) = \kappa_{p,1}|u_{p,1}(t)|^2, \quad v_{p,2}(t) = \kappa_{p,2}|u_{p,2}(t)|^2. \tag{5.2}$$

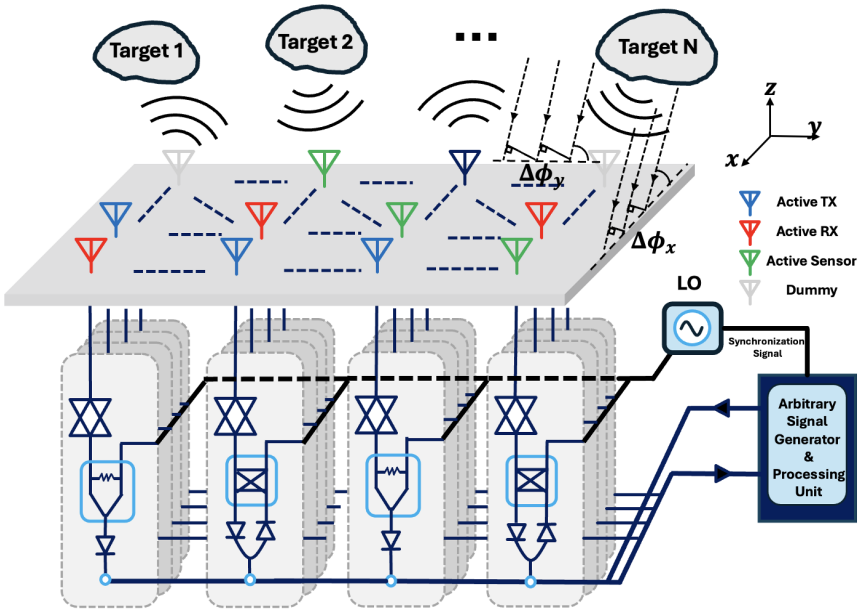

Figure 5.2 Schematic diagram of 4D RadCom cells at a given time snapshot, where different cells are configured as active TX, RX, sensors, or inactive (dummy). The front-end consists of a hybrid coupler, power divider/combiner, differential power detectors, an antenna, an amplifier, all integrated with a processing unit.

The differential operation of the two detectors provides

$$y_p^{(H)}(t) = v_{p,1}(t) - v_{p,2}(t) \approx 2\kappa_p^{(H)}\, \Im\{r_p(t)s_p^*(t)\}, \tag{5.3}$$

which represents the quadrature component of the correlation between the received signal and the reference.

For the power combiner cell, the RF signals are added as

$$u_q^{(C)}(t) = r_q(t) + s_q(t), \tag{5.4}$$

and the detected voltage is

$$y_q^{(C)}(t) = \kappa_q^{(C)}\, |u_q^{(C)}(t)|^2 \approx 2\kappa_q^{(C)}\, \Re\{r_q(t)s_q^*(t)\}. \tag{5.5}$$

Hence, the hybrid cell produces an imaginary correlation measurement, while the combiner cell provides the real correlation measurement. Together, they realize the full I/Q projection of the received signal onto the known reference.

B. VTM Transformation Matrix

Let $P = MN$ be the number of antenna positions in an $M \times N$ matrix of virtualized and reconfigurable RadCom cells. The received signals are collected in the vector

$$\mathbf{r}(t) = [\, r_1(t),\, r_2(t),\, \ldots,\, r_P(t)\,]^{\mathrm{T}}. \tag{5.6}$$

The reference signals are represented by the diagonal operator

$$\mathbf{T} = \mathrm{diag}\Big(s_1^*(t),\, s_2^*(t),\, \ldots,\, s_P^*(t)\Big). \tag{5.7}$$

The elementwise correlation between received and reference signals is then

$$\mathbf{z}(t) = \mathbf{T}\mathbf{r}(t). \tag{5.8}$$

Hybrid outputs correspond to imaginary projections of $\mathbf{z}(t)$, while combiner outputs correspond to real projections. Let $\mathbf{S}_H$ and $\mathbf{S}_C$ be selection matrices that indicate which antenna positions are connected to hybrids and combiners, respectively. With calibration matrices $\mathbf{C}_H$ and $\mathbf{C}_C$, the stacked measurement vector is expressed as

$$\mathbf{y}(t) = \begin{bmatrix} \mathbf{C}_H\, \Im\{\mathbf{S}_H \mathbf{z}(t)\} \\ \mathbf{C}_C\, \Re\{\mathbf{S}_C \mathbf{z}(t)\} \end{bmatrix} + \mathbf{w}(t), \tag{5.9}$$

where $\mathbf{w}(t)$ represents detector noise. This relation defines the real-valued linear transformation

$$\mathbf{y}(t) = \mathbf{H}\, \tilde{\mathbf{r}}(t) + \mathbf{w}(t), \tag{5.10}$$

with

$$\tilde{\mathbf{r}}(t) = \begin{bmatrix} \Re\{\mathbf{r}(t)\} \\ \Im\{\mathbf{r}(t)\} \end{bmatrix}, \tag{5.11}$$

and transformation matrix

$$\mathbf{H} = \begin{bmatrix} \mathbf{C}_H\, \mathbf{S}_H \Im\{\mathbf{T}\} & \mathbf{C}_H \mathbf{S}_H \Re\{\mathbf{T}\} \\ \mathbf{C}_C\, \mathbf{S}_C \Re\{\mathbf{T}\} & -\mathbf{C}_C \mathbf{S}_C \Im\{\mathbf{T}\} \end{bmatrix}. \tag{5.12}$$

The matrix $\mathbf{H}$ encapsulates the topology of hybrid and combiner cells, the distribution of the reference, and the calibration of detector gains. This operator maps the incident array field to the measurable low-frequency voltages that form the basis for sensing and communication

processing.

C. Two-Dimensional Angle-of-Arrival (AoA) Detection

The transformation matrix described above provides a mapping between the incident field at each 4D RadCom cell and the measurable baseband voltages. To evaluate its capability for spatial sensing, consider the case of a plane wave impinging on the matrix from elevation angle θ and azimuth angle ϕ. The complex field received at the (m, n)-th antenna element in one RadCom cell is

$$a_{m,n}(\theta, \phi) = \exp\left[-j\frac{2\pi}{\lambda}\left(md_x \cos\theta \cos\phi + nd_y \sin\phi\right)\right], \tag{5.13}$$

where $m \in \{0, \ldots, M-1\}$ and $n \in \{0, \ldots, N-1\}$. The collection of all MN responses forms the two-dimensional steering vector $\mathbf{a}(\theta, \phi) \in \mathbb{C}^P$, with $P = MN$. This vector fully describes how a plane wave from direction (θ, ϕ) is mapped across the matrix aperture.

For K simultaneous sources or targets, each with complex baseband envelope $b_k(t)$, the received field is given by

$$\mathbf{r}(t) = \sum_{k=1}^{K} b_k(t)\, \mathbf{a}(\theta_k, \phi_k). \tag{5.14}$$

Application of the transformation matrix yields

$$\mathbf{y}(t) = \sum_{k=1}^{K} \mathbf{B}(\theta_k, \phi_k)\, \tilde{b}_k(t) + \mathbf{w}(t), \tag{5.15}$$

where

$$\mathbf{B}(\theta, \phi) = \mathbf{H}\, \tilde{\mathbf{a}}(\theta, \phi), \qquad \tilde{\mathbf{a}}(\theta, \phi) = \begin{bmatrix} \Re\{\mathbf{a}(\theta, \phi)\} \\ \Im\{\mathbf{a}(\theta, \phi)\} \end{bmatrix}. \tag{5.16}$$

The matrix $\mathbf{B}(\theta, \phi) \in \mathbb{R}^{L \times 2}$ represents the effective steering response, where $L = N_H + N_C$ is the total number of 4D RadCom sensor measurement outputs. It accounts simultaneously for the physical matrix manifold, the hybrid and combiner topology, and the calibration constants. Importantly, while a conventional array manifold $\mathbf{a}(\theta, \phi)$ is complex-valued, the steering response is real-valued because the I/Q decomposition has been embedded into the transformation matrix $\mathbf{H}$. This property allows standard matrix processing techniques to be applied directly to the measured voltages.

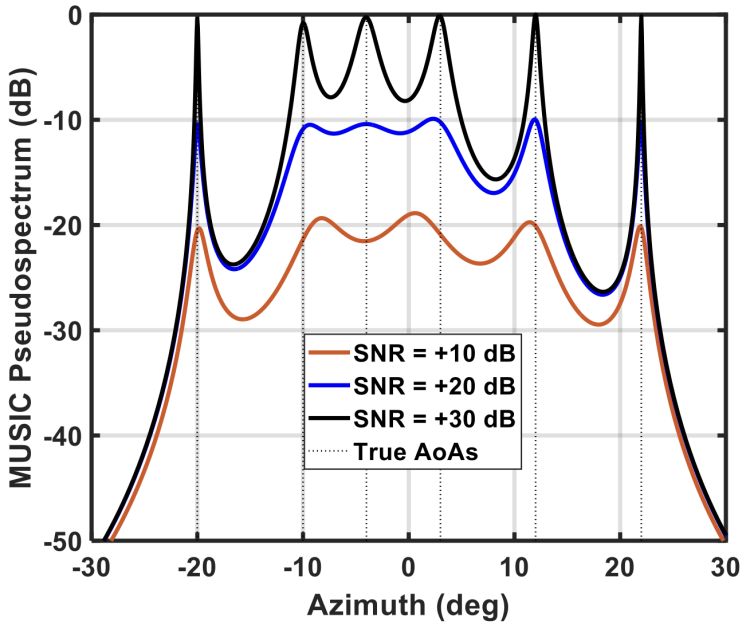

Figure 5.3 Normalized Multiple Signal Classification (MUSIC) pseudospectrum for six-target AoA estimation using the proposed RadCom sensor (8×8 matrix) across different SNRs (10 dB, 20 dB, 30 dB). The black dotted lines indicate the true AoAs, while the colored curves show the estimated pseudospectra, demonstrating improved resolution and peak sharpness with increasing SNR.

To extract DoA information, the sample covariance matrix of the outputs is formed as

$$\mathbf{R}_y = \frac{1}{T}\sum_{t=1}^{T}\mathbf{y}(t)\mathbf{y}^{\mathrm{T}}(t), \tag{5.17}$$

where T denotes the number of temporal snapshots. In the single-target case, $\mathbf{R}_y$ is approximately rank-one and proportional to $\mathbf{B}(\theta,\phi)\mathbf{B}^{\mathrm{T}}(\theta,\phi)$. For multiple targets, the covariance matrix becomes a weighted sum of such rank-one contributions. Subspace-based algorithms such as Multiple Signal Classification (MUSIC) exploit the orthogonality between the signal and noise subspaces of $\mathbf{R}_y$. By evaluating the projection of candidate steering responses $\mathbf{B}(\theta,\phi)$ onto the noise subspace, spatial spectra can be constructed, with peaks revealing the target directions (θ_k,ϕ_k). Alternative approaches such as Estimation of Properties by Iterative Techniques (ESPRIT) can also be applied by exploiting the shift-invariance properties of $\mathbf{B}(\theta,\phi)$ when the array geometry is regular.

Fig. 5.3 illustrates the MUSIC pseudospectrum for six target AoA estimation with an 8×8 matrix. Results are shown for signal-to-noise ratios (SNRs) of 10 dB, 20 dB, and 30 dB. The true AoAs are indicated by the solid black lines, while the colored curves represent the

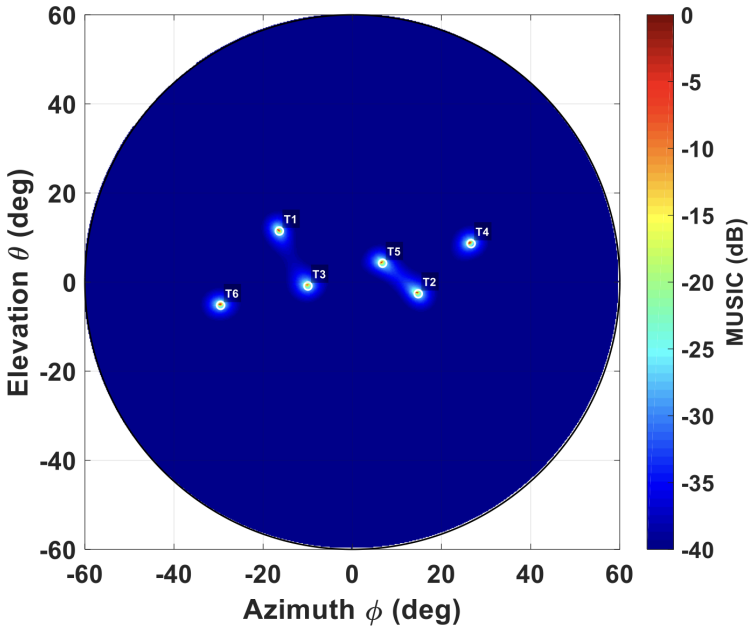

Figure 5.4 2D MUSIC circular AoA spectrum for six targets with Nx=8, Ny=8, and SNR = 25 dB. Distinct peaks corresponding to targets T1–T6 are visible in the azimuth–elevation plane, demonstrating the capability of the proposed method to resolve multiple sources under low-SNR conditions.

estimated pseudospectra. At low SNR (10 dB), the spectrum exhibits broadened peaks and increased sidelobe levels, leading to degraded resolution and occasional peak smearing around closely spaced sources. As the SNR increases to 20 dB, the peaks become more distinct and the sidelobes are significantly suppressed, allowing for more reliable AoA estimation. At high SNR (30 dB), the MUSIC algorithm achieves near-ideal performance, with sharp, well-localized peaks that closely align with the true AoAs. These results highlight the robustness of the proposed 4D virtualized and reconfigurable RadCom approach, demonstrating accurate AoA recovery even under moderate noise conditions.

The two-dimensional formulation is particularly significant because it allows simultaneous estimation of both azimuth and elevation. This is enabled by the spatial distribution of RadCom sensor cells in 2D, in which the phase progression along the x-axis depends on $\cos\theta\cos\phi$, while that along the y-axis depends on $\sin\phi$. As a result, angular resolution in both dimensions is achieved without requiring multiple stacked arrays or mechanical scanning. Furthermore, the hybrid and combiner cells ensure that both real and imaginary components of the array manifold are observable, making the effective steering matrix $\mathbf{B}(\theta, \phi)$ complete for 2D angle detection.

Fig. 5.4 presents the 2D MUSIC circular AoA spectrum obtained with $N_x = 8$, $N_y = 8$, and

SNR = 25 dB for a six-target scenario. The pseudospectrum reveals well-localized peaks at the true target positions (T1–T6) across the azimuth–elevation plane, indicating that the algorithm is capable of reliably separating multiple closely spaced sources despite the relatively low SNR. Compared to the 1D AoA spectrum, the 2D representation provides richer spatial information, allowing joint estimation of both azimuth and elevation with reduced ambiguity. The clear isolation of targets demonstrates the effectiveness of the proposed approach in preserving angular resolution and robustness under noise-limited conditions, which is essential for practical multi-target sensing applications.

The integration of the proposed RadCom operator into AoA processing therefore provides a compact and hardware-efficient means of realizing two-dimensional direction finding. Unlike conventional radar front-ends that require complex RF chains and mixers, the proposed RadCom sensor achieves the same outcome through passive couplers, combiners, and square-law detectors, with the algebraic transformation embedded in $\mathbf{H}$. This establishes a direct link between the cell-level architecture and the spatial sensing capability required for radar and communication applications.

D. Range and Velocity Estimation

The formulation developed in above subsection characterizes the angular response of the proposed 4D RadCom sensor. To extend this framework toward range and velocity detection operations, it is necessary to incorporate temporal modulation of the transmitted reference, which enables extraction of both parameters.

Consider an FMCW signal with sweep slope μ and carrier frequency f_c. The transmitted baseband waveform is expressed as

$$s(t) = e^{j(2\pi f_c t + \pi \mu t^2)}. \tag{5.18}$$

A target located at range R_k and moving with radial velocity v_k introduces a twofold distortion: a round-trip propagation delay $\tau_k = \frac{2R_k}{c}$ and a Doppler frequency shift $f_{D,k} = \frac{2v_k}{\lambda}$. The echo received at the (m, n)-th antenna element in one 4D RadCom cell is therefore

$$\begin{aligned} r^k_{m,n}(t) = \alpha_k \, s(t - \tau_k) \, e^{j2\pi f_{D,k} t} \\ \times \exp\Big[-j\frac{2\pi}{\lambda}\big(m d_x \cos\theta_k \cos\phi_k + n d_y \sin\phi_k\big)\Big]. \end{aligned} \tag{5.19}$$

where α_k denotes the complex reflection coefficient of the k-th target. Summing over all K

targets and stacking across the array yields the received signal vector

$$\mathbf{r}(t) = \sum_{k=1}^{K} \alpha_k \, s(t - \tau_k) e^{j2\pi f_{D,k} t} \mathbf{a}(\theta_k, \phi_k). \tag{5.20}$$

Application of the RadCom operator defined in subsection 5.2 C provides the measurable outputs

$$\mathbf{y}(t) = \sum_{k=1}^{K} \alpha_k \, \mathbf{B}(\theta_k, \phi_k) \, \tilde{s}(t - \tau_k, f_{D,k}) + \mathbf{w}(t), \tag{5.21}$$

where $\tilde{s}(t-\tau_k, f_{D,k})$ is the real–imag representation of the delayed and Doppler-shifted waveform, and $\mathbf{B}(\theta_k, \phi_k)$ is the effective steering response mapping each source into the L output channels.

To estimate range, the de-chirped signal is analyzed in fast time. The delay τ_k manifests as a beat frequency $f_{b,k} = \mu\tau_k = \frac{2\mu R_k}{c}$. By performing a Fourier transform across the fast-time samples, each target produces a distinct spectral peak at frequency $f_{b,k}$, directly yielding its range.

Velocity estimation is obtained from slow-time processing. Across multiple chirps transmitted at repetition period T_r, the Doppler shift contributes a phase progression proportional to $e^{j2\pi f_{D,k} m T_r}$ for the m-th chirp. By forming a Fourier transform along the slow-time index, the Doppler frequency $f_{D,k}$ can be extracted, leading to the radial velocity estimate

$$v_k = \frac{\lambda f_{D,k}}{2}. \tag{5.22}$$

Combining fast-time and slow-time processing produces a two-dimensional range–Doppler map for each RadCom output channel. Because the steering matrices $\mathbf{B}(\theta, \phi)$ are known, these maps can be coherently combined across all channels to enhance sensitivity and separate closely spaced targets. Specifically, joint processing of range, velocity, and angle domains allows reconstruction of the 4D sensing information cube (R, v, θ, ϕ). The architecture thus provides not only spatial resolution in azimuth and elevation, but also temporal resolution in range and velocity, while retaining a hardware-efficient front-end.

Furthermore, since the hybrid and combiner outputs preserve I/Q information relative to the reference, the same measurements can be employed for communication demodulation. This dual functionality underscores the advantage of the proposed 4D RadCom framework, in which the same set of low-frequency voltages enables both radar sensing and data recovery, unifying these traditionally separate operations.

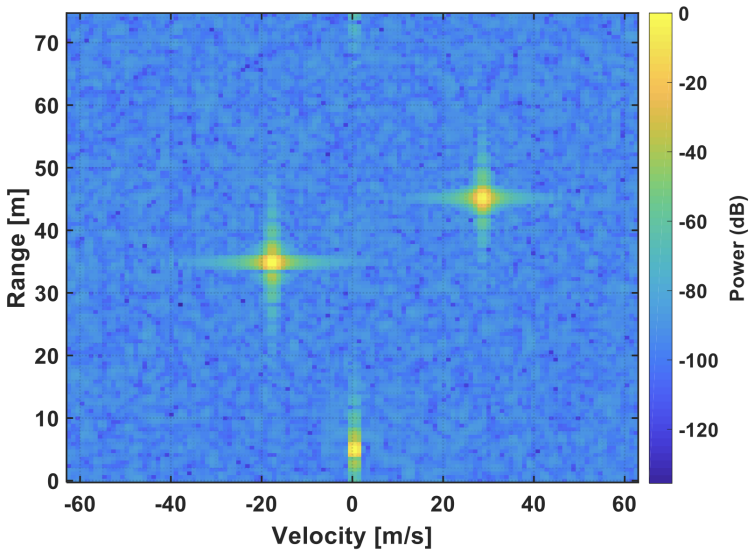

Figure 5.5 Range–velocity map showing target detections, where the color intensity represents the received power in dB. Distinct peaks indicate targets at different ranges and velocities, while clutter and sidelobes appear at lower power levels.

Fig. 5.5 shows the range–velocity map obtained from the proposed processing framework, where the color scale represents the received power in dB. Clear peaks can be observed at distinct range–velocity bins, corresponding to target detections. For example, one target appears around 40 m with a positive velocity, while another is located near 30 m with a negative velocity, demonstrating the capability to distinguish moving objects with different radial velocities. A strong stationary component near zero velocity corresponds to static clutter or reflections from the environment, which appear at lower ranges. The sharpness of the target peaks and the relative suppression of noise and sidelobes confirm the effectiveness of the approach in jointly resolving range and velocity, even in the presence of background interference.

E. System-Level Considerations

The mathematical framework developed in the preceding subsections establishes how the proposed RadCom sensor inherently performs angle, range, and velocity estimation through passive spatial transformations of the incident RF field. To physically realize these operations, it is implemented as a matrix of interferometric cells composed of multi-port passive networks and envelope-detecting power sensors. Each cell directly converts the incoming electromagnetic field into a low-frequency voltage that encodes the spatial phase distribution of the received wavefront.

Table 5.1 The 4D Automotive RadCom ADS/MATLAB Simulation Parameters

Param.	**Description**	**Value**
T_f	Chirp duration time	100 μs
f_c	Carrier frequency	24 GHz
BW	signal bandwidth	1.0 GHz
P_T	TX output power	12 dBm
G_{ANT}	TX/RX antenna gain	7.17 dBi
σ	Radar cross-section	10 m^2 (car), 1 m^2 (pedestrian)
R	Target range	1–90 m
V	Target velocity	0–30 m/s
G	cell gain	-3 to -6 dB
N	noise figure	7–10 dB
G_{RX}	RX array gain	40 dB
$C_{TX/RX}$	TX–RX coupling	-65 to -75 dB
Mod.	Comm. format	64-QAM, 50 MSym/s
Proc.	AoA/Range/Vel. est.	MUSIC + FFT

Since the outputs of the RadCom sensor are already at baseband, no mixers, local oscillators (LOs), or RF down-conversion chains are required, which substantially reduces system complexity and power consumption. The focus of the hardware design therefore shifts toward ensuring detector linearity, network phase balance, and controlled inter-cell coupling. In practice, each output is conditioned using low-noise amplification and anti-alias filtering before digitization. Because the resulting signals lie in the kilohertz-to-megahertz range, moderate-speed, high-resolution multi-channel ADCs can be used. In this regime, dynamic range and matching accuracy dominate the overall sensing fidelity, directly impacting covariance estimation and high-resolution AoA reconstruction.

System operation proceeds in two main stages. First, the RadCom sensor is calibrated to correct for detector gain/phase mismatches, offsets, and static network phase imbalances. These calibration parameters form the digital transformation matrix $\mathbf{H}$, applied to the raw digitized outputs for amplitude and phase equalization. Second, the conditioned voltages are processed through a low-frequency digital back-end that executes the full 4D radar and communication chain—range, Doppler, and 2D angular detection.

This hybrid analog–digital framework preserves the core advantage of the virtualized 4D RadCom sensor: the majority of sensing and communication functionalities are realized through passive analog transformations, whereas only lightweight digital processing is required at baseband. Eliminating active RF mixing and beamforming stages enables compact PCB or on-chip realizations in CMOS technologies and eases frequency-scaling constraints at mm-Wave and sub-THz bands.

Moreover, the matrix-based formulation provides a direct pathway for system evolution. Adaptive calibration corresponds to real-time updates of $\mathbf{H}$, machine-learning inference can

be incorporated to map voltage distributions to target states, and extensions toward reconfigurable intelligent surfaces (RISs) can be modeled by modifying the array manifold $\mathbf{B}(\theta, \phi)$. These capabilities highlight the scalability and energy efficiency of the proposed RadCom sensor as a versatile architecture for next-generation multifunction joint sensing and communication systems.

5.3 System Architecture and Design Methodology

The proposed joint 4D radar and communication system forms a unified platform—a scalable, reconfigurable front-end architecture supporting both active sensing and high-speed wireless communication. Unlike conventional radar transceivers that rely on fixed TX/RX chains and digital beamforming for target localization, the VTM paradigm employs a distributed matrix of compact transceiver cells. Each cell can dynamically switch between radar and communication functions as required by operational conditions.

The design aims to deliver accurate multi-target detection and high-throughput communication within a compact, low-power, and cost-effective structure optimized for automotive deployment. Fig. 5.2 shows the functional block topology of the proposed 4D RadCom system. A two-dimensional antenna matrix first captures the spatial characteristics of incoming electromagnetic waves. These signals are mixed with a LO during communication operation. For sensing purposes, a frequency-modulated continuous-wave (FMCW) signal generated by the source is used to detect multiple targets and vehicles concurrently. The resulting outputs, measured at power detectors, inherently carry the information needed for both sensing and communication.

The RadCom cells are designed based on two core building blocks: (1) a 90° hybrid coupler connected to a pair of power detectors, and (2) a power combiner linked to a single detector. Using these two configurations, the system performs joint sensing and communication without restrictions on the angle of incidence.

The overall architecture is organized into three layers: a cavity-backed L-shaped dipole RF antenna based on substrate-integrated waveguide (SIW) technology, a passive feed network for reference signal distribution, and an intermediate signal-conditioning stage ensuring precise synchronization and power detection. Finally, we present the detailed design principles of the 4D RadCom unit cell, implemented using multi-layer stacked SIW technology for compactness and scalability. The design methodology and performance of the multilayer magneto-electric dipole antenna, power divider/combiner, and hybrid coupler are presented in this subsection.

A. Multilayer Cavity-Backed Dipole Antenna

Fig. 5.6(a) shows the proposed multilayer dipole antenna implemented using SIW technology. Cylindrical vias are arranged around a central radiating element, forming a cavity for the dipole configuration. Critical geometrical parameters, including via radii, slot dimensions, and inter-element spacing, are optimized to achieve wideband impedance matching and high radiation efficiency, as summarized in Table. 5.2. The SIW cavity, defined by via fences, supports low-loss guided-wave propagation while maintaining a compact footprint and enabling seamless integration with other RF front-end components (see Fig. 5.6(b)).

A balanced feeding network ensures symmetric excitation of the dipole, providing stable far-field characteristics and improved polarization purity. The dipole antenna and cavity layer is fabricated on a Rogers RO4003 substrate with a thickness of 30 mils and a relative permittivity of 3.38. For the RX path, electromagnetic energy is coupled through a slot into two lower substrate layers of Rogers RO3010 with thickness of 10 mils and a relative permittivity of 10.2 to eventually routed to an LNA. Conversely, for the TX path, the electromagnetic field is coupled upward through the same slot from the output of a PA located beneath the antenna layer (see Fig. 5.6(c)).

The simulated reflection coefficient (S11) in Fig. 5.6(d) demonstrates a wide impedance bandwidth spanning 21–27 GHz, with multiple resonant dips corresponding to the excitation of hybrid modes. The 3D radiation pattern shown in Fig. 5.6(e) exhibits stable broadside gain, symmetric coverage, and low cross-polarization levels. The multilayer architecture thus achieves wide bandwidth, high gain, and compact integration, making it well-suited for 5G systems, automotive radar, and high-capacity mm-Wave communications. Furthermore, SIW technology is deliberately selected to minimize inter-cell coupling in large-scale VTM RadCom systems, improving scalability and overall system performance.

At the core of the analog front-end lies a matrix of power combiners, hybrid couplers, and power detectors that passively process incoming wavefronts. The design of Wilkinson Power Divider is presented in the next subsection.

B. Wilkinson Power Divider

Fig. 5.7(a) illustrates the proposed multilayer Wilkinson power divider designed on Rogers RO3010 substrate with a thickness of 10 mils and a relative permittivity of 10.2, along with transitions to another identical substrate containing the LNA, PA, and power detectors. The compact structure leverages cavities formed by periodic metallic vias and integrates an embedded resistor network to ensure isolation between output ports. Key structural param-

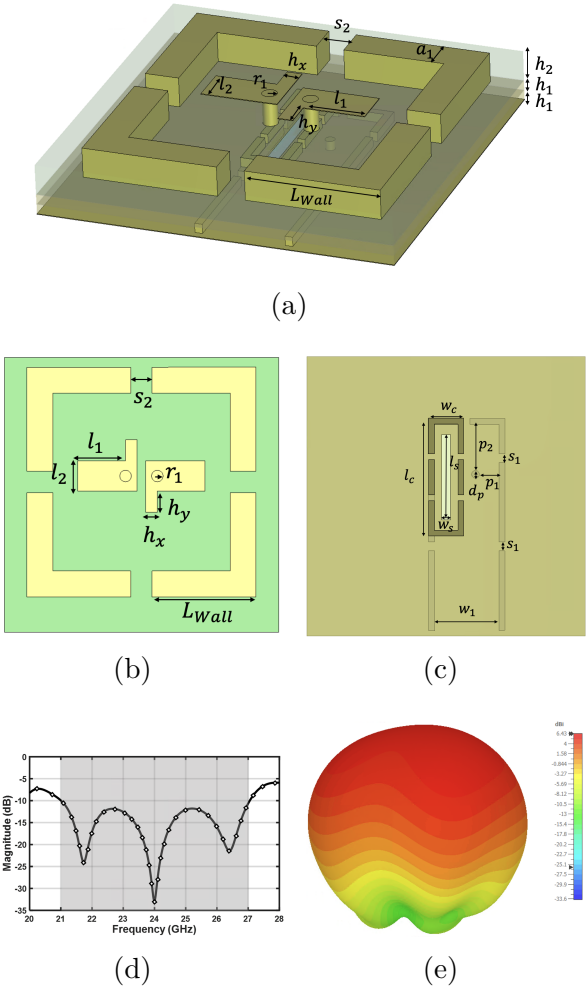

Figure 5.6 (a) Proposed cavity-backed L-shaped antenna. (b) Top view. (c) Coupling transition to the two underlying layers beneath the cavity layer. (d) Scattering parameters. (e) 3D radiation pattern.

eters—such as via radii, slot dimensions, and cavity widths—are optimized for wideband matching and minimal insertion loss, as summarized in Table. 5.3.

As shown in Fig. 5.7(b) and (c), S_{11}, S_{22}, and S_{33} remain below -10 dB from 22–26 GHz, while the insertion losses (S_{21}, S_{31}) are balanced and close to the theoretical -3 dB. Fig. 5.7(c) further demonstrates isolation (S_{23}) better than -20 dB within 23–27 GHz, confirming excellent port-to-port decoupling. The divider achieves wideband performance, low loss, and high isolation, enabling seamless integration into mm-Wave phased arrays and compact front-end modules.

Table 5.2 Dimension Parameters of Antenna

Parameter	**Value (mm)**	**Parameter**	**Value (mm)**
h_1	0.254	s_1	0.12
h_2	0.762	s_2	0.57
l_1	1.73	L_{wall}	4.02
l_2	1.25	a_1	0.90
h_x	0.80	w_s	0.30
h_y	0.82	l_s	2.90
w_c	1.05	L_c	3.80
p_1	0.67	p_2	1.57
d_p	0.26	r_1	0.20

C. 90° Hybrid Coupler

Fig. 5.8(a) presents the proposed multilayer 90° hybrid coupler. The coupler consists of four arms coupled through an optimized aperture with shorting pins to achieve equal power division and a quadrature phase difference. Periodic vias confine the electromagnetic fields within the SIW cavities, minimizing radiation losses while maintaining a compact footprint. The exact optimized dimensions are summarized in Table. 5.3.

The simulated S-parameters shown in Fig. 5.8(b) indicate that S_{11} remains below -15 dB over 22–27 GHz, while the through and coupled ports exhibit nearly equal insertion losses of approximately -3.2 dB. The isolation (S_{41}) exceeds -25 dB across the entire band. Furthermore, Fig. 5.8(c) confirms a stable 90° phase difference between the coupled ports, validating the quadrature hybrid operation. The proposed coupler thus offers wide bandwidth, low insertion loss, and excellent isolation, making it suitable for mmWave phased arrays, balanced transceivers, and beamforming networks.

D. Power Detection and Signal Conditioning

The hybrid coupler's two output paths and power combiner's only output path are connected to diode-based differential power detectors operating in the square-law region, converting RF power into measurable DC voltages. A differential topology is adopted to suppress common-mode noise and enhance demodulation linearity. This configuration also enables direct analog extraction of QAM baseband symbols without requiring high-speed analog-to-digital conversion, making the system highly efficient for low-power vehicular applications.

As shown in the layout of Fig. 5.7(a) and Fig. 5.8(a), the RF signal of either hybrid coupler or power combiner are routed through a microstrip line which is connected to the detection

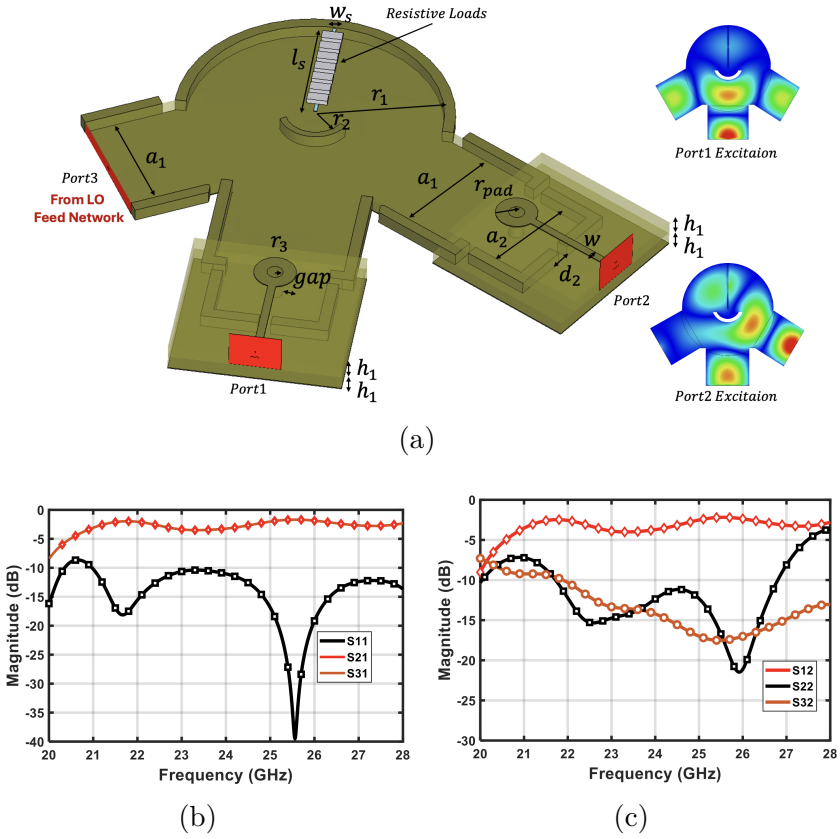

Figure 5.7 (a) 3D view of the Wilkinson power divider/combiner cell with resistive isolation and coupling apertures; field plots confirm the intended quadrature response. (b), (c) Simulated S-parameters under Port 1 and Port 2 excitation, demonstrating balanced power division, low reflection, and good port isolation around 24 GHz.

circuitry, where the diode-based detectors process the signal. Fig. 5.9(a) illustrates the input and output matching networks for the passive Schottky diode and its packaging models. The detected outputs are then combined and transferred through the interconnect network, ensuring minimal insertion loss and maintaining impedance matching across all transitions for optimal performance. Fig. 5.9(b) also shows the output voltage of power detector for different input power levels swept by various operational frequencies.

E. Signal Amplification

Each matrix cell integrates an amplifier in both the RX and TX paths. Fig. 5.10(a) demonstrates the input and output matching networks of the designed amplifier using a CE3520K3 FET transistor and its associated DC biasing connections. It is optimized for broadband operation within the 24 GHz band, providing sufficient gain for extended sensing ranges

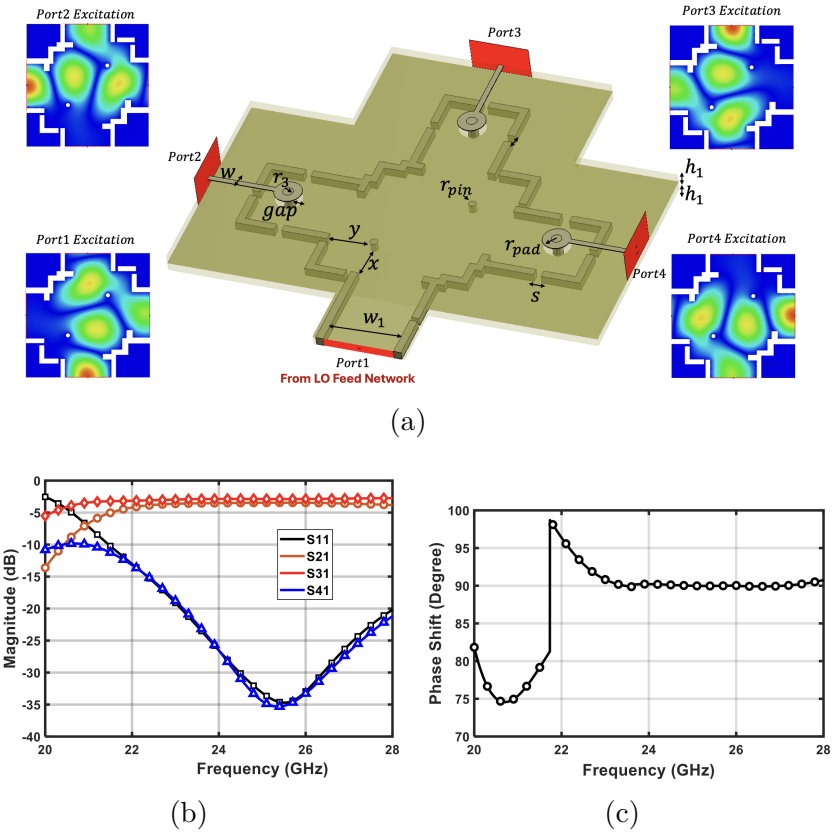

Figure 5.8 (a) 3D view of the 90° hybrid coupler cell, showing the coupling apertures, cavity geometry, and port arrangement, with field distributions for individual port excitations confirming the quadrature response. (b) Simulated S-parameters over the 24 GHz band. (c) Corresponding phase difference between the through and coupled ports.

while maintaining system-level noise figure and linearity requirements (see Fig. 5.10(b)). Fig. 5.10(c) illustrates the simulated stability performance of the amplifier, showing the Rollet stability factor K (red) and the B_1 parameter (blue) across frequency, both remaining above the unconditional-stability threshold throughout the 22–26 GHz band under multiple bias and temperature variations.

F. Signal Flow and Reconfigurability

The proposed 4D RadCom architecture achieves joint sensing and communication by leveraging a highly reconfigurable multi-layer front-end that flexibly adapts to different operational modes. By dynamically assigning the same hardware resources to either sensing or data communication, the system maximizes hardware efficiency while maintaining high performance in both domains. This integration significantly reduces the RF front-end footprint, lowers

Table 5.3 Dimension Parameters of Power Divider/Combiner and 90-Degree Hybrid Coupler

Parameter	**Value (mm)**	**Parameter**	**Value (mm)**
r_1	2.59	gap	0.25
r_2	0.10	w_s	0.06
r_3	0.20	l_s	2.40
a_1	2.48	r_{pin}	0.11
a_2	2.00	w_1	2.48
r_{pad}	0.40	w_2	0.15
x	1.39	y	1.42

power consumption, and enables seamless transitions between sensing and communication tasks, which are critical for advanced automotive and vehicular networking scenarios.

In sensing mode, a selected subset of matrix cells is activated to transmit FMCW signals, while the echoes reflected from surrounding targets are captured by a spatially distributed matrix of receiving cells. Within each cell, the combination of hybrid couplers and power detectors enables accurate interferometric AoA estimation by measuring the phase differences between signals arriving at spatially separated receivers. These phase relationships are further processed using a calibrated mathematical framework to precisely extract both elevation and azimuth angles, enabling high-resolution target localization.

In communication mode, the same matrix cells are seamlessly reconfigured to perform modulation and demodulation of high-order communication waveforms, such as 64-QAM symbols. Here, the hybrid coupler and power combiner cells operate as a quadrature splitter for direct down-conversion, while the differential detectors reconstruct the in-phase (I) and quadrature (Q) baseband components. By reusing the same RF chain for both radar sensing and high-speed data communication, the system achieves efficient time-duplexed RadCom functionality within a single compact hardware platform. This integrated architecture supports low-latency, high-reliability inter-vehicle data exchange, which is essential for collaborative perception and cooperative driving in future intelligent transportation systems.

Fig. 5.11 illustrates the proposed multilayer integrated 4D automotive RadCom front-end that enables this reconfigurable joint operation. The top antenna layer hosts an optimized array of radiating elements designed for simultaneous sensing and communication. Below it, the intermediate layer incorporates the LO feed network along with quadrature hybrids and power combiners, ensuring precise LO distribution and coherent signal combining across multiple channels. The bottom layer integrates the active RF circuitry, including LNAs, PAs, and power detectors, which provide signal amplification, conditioning, and detection. This

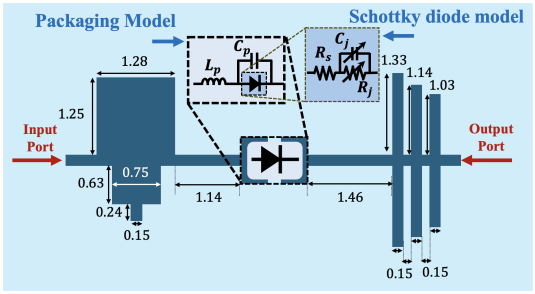

(a)

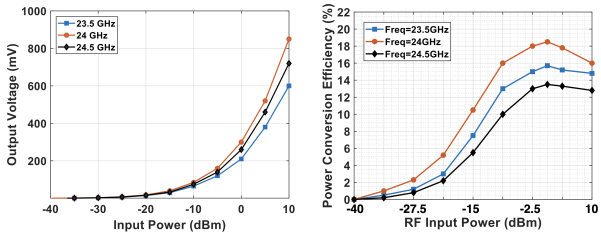

(b) (c)

Figure 5.9 (a) Geometric configuration of the designed microwave power detector. (b) Output voltage of the power detector with sweeping input power from –40 to 10 dBm. (c) Power conversion efficiency of the power detector for different operational frequencies versus RF input power.

compact multilayer integration minimizes interconnect losses, reduces hardware complexity, and enables efficient resource sharing between sensing and communication subsystems.

Finally, the overall reconfigurability of the proposed 4D RadCom sensor is governed by a processing control interface that dynamically manages the activation sequence of individual cells based on operational context, such as target detection conditions, communication bandwidth requirements, or power consumption constraints. By intelligently adapting the number and location of active elements, the system minimizes redundant signal paths and achieves highly energy-efficient operation while maintaining robust performance in both sensing and communication tasks.

5.4 Experimental Results and Performance Evaluation

This section presents the experimental validation of the proposed 4D RadCom sensor. A fully integrated prototype operating in the 24 GHz band was fabricated and tested to evaluate its performance in joint radar and communication tasks.

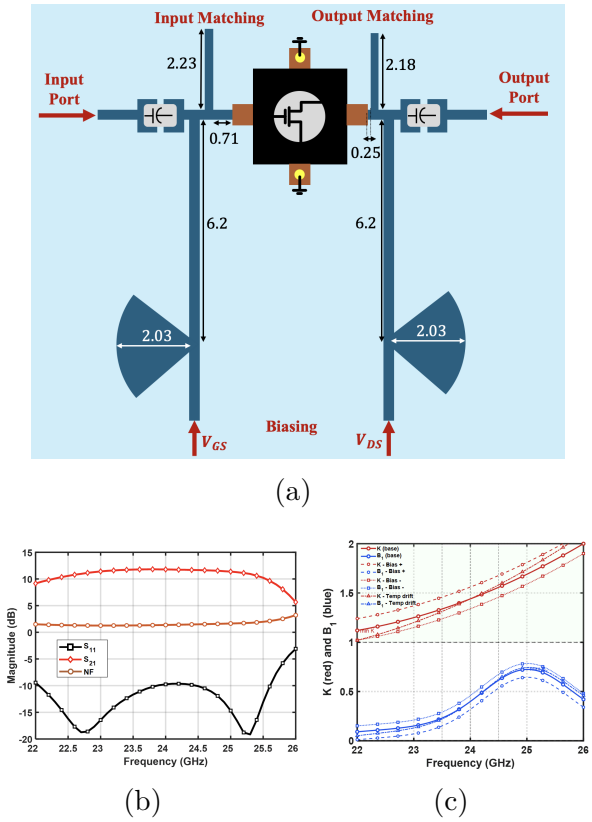

Figure 5.10 (a) Geometric configuration of the designed low-noise amplifier (LNA). (b) Scattering parameters and noise figure of the designed LNA ($V_{DS} = 2$ V, $V_{GS} = -0.45$ V). (c) Stability factors.

A. Prototype and Measurement Setup

To experimentally validate the proposed 4D RadCom sensor, a fully functional prototype was fabricated using a three-layer SIW architecture, (see Fig. 5.12). The sensor comprises an 8×8 matrix configuration, integrating hybrid couplers, power combiners, differential power detectors, and amplifiers. The cell size is approximately one wavelength at 24 GHz, resulting in an overall array dimension that remains compact and suitable for integration into automotive platforms such as bumpers or rooftop modules. The complete system is designed to support dual-mode operation, switching between radar and communication tasks.

The experimental setup includes a Keysight M8196A arbitrary waveform generator for generating linear FMCW chirps and an Agilent E8257D vector signal generator for modulated communication waveforms. A motorized two-dimensional rotary stage enables precise positioning of reflective targets to assess angular estimation performance. For communication testing, standard 64-QAM signals are transmitted between matrix cells, and their demodu-

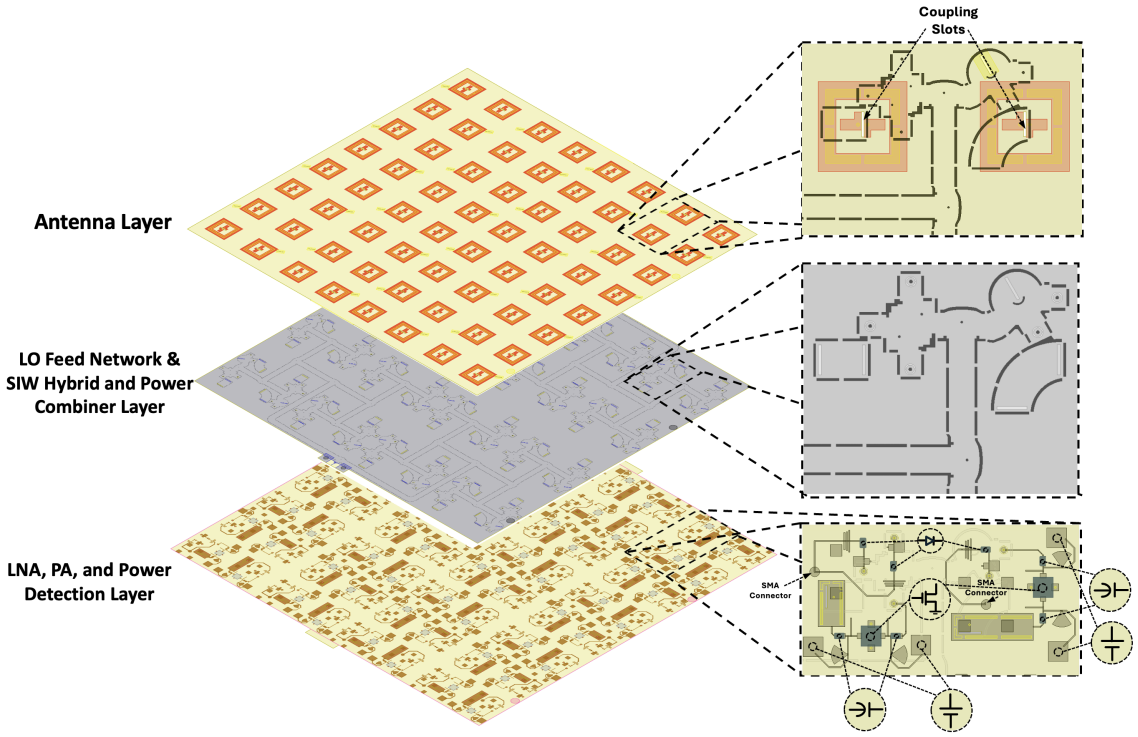

Figure 5.11 Exploded view of the proposed multilayer 4D automotive RadCom front-end. The top antenna layer hosts an array of radiating elements. The middle layer integrates the LO feed network, hybrid couplers, and power combiners for signal routing and coherent combining. The bottom layer includes LNAs, PAs, and power detectors for amplification and detection. Zoomed-in views on the right highlight key design details of each layer.

lation performance is evaluated through Error Vector Magnitude (EVM) and constellation reconstruction. For radar validation, a channel emulator (Keysight Propsim C8) is used to simulate controlled propagation environments, introducing programmable delays and Doppler shifts to emulate varying ranges and velocities of moving targets. Differential voltage outputs from each power detector are routed to a high-speed oscilloscope and a microcontroller-based digital back-end, which performs real-time analysis and calibration.

B. Communication Performance

The proposed 4D RadCom system's communication performance was experimentally validated by configuring one matrix cell as a transmitter and another as a receiver, while keeping the remaining array elements inactive. A 64-QAM signal centered at 24 GHz was generated and transmitted through the analog front-end composed of a hybrid coupler and differential power detectors. The in-phase and quadrature components were directly extracted from the analog outputs without any digital carrier recovery, and subsequently digitized by a low-noise

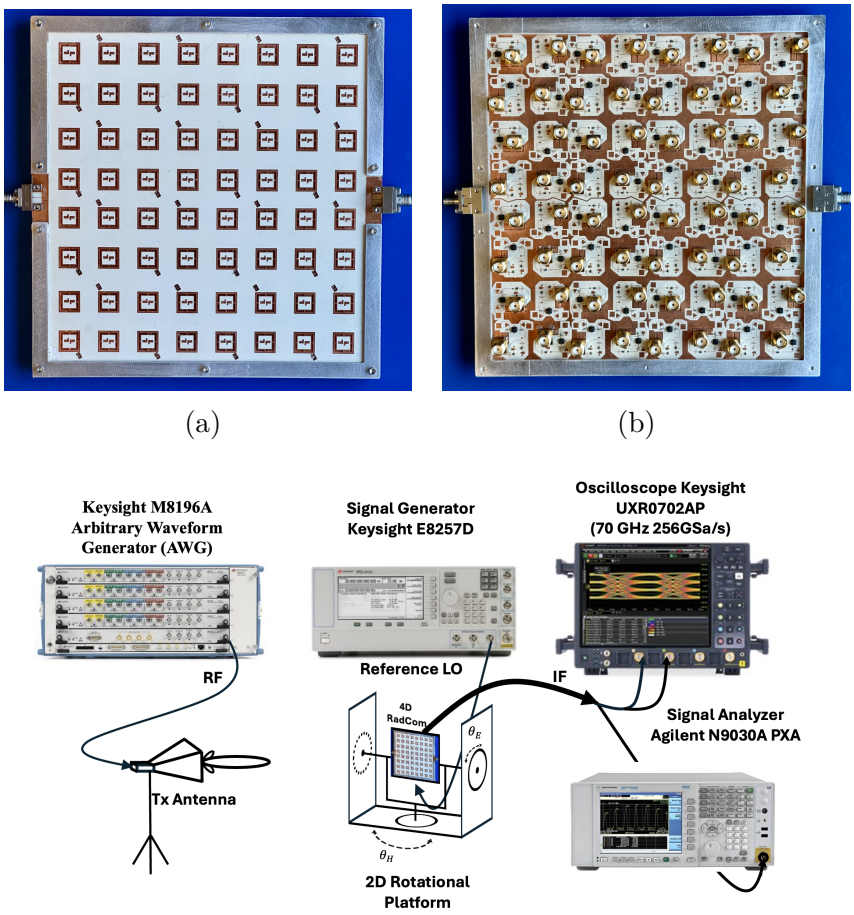

Figure 5.12 Fabricated prototype of 4D RadCom sensor (a) top view (b) bottom view. (c) Block diagram of the measurement setup for communication and 2D AoA detection.

sampling unit for constellation analysis.

As illustrated in Fig. 5.13, the measured 64-QAM constellations and corresponding spectra confirm the system's ability to faithfully transmit and demodulate high-order modulation signals. The RX mode exhibits an EVM of –29.7 dB, while the TX mode achieves an even lower EVM of –33.0 dB. These results verify the high linearity, low-distortion characteristics, and excellent I/Q balance. Moreover, the fully analog I/Q extraction approach eliminates the need for complex digital compensation, making the proposed architecture particularly suitable for compact, low-latency, and energy-efficient RadCom systems operating under stringent power constraints.

C. Angular Detection Results

The 2D AoA detection in the proposed RadCom sensor is achieved through a hybrid analog–digital interferometric process that efficiently combines passive phase measurement with high-resolution subspace estimation. Each matrix cell senses the incident wave's amplitude and phase through a hybrid coupler and differential power detector, generating analog I/Q voltages corresponding to the local phase state of the received signal. The relative phase differences between multiple spatially distributed matrix cells form an array manifold, which encodes the directional information of the incoming electromagnetic wave.

As shown in Fig. 5.14, the measured results confirm excellent agreement between the detected and true angles for both elevation (Fig. 5.14(a)) and azimuth (Fig. 5.14(b)) directions. The measured angles (blue markers) closely follow the ideal 1:1 line, while the error traces (red dashed lines) remain within $\pm 1.5^\circ$ over a $\pm 20^\circ$ scanning range. These results validate the high angular accuracy and robustness of the RadCom system, enabling precise 2D target localization without requiring active phase shifters or complex digital beamforming networks.

D. Range and Velocity Measurements

The range and velocity detection of the proposed RadCom sensor were experimentally validated using the FMCW configuration shown in Fig. 5.15(a). The measurement setup integrates a Keysight M8190A arbitrary waveform generator (AWG) for chirp synthesis, an Agilent E8267D microwave source for frequency up-conversion, and an Agilent N9030A PXA analyzer for down-converted signal observation. A PropSim C8 channel emulator was employed to reproduce controlled propagation conditions with adjustable target distances and Doppler shifts, while the matrix served as the analog sensing and mixing front-end. The transmitted and received chirps were routed through hybrid couplers and differential power detectors, enabling direct analog extraction of the beat signal that carries both range and velocity information.

As shown in Fig. 5.15(b), the measured beat-frequency spectrum demonstrates a clear peak structure with high signal-to-noise ratio, corresponding to the frequency difference between transmitted and reflected chirps. This beat component forms the basis for the fast-time FFT, which resolves the target's range by transforming the time-domain beat signal into the frequency domain. Subsequently, a slow-time FFT is applied across consecutive chirps to estimate the Doppler frequency shift, which yields the target's radial velocity. The resulting range–velocity pairs are then mapped to generate the full motion profile of the observed object.

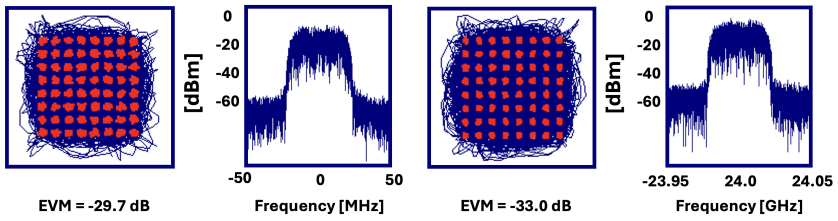

(a) (b)

Figure 5.13 Measured 64-QAM constellations and corresponding output spectra of the proposed RadCom system: (a) RX mode. (b) TX mode.

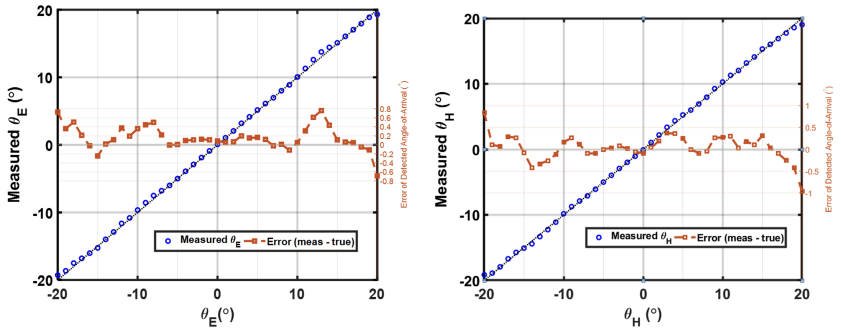

(a) (b)

Figure 5.14 Measurement results of 2D AoA detection for (a) elevation and (b) azimuth angles.

The quantitative results, presented in Fig. 5.15(c) and Fig. 5.15(d), confirm the high precision and linearity of the system's FMCW processing chain. The measured ranges align closely with the defined target positions up to 90 m, with an average error below ±2 m, while the measured velocities remain within ±1.7 m/s of the defined values up to 50 m/s. These findings verify that the hybrid analog–digital RadCom architecture can accurately extract range and velocity information through compact analog front-end processing and lightweight FFT-based digital estimation, achieving high fidelity and low latency suitable for real-time automotive and wireless sensing applications.

E. Multi-Target Testing Scenario

To validate the spatial detection capability of the proposed 4D RadCom sensor, a multi-target measurement experiment was conducted inside an anechoic chamber, as shown in Fig. 5.16(a). Three metallic corner reflectors were positioned at different heights and distances near the chamber corner to emulate complex scattering conditions. The measured 3D

reconstruction results, illustrated in Fig. 5.16(b), show that all three targets were successfully identified with high spatial accuracy. The measured points (red) closely coincide with the actual target positions (blue), confirming precise estimation of range, azimuth, elevation, and relative target separation. These results demonstrate the sensor's capability to perform multi-target detection and localization in realistic environments, highlighting its potential for high-resolution automotive and wireless sensing applications.

F. Comparative Evaluation

A comparative evaluation was conducted against representative state-of-the-art 4D radar and joint RadCom systems reported in the literature (see Table 5.4). Although some existing systems achieve finer angular resolution by leveraging dense MIMO configurations or high-frequency operation in the 77–81 GHz band, these typically require hundreds of channels and high-power digital signal processing units. In contrast, the proposed 4D RadCom offers a highly compact and energy-efficient alternative by leveraging passive interferometric analog processing and a dynamically reconfigurable matrix of cells. Furthermore, its integrated communication capability alongside radar operation, demonstrated through high-fidelity 64-QAM demodulation, sets it apart from conventional radar systems that lack data transmission functionalities. Overall, the proposed architecture strikes a balance between hardware simplicity, sensing performance, and multifunctionality, making it an attractive candidate for intelligent vehicular sensing networks.

5.5 Conclusion

This paper has introduced and experimentally validated a multifunctional 4D radar and communication sensor based on a reconfigurable and virtualized architecture. By unifying interferometric radar sensing and analog quadrature demodulation within a compact matrix of transceiver cells, the proposed platform achieves simultaneous measurement of range, velocity, azimuth, and elevation, alongside high-fidelity QAM communication. Comprehensive experimental results confirm the system's ability to resolve angular information with sub-5-degree resolution, detect range and Doppler signatures of targets up to 90 m, and demodulate 64-QAM symbols with EVM below –28 dB. These outcomes validate the effectiveness of the proposed architecture in supporting both radar and data exchange functionalities within a single hardware framework. Furthermore, the system's reconfigurability enables dynamic activation of sensing and communication modes, offering a scalable and efficient approach for adaptive vehicular applications. This work lays the foundation for future ISAC systems, where the seamless interplay of radar perception and data connectivity will be essential to

the advancement of connected and autonomous vehicle technologies. Future efforts will focus on extending the system to higher frequency bands, enhancing modulation capabilities, and enabling full-duplex RadCom operation for more advanced and collaborative automotive sensing environments.

Table 5.4 Performance Summary of Other State-of-the-Art Radar Sensors

Radar Types	**TX/RX (Ch.)**	**Freq. (GHz)**	P_{out} **(dBm)**	**Ant. Type**	**Gain (dBi)**	**EIRP (dBm)**	**NF (dB)**	**Functions / Cost**
[187] T-MTT 2022 *	8/8	2.4	NA	Patch	7	NA	NA	Radar / Low
[188] T-MTT 2018 *	1	61	NA	AiP	12	NA	NA	Radar / Low
[106] T-MTT 2017 *	1/4	23.7	8	Patch	NA	NA	NA	Radar / Low
[189] T-MTT 2024 #	4/8	77	NA	Patch	NA	NA	NA	Radar / Medium
[190] T-MTT 2018 #	2/2	94	18	Horn	22.9	40.9	20	Radar / High
[191] JSSC 2020 #	2/3	77	13.4	PCB	11.2	NA	15.3	Radar / High
This work (VTM RadCom) †	8×8	24	12.1	AiP (SIW)	7.17	18	9	**Joint 4D Radar + Comm / Low**

Notes: * six-port architecture # MIMO architecture. † = VTM-mapped virtual measurement channels.

Abbreviations: AiP = Antenna-in-Package.

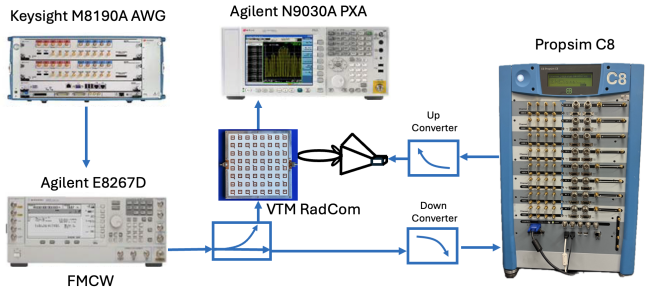

(a)

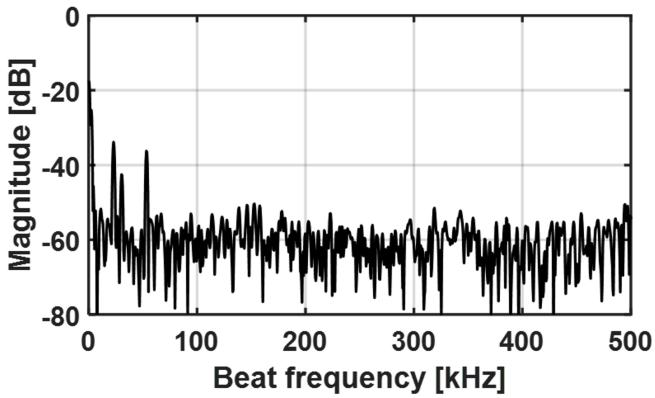

(b)

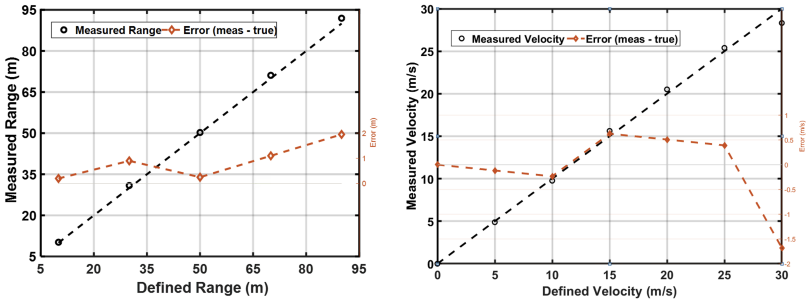

(c) (d)

Figure 5.15 (a) Measurement setup block diagram for range and velocity detection using Propsim C8 emulator. (b) Measured beat-frequency spectrum obtained from the FMCW waveform, showing clear frequency separation for range extraction. (c) Measured range. (d) Measured velocity.

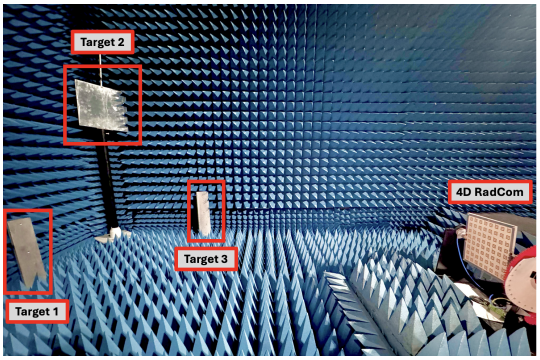

(a)

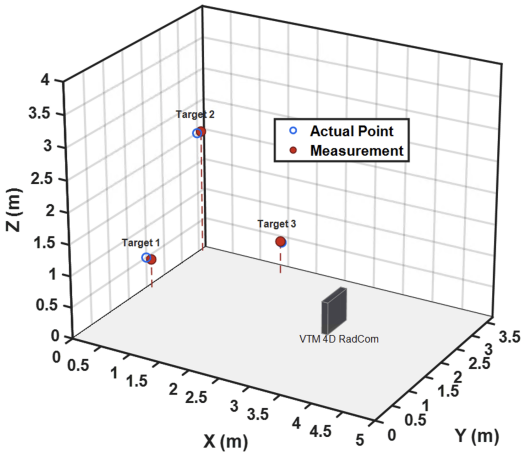

(b)

Figure 5.16 (a) The experimental setup of proposed 4D RadCom system inside the anechoic chamber with three metallic targets positioned at different heights and angles. (b) Reconstructed 3D target locations compared with their actual positions, demonstrating accurate spatial localization performance of the proposed architecture.

CHAPTER 6 VIRTUAL RECEIVER MATRIX FOR MULTIFUNCTION COMMUNICATION AND SENSING WIRELESS SYSTEMS USING SIMULTANEOUS INCIDENT WAVES AT THE SAME CARRIER FREQUENCY

In this paper, simultaneous reception and demodulation of incident signals at the same carrier frequency is proposed and demonstrated. Not only does this technique significantly enhance the communication capacity, but also, most importantly, it enables multifunction communication and sensing applications. This technique exploits both the phase difference and the angle-of-arrival (AoA) of incoming waves to demodulate multiple and simultaneous incident signals at the same carrier frequency. In addition, this is made possible through the combinatory and dynamic allocation of activated receiving units that are spatially distributed in the Virtual Receiver Matrix (VRM). The theoretical analysis is presented in this work, and as a proof of concept, a prototype is fabricated for 5G applications. Measurement results show an EVM of less than 10% for the two distinct 16-QAM signals.

6.1 Introduction

Over the last decades, the five generations of wireless technology have been introduced and deployed, each enabling features and services that provide breakthrough enhancements in terms of communication capacity and quality. Generally, they take advantage of networks with multiple base stations and access points [192]. However, future multifunction wireless communication and sensing systems, under the umbrella of 6G and beyond [193], should substantially upgrade their standards to keep pace with the insatiable demand for ever-increasing intelligence, capacity, and low latency driven by a projected rising number of smart terminals and data traffic [194]. In this connection, disruptive and innovative solutions are required to redefine the architectures of existing wireless systems [141].

Recently, a new receiver topology, named the *Virtual Receiver Matrix* (VRM), has been introduced [20], which accommodates multifunctionality in a smart, dense, and efficient manner, while tremendously increasing the number of potential receivers or receiving channels in a dynamic configuration compared to conventional fixed receivers.

In this paper, data reception and demodulation of two simultaneous incoming signals having the same carrier frequency are proposed and demonstrated using the VRM concept, thereby greatly enhancing communication capacity and multifunctionality. In fact, data reception for

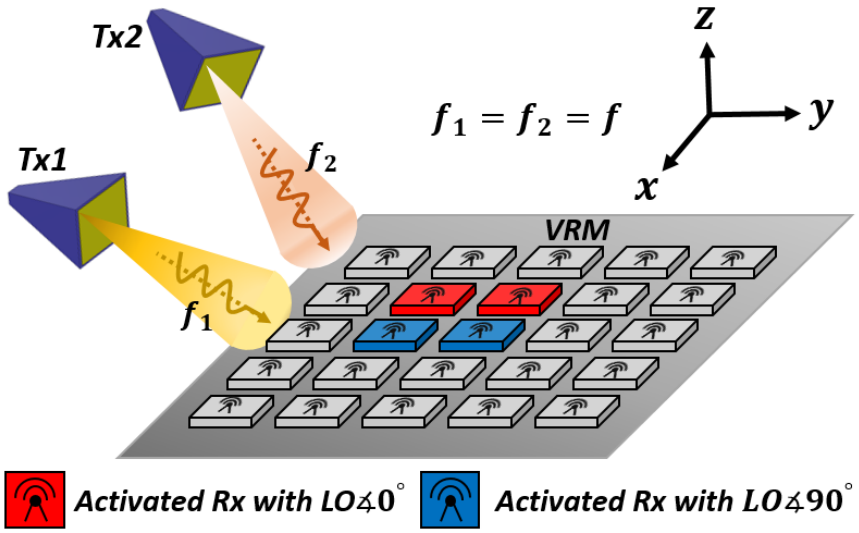

Figure 6.1 Conceptual illustration of VRM demodulating two incident signalsat the same carrier frequencies, simultaneously. Two red activated unitsextract quadrature components while the two blue ones demodulate in-phasecomponents of the two incident signals.

multiple incident signals is enabled by the VRM concept, consisting of a dynamic allocation of activated receiving units, spatially distributed in a two-dimensional (2D) matrix. By exploiting the phase difference of incident waves with diversified angles-of-arrival (AoAs), multiple and simultaneous incident signals at the same carrier frequency can be demodulated (See Fig. 6.1).

In the following, the theoretical background for demodulating two incident signals is studied and discussed. As a proof of concept, an experimental prototype is fabricated and measured at Ka-band for 5G multifunction applications, which is designed to receive two distinct sources with the same carrier frequency. In the fabricated prototype, each unit cell demodulates either the in-phase or quadrature component of an incoming QAM signal. The measurement results confirm the data reception and demodulation operation for both simultaneous incident signals.

6.2 Theoretical Analysis

The proposed VRM unit-cells illustrated in Fig. 6.2, involve a RF antenna, a low noise amplifier (LNA), a 90-degree hybrid coupler, and two power detectors connected in a differential and balanced form. Other forms of unit-cells are possible. The local oscillator (LO) signal is injected into each unit-cell through the other port of the hybrid coupler. To avoid the

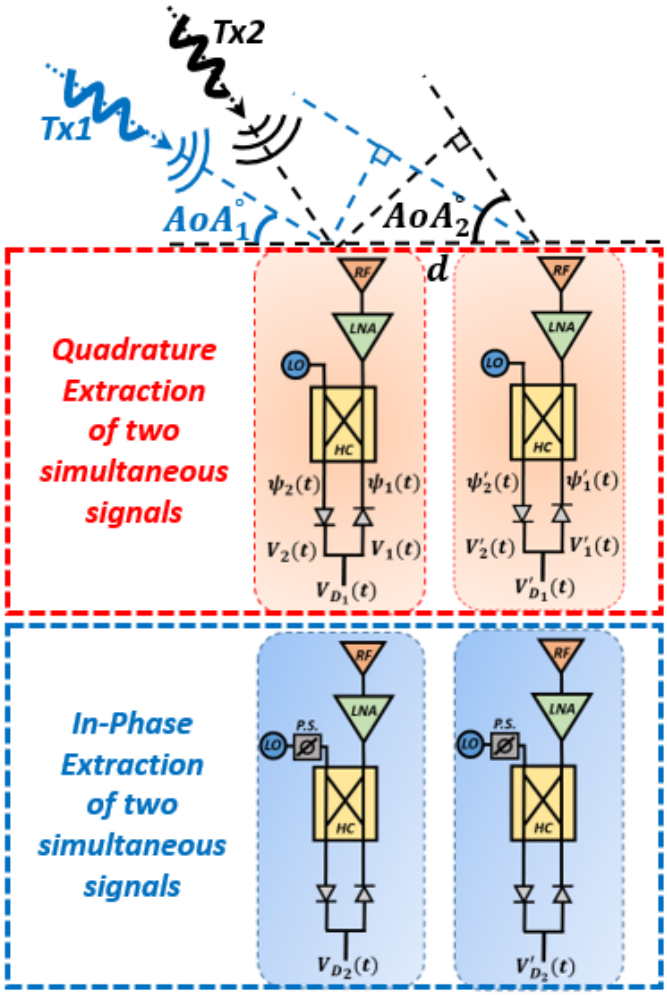

Figure 6.2 Block diagram of 2D VRM unit-cells, each containing an antenna,a LNA, a 90-degree hybrid coupler, and two power detectors connectedin a differential and balanced form. Two different signals at the samecarrier frequency are incident on the VRM unit-cells with different AoAs,simultaneously. (P.S. and HC are short for phase shifter and hybrid coupler,respectively).

leakage of LO into the antenna, these two ports should be designed with maximum possible isolation. In the following, the theoretical analysis of data reception for two different incoming signals having the same carrier frequency is presented. In the case of a coherent receiver, the frequency of carrier at both transmitter and receiver is considered the same for both transmitted signals. Considering the proposed configuration for each unit-cell of VRM in Fig. 6.2, the received signal after the LNA of the first unit-cell is

$$S_{\mathrm{RF}}(t) = a_{\mathrm{RF}}\alpha_1(t)e^{j(\omega t+\theta_1(t))} + a_{\mathrm{RF}}\alpha_2(t)e^{j(\omega t+\theta_2(t))} \tag{6.1}$$

where $\alpha_1(t)$, $\alpha_2(t)$ and $\theta_1(t)$, $\theta_2(t)$ are the modulated amplitude and phase of transmitted baseband signals, respectively. If we also consider the injected LO signal as

$$S_{\mathrm{LO}}(t) = a_{\mathrm{LO}} e^{j\omega t} \tag{6.2}$$

then, the output signals of the 90-degree hybrid coupler ports can be obtained as

$$\psi_1(t) = -\frac{a_{\mathrm{LO}}}{\sqrt{2}} e^{j\omega t} \left[j \frac{a_{\mathrm{RF}}}{a_{\mathrm{LO}}} \alpha_1(t) e^{j\theta_1(t)} + \frac{a_{\mathrm{RF}}}{a_{\mathrm{LO}}} \alpha_2(t) e^{j\theta_2(t)} + 1 \right] \tag{6.3}$$

$$\psi_2(t) = -\frac{a_{\mathrm{LO}}}{\sqrt{2}} e^{j\omega t} \left[\frac{a_{\mathrm{RF}}}{a_{\mathrm{LO}}} \alpha_1(t) e^{j\theta_1(t)} + \frac{a_{\mathrm{RF}}}{a_{\mathrm{LO}}} \alpha_2(t) e^{j\theta_2(t)} + j \right] \tag{6.4}$$

These two signals are connected to power detectors with opposite polarities, thus resulting in baseband signals proportional to their input RF power:

$$V_i(t) = K \left| \psi_i(t) \right|^2, \quad i = 1, 2 \tag{6.5}$$

where K is a constant determined by the type of power detectors. Accordingly, the output voltages of the power detectors are described as follows:

$$\begin{aligned} V_1(t) = \frac{K a_{\mathrm{LO}}^2}{2} \Bigg[& 1 + \left(\frac{a_{\mathrm{RF}}}{a_{\mathrm{LO}}} \right)^2 \alpha_1^2(t) + \left(\frac{a_{\mathrm{RF}}}{a_{\mathrm{LO}}} \right)^2 \alpha_2^2(t) \\ & - 2 \left(\frac{a_{\mathrm{RF}}}{a_{\mathrm{LO}}} \right) \alpha_1(t) \sin(\theta_1(t)) - 2 \left(\frac{a_{\mathrm{RF}}}{a_{\mathrm{LO}}} \right) \alpha_2(t) \sin(\theta_2(t)) \Bigg] \end{aligned} \tag{6.6}$$

$$\begin{aligned} V_2(t) = \frac{K a_{\mathrm{LO}}^2}{2} \Bigg[& 1 + \left(\frac{a_{\mathrm{RF}}}{a_{\mathrm{LO}}} \right)^2 \alpha_1^2(t) + \left(\frac{a_{\mathrm{RF}}}{a_{\mathrm{LO}}} \right)^2 \alpha_2^2(t) \\ & + 2 \left(\frac{a_{\mathrm{RF}}}{a_{\mathrm{LO}}} \right) \alpha_1(t) \sin(\theta_1(t)) + 2 \left(\frac{a_{\mathrm{RF}}}{a_{\mathrm{LO}}} \right) \alpha_2(t) \sin(\theta_2(t)) \Bigg] \end{aligned} \tag{6.7}$$

Since the power detectors are configured in a differential form, their differential output voltage becomes

$$V_{D1}(t) = 2Ka_{\mathrm{LO}}a_{\mathrm{RF}}\left[\alpha_1(t)\sin(\theta_1(t)) + \alpha_2(t)\sin(\theta_2(t))\right] \tag{6.8}$$

The phase differences between received signals at two distinct antennas in different cells can be formulated as follows:

$$\Delta\phi_1 = \frac{2\pi}{\lambda}d\cos(\mathrm{AoA}_1), \quad \Delta\phi_2 = \frac{2\pi}{\lambda}d\cos(\mathrm{AoA}_2) \tag{6.9}$$

where d is the inter-element distance between any two cells distributed in the matrix, λ is the operational wavelength, and AoA_1 and AoA_2 are the angles of arrival of the two incident waves. By considering these two phase differences, we can obtain the RF signal after the LNA of the second unit cell as

$$S'_{\mathrm{RF}}(t) = a_{\mathrm{RF}}\alpha_1(t)e^{j(\omega t+\theta_1(t))}e^{-j\Delta\phi_1} + a_{\mathrm{RF}}\alpha_2(t)e^{j(\omega t+\theta_2(t))}e^{-j\Delta\phi_2} \tag{6.10}$$

Again, after injecting LO power to the hybrid coupler of the second unit cell, the signals before the power detectors can be obtained as

$$\psi'_1(t) = -\frac{a_{\mathrm{LO}}}{\sqrt{2}}e^{j\omega t}\left[j\frac{a_{\mathrm{RF}}}{a_{\mathrm{LO}}}\alpha_1(t)e^{j(\theta_1(t)+\Delta\phi_1)} + j\frac{a_{\mathrm{RF}}}{a_{\mathrm{LO}}}\alpha_2(t)e^{j(\theta_2(t)+\Delta\phi_2)} + 1\right] \tag{6.11}$$

$$\psi'_2(t) = -\frac{a_{\mathrm{LO}}}{\sqrt{2}}e^{j\omega t}\left[\frac{a_{\mathrm{RF}}}{a_{\mathrm{LO}}}\alpha_1(t)e^{j(\theta_1(t)+\Delta\phi_1)} + \frac{a_{\mathrm{RF}}}{a_{\mathrm{LO}}}\alpha_2(t)e^{j(\theta_2(t)+\Delta\phi_2)} + j\right] \tag{6.12}$$

Therefore, the output voltages of power detectors can be calculated as

$$\begin{aligned} V'_1(t) = \frac{Ka_{\mathrm{LO}}^2}{2}\Bigg[1 &+ \left(\frac{a_{\mathrm{RF}}}{a_{\mathrm{LO}}}\right)^2\alpha_1^2(t) + \left(\frac{a_{\mathrm{RF}}}{a_{\mathrm{LO}}}\right)^2\alpha_2^2(t) \\ &- 2\left(\frac{a_{\mathrm{RF}}}{a_{\mathrm{LO}}}\right)\alpha_1(t)\sin\Big(\theta_1(t)+\Delta\phi_1\Big) - 2\left(\frac{a_{\mathrm{RF}}}{a_{\mathrm{LO}}}\right)\alpha_2(t)\sin\Big(\theta_2(t)+\Delta\phi_2\Big)\Bigg] \end{aligned} \tag{6.13}$$

$$V_2'(t) = \frac{Ka_{\mathrm{LO}}^2}{2}\Bigg[1 + \left(\frac{a_{\mathrm{RF}}}{a_{\mathrm{LO}}}\right)^2 \alpha_1^2(t) + \left(\frac{a_{\mathrm{RF}}}{a_{\mathrm{LO}}}\right)^2 \alpha_2^2(t) + 2\left(\frac{a_{\mathrm{RF}}}{a_{\mathrm{LO}}}\right)\alpha_1(t)\sin\Big(\theta_1(t) + \Delta\phi_1\Big) + 2\left(\frac{a_{\mathrm{RF}}}{a_{\mathrm{LO}}}\right)\alpha_2(t)\sin\Big(\theta_2(t) + \Delta\phi_2\Big)\Bigg] \tag{6.14}$$

The differential output of the second unit cell can then be written as

$$V_{D1}'(t) = 2Ka_{\mathrm{LO}}a_{\mathrm{RF}}\left[\alpha_1(t)\sin\Big(\theta_1(t) + \Delta\phi_1\Big) + \alpha_2(t)\sin\Big(\theta_2(t) + \Delta\phi_2\Big)\right] \tag{6.15}$$

By setting $\Delta\phi_1 = 2\pi n$ and $\Delta\phi_2 = 2\pi n + \pi$, we can readily find the quadrature components of the two signals as

$$Q_1(t) = V_{D1}(t) + V_{D1}'(t), \qquad Q_2(t) = V_{D1}(t) - V_{D1}'(t) \tag{6.16}$$

Until now, we have obtained the quadrature components of the two incident signals with the same carrier frequency. For the in-phase components, another set of two unit cells should be chosen, with the difference that their injected LO signals should have a 90-degree phase shift. Using a similar procedure from (6.1) to (6.16), we can establish the following formulas for their differential output voltages.

$$V_{D2}(t) = 2Ka_{\mathrm{LO}}a_{\mathrm{RF}}\left[\alpha_1(t)\cos\Big(\theta_1(t)\Big) + \alpha_2(t)\cos\Big(\theta_2(t)\Big)\right] \tag{6.17}$$

$$V_{D2}'(t) = 2Ka_{\mathrm{LO}}a_{\mathrm{RF}}\left[\alpha_1(t)\cos\Big(\theta_1(t) + \Delta\phi_1\Big) + \alpha_2(t)\cos\Big(\theta_2(t) + \Delta\phi_2\Big)\right] \tag{6.18}$$

Hence, by setting the same conditions for phase difference, we can readily find out the in-phase components of the two signals.

$$I_1(t) = V_{D2}(t) + V_{D2}'(t), \qquad I_2(t) = V_{D2}(t) - V_{D2}'(t) \tag{6.19}$$

Now, considering complex vectors of $S_1(t) = I_1(t) + jQ_1(t)$ and $S_2(t) = I_2(t) + jQ_2(t)$, the two demodulated signals can be extracted separately.

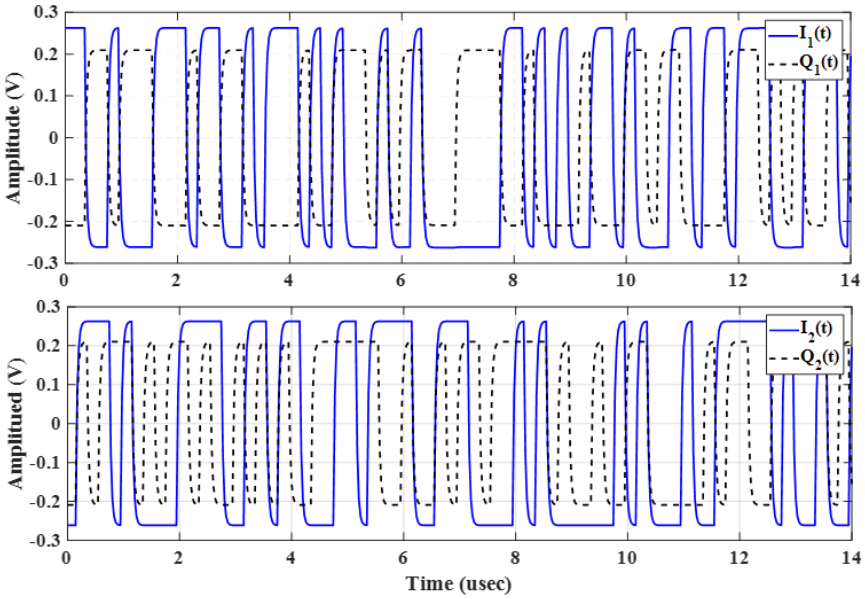

Figure 6.3 Simulated in-phase and quadrature components of two simultaneousincident signals at the same carrier frequency for QPSK modulation with datarate of 2 MSPs.

6.3 Design Methodology and Performance Analysis

For the proof of concept, a VRM prototype of 3×5 unit cells is designed and fabricated on Rogers RO4350 substrate over Ka-band for 5G applications. This prototype is intended to receive two signals with the same carrier frequency simultaneously, as shown in Fig. 6.3. The prototype is designed and analyzed in the Advanced Design System (ADS) software platform, and full-wave simulations are performed in CST software to design the antenna and hybrid couplers. The output voltages of power detectors (SMS7630-040LF) are connected to a Keysight UXR0702AP Real-Time Oscilloscope to demonstrate the constellations of demodulated signals. Using an Agilent PSG vector signal generator (E8267D), a bit train of 16-QAM modulation with a symbol rate of 2 Msps is generated. All generators and analyzers are synchronized to ensure receiver coherency. The VRM is placed on a rotational platform to adjust the desired AoAs with respect to the horn radiators. Considering the designed unit cells with an inter-element distance of two wavelengths, the AoAs are set to 65.2° and 83.7°. Fig. 6.4 shows the measured constellation diagrams of the VRM prototype for the two incident signals, validating the receiving operation. The receiver exhibits an EVM of less than 10% for both signals.

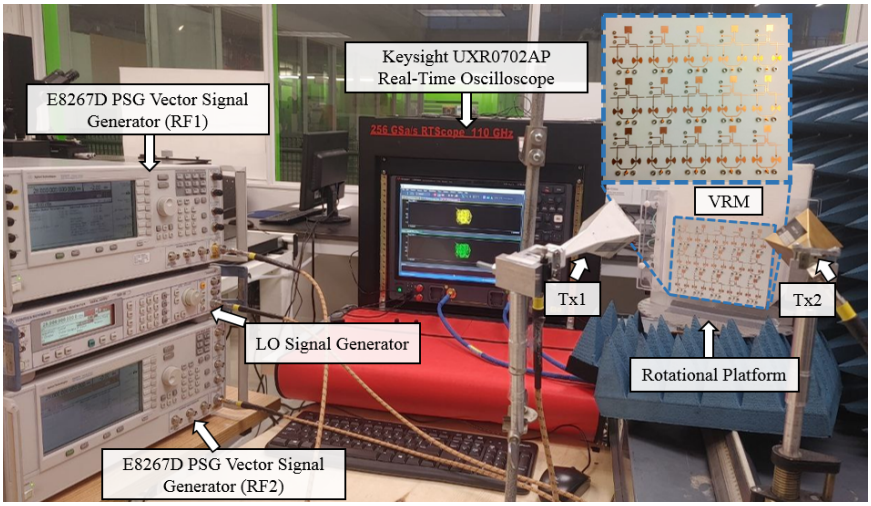

Figure 6.4 Photograph of the measurement setup for demodulating twosimultaneous incident signals with different AoAs over the VRM.

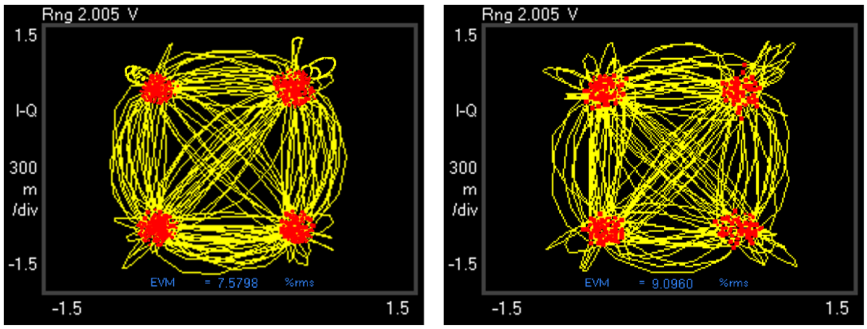

Figure 6.5 Measured constellations of two simultaneous incident signals withdifferent AoAs.

6.4 Conclusion

This work proposed and presented the demodulation of simultaneous incident signals featuring the same carrier frequency, for the first time. This seamless architecture technique, which is made possible through the concept of VRM, greatly enhances the capacity and multifunctionality of future wireless systems. A mathematical modeling of the proposed technique was derived and presented. As a proof-of-concept, a fabricated prototype was measured at Ka-band for 5G applications, and measurements results have confirmed the viability of the proposed technique.

CHAPTER 7 CONCLUSION

This chapter concludes the thesis by summarizing the principal contributions, critically discussing the limitations of the proposed architectures, and outlining well-defined directions for future research. The work presented in this thesis addressed the growing need for compact, energy-efficient, and multifunctional RF front-ends capable of jointly supporting sensing and communication functionalities within a unified hardware framework. By rethinking the role of multi-port interferometric architectures, this research demonstrated that advanced spatial processing and information extraction can be achieved without relying exclusively on fully digital beamforming or large-scale active arrays.

7.1 Summary of Works

This thesis introduced a novel class of reconfigurable RF front-end architectures based on the concepts of the VRM and the VTM. The proposed framework departs from conventional MIMO and phased-array paradigms by exploiting passive analog interference and fixed multi-port combining networks to synthesize virtual spatial channels directly in the RF domain.

The research began with a critical analysis of existing multi-port receivers and joint radar communication systems, highlighting their limitations in terms of scalability, hardware overhead, calibration complexity, and power consumption. These observations motivated the development of a new interferometric front-end that maps a dense grid of physical antenna elements into a reduced set of virtual channels with well-defined spatial responses.

A rigorous mathematical formulation was developed to describe floating-channel formation, spatial interference, and virtual beam synthesis within the VRM/VTM framework. This formulation established clear links between physical array geometry, analog combining coefficients, and the resulting virtual channel responses. Based on this theoretical foundation, signal processing strategies for angle-of-arrival estimation, multi-target detection, and data demodulation were derived and validated.

The proposed architectures were experimentally demonstrated through multiple hardware prototypes operating at millimeter-wave frequencies. Measurement results confirmed the ability of the VTM-based systems to perform high-resolution spatial sensing, simultaneous multi-user communication, and joint radar–communication operation using a compact and low-power front-end. Comparisons with state-of-the-art radar and ISAC platforms showed that the proposed approach achieves competitive performance while significantly reducing

RF chain count, calibration burden, and system complexity.

Overall, the results of this thesis establish the VRM/VTM paradigm as a viable and scalable alternative to conventional RF front-end architectures for future integrated sensing and communication systems.

7.2 Limitations

Despite the demonstrated capabilities of the proposed architectures, several limitations must be acknowledged. First, the performance of VRM/VTM systems is inherently sensitive to amplitude and phase mismatches within the analog multi-port network. While calibration and compensation techniques were proposed and experimentally validated, their complexity increases with the number of virtual channels and operating frequency, particularly in millimeter-wave and sub-THz regimes.

Second, the reliance on analog-domain processing introduces a trade-off between hardware efficiency and operational flexibility. Unlike fully digital systems, the virtual channel responses in the proposed architectures are determined by fixed or semi-reconfigurable analog weights, which may limit adaptability in highly dynamic environments or wideband multi-standard scenarios.

Additionally, the experimental validations presented in this thesis were primarily conducted under controlled laboratory conditions. Although these experiments provide strong proof of concept, further evaluation in realistic propagation environments—including mobility, interference, and non-ideal channel conditions—is required to fully characterize system robustness and long-term stability.

7.3 Future Research

The results of this thesis open several promising avenues for future investigation. Each direction represents a natural extension of the VTM paradigm toward next-generation RF systems.

A first major direction concerns the realization of ultra-massive VTM architectures integrated at sub-THz and THz frequencies. Advancements in on-chip and package-level integration could enable dense virtual transceiver matrices with unprecedented spatial resolution, supporting emerging applications such as high-data-rate wireless links, high-resolution imaging, and compact automotive or biomedical sensors.

A second direction involves the incorporation of artificial intelligence and machine learning

techniques for hardware-aware calibration, adaptive beam synthesis, and dynamic reconfiguration. By embedding learning-based algorithms within the VTM control loop, future systems could compensate for hardware imperfections, track environmental changes, and optimize sensing–communication trade-offs in real time.

Another important research avenue lies in the co-design of RIS with VRM/VTM front-ends. Joint RIS–VTM architectures could extend the concept of virtual spatial processing beyond the transceiver itself, enabling environment-assisted sensing, coverage enhancement, and distributed spatial intelligence.

A particularly promising extension of the Virtual Transceiver Matrix paradigm lies in its conceptual compatibility with quantum information processing systems. At a fundamental level, the VTM operates as a deterministic linear transformation between physical input modes and virtual output channels, implemented through passive interferometric networks. This structure closely mirrors the linear optical transformations used in quantum computing and quantum signal processing, where unitary or near-unitary mixing of quantum states is achieved through networks of beam splitters and phase shifters.

In a quantum implementation, the physical antenna or sensor elements of the VTM can be abstracted as quantum modes, while the analog combining network corresponds to a quantum interferometer implementing a predefined transformation matrix. Such a mapping enables the realization of quantum-enhanced sensing and communication, where spatial information—such as angle, phase, or propagation delay—can be encoded into quantum states and processed through a VTM-inspired transformation. Importantly, the passive and linear nature of the VTM aligns with the constraints of near-term quantum hardware, where minimizing active elements and decoherence sources is critical.

Furthermore, the concept of floating channels in the VTM naturally maps to quantum superposition, where a single quantum state can simultaneously occupy multiple spatial or modal paths. This opens the possibility of exploiting quantum parallelism to perform spatial processing tasks—such as multi-target discrimination or channel estimation—with reduced measurement overhead. While practical realization remains a long-term challenge, the theoretical correspondence between VTM transformations and quantum linear optics suggests that the proposed architecture could serve as a bridge between classical RF interferometry and emerging quantum sensing platforms.

Another compelling research direction involves the implementation of Virtual Transceiver Matrices using integrated photonic platforms. Photonic circuits inherently support high-bandwidth, low-loss, and phase-stable linear interferometric processing, making them well suited for realizing the core operations of the VTM in the optical domain. In such systems,

RF or millimeter-wave signals can be mapped onto optical carriers using electro-optic modulation, processed through a photonic interferometric network, and subsequently detected or converted back to the electrical domain.

In a photonic VTM, optical waveguides represent physical channels, while directional couplers and phase shifters implement the analog combining coefficients that define the virtual channels. This approach enables precise and reconfigurable control of amplitude and phase weights, allowing large-scale virtual matrices to be realized with minimal footprint and excellent scalability. Compared to purely electronic implementations, photonic VTMs offer superior immunity to electromagnetic interference and reduced sensitivity to parasitic effects at high frequencies.

Moreover, linear interferometric photonics provides a natural pathway toward ultra-wideband and sub-THz operation, where conventional RF components face significant limitations. By performing spatial processing in the optical domain, photonic VTM architectures can decouple spatial resolution from RF hardware constraints, enabling compact and energy-efficient front-ends for high-frequency ISAC applications. These advantages position photonic VTMs as a promising candidate for future hybrid RF–photonic sensing and communication systems, particularly in scenarios requiring extreme bandwidth, high spatial fidelity, or dense integration.

Finally, the networking of multiple VRM/VTM-enabled nodes into cooperative and distributed systems represents a key step toward large-scale integrated sensing and communication networks. Such systems could provide enhanced spatial awareness, robustness, and scalability, contributing to the long-term vision of intelligent, software-defined, and hardware-efficient wireless infrastructures.

In conclusion, this thesis establishes a solid theoretical and experimental foundation for virtual transceiver matrix architectures and demonstrates their potential to reshape the design of future multifunctional RF systems. The proposed concepts offer a pathway toward unified, scalable, and intelligent sensing and communication platforms that bridge the gap between analog hardware efficiency and advanced spatial signal processing.

REFERENCES

[1] K. Wu, Y. Bigdeli, S. A. Keivaan, J. Deng et P. Burasa, "Integrated sensing and communication (isac) transceiver: Hardware architectures, enabling technologies, and emerging trends," *IEEE Journal of Selected Topics in Electromagnetics, Antennas and Propagation*, vol. 1, n°. 1, p. 37–64, 2025.

[2] F. Liu, C. Masouros, A. P. Petropulu, H. Griffiths et L. Hanzo, "Joint radar and communication design: Applications, state-of-the-art, and the road ahead," *IEEE Trans. Commun.*, vol. 68, n°. 6, p. 3834–3862, juin 2020.

[3] V. Shatov *et al.*, "Joint radar and communications: Architectures, use cases, aspects of radio access, signal processing, and hardware," *IEEE Access*, vol. 12, p. 47 888–47 914, 2024.

[4] L. Zheng, M. Lops, Y. C. Eldar et X. Wang, "Radar and communication coexistence: An overview—a review of recent methods," *IEEE Signal Process. Mag.*, vol. 36, n°. 5, p. 85–99, sept. 2019.

[5] S. Mazahiri, S. Ahmed et M.-S. Alouini, "A survey on joint communication-radar systems," *Front. Commun. Netw.*, vol. 1, févr. 2021.

[6] J. Li, R. G. Bosisio et K. Wu, "A six-port direct digital millimeter wave receiver," dans *Proceedings of IEEE National Telesystems Conference (NTC '94)*, San Diego, CA, USA, 1994, p. 79–82.

[7] ——, "Modeling of the six-port discriminator used in a microwave direct digital receiver," dans *Proceedings 1995 Canadian Conference on Electrical and Computer Engineering*, Montreal, QC, Canada, 1995, p. 1164–1165, vol. 2.

[8] S. O. Tatu, E. Moldovan, K. Wu et R. G. Bosisio, "A new direct millimeter-wave six-port receiver," *IEEE Transactions on Microwave Theory and Techniques*, vol. 49, n°. 12, p. 2517–2522, 2001.

[9] C.-H. Wang *et al.*, "A 60ghz low-power six-port transceiver for gigabit software-defined transceiver applications," dans *2007 IEEE International Solid-State Circuits Conference Digest of Technical Papers*, San Francisco, CA, USA, 2007.

[10] H.-S. Lim, W.-K. Kim, J.-W. Yu, H.-C. Park, W.-J. Byun et M.-S. Song, "Compact six-port transceiver for time-division duplex systems," *IEEE Microwave and Wireless Components Letters*, vol. 17, nº. 5, p. 394–396, 2007.

[11] B. Laemmle, G. Vinci, L. Maurer, R. Weigel et A. Koelpin, "A 77-ghz sige integrated six-port receiver front-end for angle-of-arrival detection," *IEEE Journal of Solid-State Circuits*, vol. 47, nº. 9, p. 1966–1973, 2012.

[12] B. Boukari, E. Moldovan, S. Affes, K. Wu, R. G. Bosisio et S. O. Tatu, "A heterodyne six-port fmcw radar sensor architecture based on beat signal phase slope techniques," *Progress In Electromagnetics Research*, vol. 93, p. 307–322, 2009.

[13] E. Moldovan, S. O. Tatu, T. Gaman, K. Wu et R. G. Bosisio, "A new 94-ghz six-port collision-avoidance radar sensor," *IEEE Transactions on Microwave Theory and Techniques*, vol. 52, nº. 3, p. 751–759, 2004.

[14] G. Vinci *et al.*, "Six-port radar sensor for remote respiration rate and heartbeat vital-sign monitoring," *IEEE Transactions on Microwave Theory and Techniques*, vol. 61, nº. 5, p. 2093–2100, 2013.

[15] B. Liu, K. Ma, Y. Wang, N. Yan, K. Li et Y. Ma, "An SISL-based 24-ghz FMCW radar with self-packaged six-port butler matrix receiver," *IEEE Transactions on Components, Packaging and Manufacturing Technology*, vol. 12, nº. 10, p. 1661–1672, 2022.

[16] X. Song *et al.*, "A six-port transceiver for frequency-division duplex systems," *IEEE Microwave and Wireless Components Letters*, vol. 28, nº. 10, p. 936–938, Oct 2018.

[17] B. L. et al., "An sisl-based 24-ghz fmcw radar with self-packaged six-port butler matrix receiver," *IEEE Trans. Compon., Packag., Manuf. Technol.*, vol. 12, nº. 10, p. 1661–1672, Oct. 2022.

[18] G. P. Riblet et E. R. B. Hansson, "Aspects of the calibration of a single six-port using a load and offset reflection standards," *IEEE Transactions on Microwave Theory and Techniques*, vol. 30, nº. 12, p. 2120–2125, 1982.

[19] P. Cheong, M. Tu, W.-W. Choi et K. Wu, "An ingenious multiport interferometric front-end for concurrent dual-band transmission," *IEEE Transactions on Microwave Theory and Techniques*, vol. 70, nº. 3, p. 1725–1731, 2022.

[20] S. A. Keivaan, P. Burasa et K. Wu, "Virtual receiver matrix and combinatory analog operations for future multifunction reconfigurable sensing and communication wireless

systems," *IEEE Transactions on Microwave Theory and Techniques*, vol. 71, nº. 1, p. 424–433, 2023.

[21] S. Ali Keivaan, P. Burasa, J. Deng et K. Wu, "Concurrent detection of 2-d angle-of-arrival and polarization enabled by virtual transceiver matrix architecture," *IEEE Transactions on Microwave Theory and Techniques*, vol. 73, nº. 9, p. 6863–6878, 2025.

[22] S. A. Keivaan, P. Burasa et K. Wu, "Virtual receiver matrix for multifunction communication and sensing wireless systems using simultaneous incident waves at the same carrier frequency," dans *2023 IEEE/MTT-S International Microwave Symposium (IMS 2023)*, San Diego, CA, USA, 2023.

[23] ——, "Joint 4d radar and communication system enabled by virtual transceiver matrix architecture for advanced automotive sensing and connectivity," dans *2025 IEEE/MTT-S International Microwave Symposium*, San Francisco, CA, USA, 2025.

[24] J. Rao *et al.*, "A novel reconfigurable intelligent surface for wide-angle passive beamforming," *IEEE Transactions on Microwave Theory and Techniques*, vol. 70, nº. 12, p. 5427–5439, 2022.

[25] S. Venkatesh, X. Lu, K. Sengupta et B. Tang, "Spatio-temporal modulated millimeter-wave antenna arrays for secure wireless links," dans *2020 IEEE International Symposium on Antennas and Propagation and North American Radio Science Meeting*, Montreal, QC, Canada, 2020, p. 1565–1566.

[26] U. Stumper, "Six-port and four-port reflectometers for complex permittivity measurements at submillimeter wavelengths," *IEEE Transactions on Microwave Theory and Techniques*, vol. 37, nº. 1, p. 222–230, 1989.

[27] A. Duenas Jimenez et C. A. Bonilla Barragan, "On the calibration of a microwave network six-port reflection analyzer," *IEEE Transactions on Instrumentation and Measurement*, vol. 56, nº. 5, p. 1763–1769, 2007.

[28] J. Li, R. G. Bosisio et K. Wu, "Computer and measurement simulation of a new digital receiver operating directly at millimeter-wave frequencies," *IEEE Transactions on Microwave Theory and Techniques*, vol. 43, nº. 12, p. 2766–2772, 1995.

[29] ——, "Dual-tone calibration of six-port junction and its application to the six-port direct digital millimetric receiver," *IEEE Transactions on Microwave Theory and Techniques*, vol. 44, nº. 1, p. 93–99, 1996.

[30] A. Honda, K. Sakaguchi, J.-I. Takada et K. Araki, “A study of nonlinearity calibration for six-port direct conversion receivers,” dans *2003 IEEE Topical Conference on Wireless Communication Technology*, Honolulu, HI, USA, 2003, p. 40–41.

[31] C. Gutierrez Miguelez, B. Huyart, E. Bergeault et L. P. Jallet, “A new automobile radar based on the six-port phase/frequency discriminator,” *IEEE Transactions on Vehicular Technology*, vol. 49, nº. 4, p. 1416–1423, 2000.

[32] S. O. Tatu, M. Aljerjawi, R. G. Bosisio et K. Wu, “Multi-port receiver and transmitter — state-of-the-art and applications,” dans *2008 Joint 6th International IEEE Northeast Workshop on Circuits and Systems and TAISA Conference*, Montreal, QC, Canada, 2008, p. 371–374.

[33] S. O. Tatu, E. Moldovan, R. G. Bosisio, K. Wu et T. A. Denidni, “Ka-band analog front-end for software-defined direct conversion receiver,” *IEEE Transactions on Microwave Theory and Techniques*, vol. 53, nº. 9, p. 2768–2776, 2005.

[34] J. C. Schiel, S. O. Tatu, K. Wu et G. Bosisio, “Six-port direct digital receiver (spdr) and standard direct receiver (sdr) results for QPSK modulation at high speeds,” dans *2002 IEEE MTT-S International Microwave Symposium Digest*, Seattle, WA, USA, 2002, p. 931–934, vol. 2.

[35] X. Xu, S. O. Tatu, E. Moldovan, R. G. Bosisio et K. Wu, “Analysis of FDSS ultra-wideband six-port receiver,” dans *Proceedings RAWCON 2002. 2002 IEEE Radio and Wireless Conference*, Boston, MA, USA, 2002, p. 87–90.

[36] J. Pérez-Dueñas, J. G. Wangüemert-Pérez et I. Molina-Fernández, “Novel modulation scheme and six-port based RAKE receiver for DS-UWB,” *IEEE Transactions on Wireless Communications*, vol. 8, nº. 7, p. 3628–3633, 2009.

[37] M. AlJerjawi, C. Nerguizian, R. G. Bosisio, Y. Xu, C. Caloz et K. Wu, “Wave-radio interferometer transceiver for UWB,” dans *2009 IEEE MTT-S International Microwave Symposium Digest*, Boston, MA, USA, 2009.

[38] P. Perez-Lara, Í. Molina-Fernandez, J. G. Wanguemert-Perez et A. Rueda-Perez, “Broadband five-port direct receiver based on low-pass and high-pass phase shifters,” *IEEE Transactions on Microwave Theory and Techniques*, vol. 58, nº. 4, p. 849–853, 2010.

[39] T. Mack, A. Honold et J.-F. Luy, “An extremely broadband software configuration six-port receiver platform,” dans *33rd European Microwave Conference Proceedings*, Munich, Germany, 2003, p. 623–626, IEEE Cat. No.03EX723C, vol. 2.

[40] X. Xu, K. Wu et R. G. Bosisio, “Software defined radio receiver based on six-port technology,” dans *IEEE MTT-S International Microwave Symposium Digest*, Philadelphia, PA, USA, 2003, p. 1059–1062, vol. 2.

[41] X. Xu, R. G. Bosisio et K. Wu, “Analysis and implementation of six-port software-defined radio receiver platform,” *IEEE Transactions on Microwave Theory and Techniques*, vol. 54, n°. 7, p. 2937–2943, 2006.

[42] H. Zhang, L. Li et K. Wu, “Software-defined six-port radar technique for precision range measurements,” *IEEE Sensors Journal*, vol. 8, n°. 10, p. 1745–1751, 2008.

[43] A. O. Olopade, A. Hasan et M. Helaoui, “Concurrent dual-band six-port receiver for multi-standard and software-defined radio applications,” *IEEE Transactions on Microwave Theory and Techniques*, vol. 61, n°. 12, p. 4252–4261, 2013.

[44] A. Hasan et M. Helaoui, “Effort-reduced calibration of six-port based receivers for cr/sdr applications,” *IEEE Journal on Emerging and Selected Topics in Circuits and Systems*, vol. 3, n°. 4, p. 586–593, 2013.

[45] A. A. L’vov, R. V. Geranin, N. Semezhev, A. A. Solopekina et P. A. L’vov, “A novel parameter estimation technique for software defined radio system based on broadband multi-port receiver,” dans *2015 International Siberian Conference on Control and Communications (SIBCON)*, Omsk, Russia, 2015, p. 1–5.

[46] X. Xu, R. G. Bosisio et K. Wu, “Software defined six-port receiver for OFDM modulation,” dans *12th International Symposium on Antenna Technology and Applied Electromagnetics and Canadian Radio Sciences Conference*, Montreal, QC, Canada, 2006, p. 1–4.

[47] S. O. Tatu, E. Moldovan, G. Brehm, K. Wu et R. G. Bosisio, “New results on MMIC six-port’s used in Ka-band direct conversion receivers,” dans *IEEE Radio Frequency Integrated Circuits (RFIC) Symposium*, Philadelphia, PA, USA, 2003, p. 523–526.

[48] N. Khaddaj Mallat, E. Moldovan, S. O. Tatu et K. Wu, “Ultra-high-speed six-port frequency-division-multiplexing v-band transceiver,” dans *Asia-Pacific Microwave Conference*, Melbourne, VIC, Australia, 2011, p. 896–899.

[49] M. D. Ardakani, H. Tadayon, R. Karimian, S. Ahmadi et M. Zaghloul, “Time division duplex beam switching system using a common multi-port junction transceiver,” dans *2023 IEEE International Symposium on Antennas and Propagation and USNC-URSI Radio Science Meeting*, Portland, OR, USA, 2023.

[50] Y. Ding et K. Wu, “Half-mode substrate integrated waveguide six-port front-end circuits for direct-conversion transceiver design,” dans *2008 IEEE MTT-S International Microwave Symposium Digest*, Atlanta, GA, USA, 2008, p. 1175–1178.

[51] T. Djerafi, M. Daigle, H. Boutayeb, X. Zhang et K. Wu, “Substrate integrated waveguide six-port broadband front-end circuit for millimeter-wave radio and radar systems,” dans *2009 European Microwave Conference (EuMC)*, Rome, Italy, 2009, p. 77–80.

[52] B. Laemmle *et al.*, “A fully integrated 120-ghz six-port receiver front-end in a 130-nm sige bicmos technology,” dans *2013 IEEE 13th Topical Meeting on Silicon Monolithic Integrated Circuits in RF Systems*, Austin, TX, USA, 2013, p. 129–131.

[53] F. Lurz, F. Michler, B. Scheiner, R. Weigel et A. Koelpin, “Microw(h)att?! ultralow-power six-port radar: realizing highly integrated portable radar systems with good motion sensitivity at relatively low cost,” *IEEE Microwave Magazine*, vol. 19, n°. 1, p. 91–98, 2018.

[54] M. D. Ardakani, R. Karimian, S. Ahmadi, M. Zaghloul et A. Zaghloul, “All-in-one integrated multiport receiver for giga-speed backhaul applications,” dans *2024 International Applied Computational Electromagnetics Society Symposium (ACES)*, Orlando, FL, USA, 2024, p. 1–2.

[55] Z. Song, S. Tatu, M. R. Soleymani, K. Wu et R. G. Bosisio, “Rf coding in mmic six port receiver,” dans *2003 Canadian Conference on Electrical and Computer Engineering (CCECE)*, Montreal, QC, Canada, 2003, p. 1929–1931, vol. 3.

[56] M. D. Ardakani, R. Karimian et S. O. Tatu, “60-ghz-band mhmic frequency multiplier module for multi-port interferometer receivers,” dans *2021 United States National Committee of URSI National Radio Science Meeting (USNC-URSI NRSM)*, Boulder, CO, USA, 2021, p. 230–231.

[57] I. Hussain et K. Wu, “Low-if interferometric receiver architecture for massive-iot wireless systems,” dans *2020 50th European Microwave Conference (EuMC)*, Utrecht, Netherlands, 2021, p. 694–697.

[58] M. D. Ardakani et S. O. Tatu, “V-band six-port interferometer receiver: high data-rate wireless applications, BER and EVM analysis, and CFO compensation,” *IEEE Access*, vol. 9, p. 160 847–160 854, 2021.

[59] I. Hussain, L.-P. Carignan et K. Wu, “Balanced detection in multiport direct-conversion interferometric receiver for IoT systems,” *IEEE Systems Journal*, vol. 18, nº. 1, p. 612–619, 2024.

[60] E. Moldovan, S. O. Tatu, S. Affes, R. G. Bosisio et K. Wu, “W-band substrate integrated waveguide radar sensor based on multi-port technology,” dans *2007 European Radar Conference*, Munich, Germany, 2007, p. 174–177.

[61] P. Feng, B. Huang, Y. Cao, J. Chen et S. Yan, “A novel compact broadband SIW six-port junction for angle-of-arrival applications,” *IEEE Transactions on Instrumentation and Measurement*, vol. 72, p. 1–8, 2023, art. no. 8003308.

[62] S. O. Tatu, B. Boukari, E. Moldovan, R. G. Bosisio et K. Wu, “Millimeter-wave multi-port radar sensor with integrated receiver front-end for automotive applications,” dans *2012 IEEE/MTT-S International Microwave Symposium Digest*, Montreal, QC, Canada, 2012, p. 1–3.

[63] J. Deng, P. Burasa et K. Wu, “Unified microwave terahertz waveguide coupler for multiband wireless applications,” *IEEE Transactions on Components, Packaging and Manufacturing Technology*, vol. 15, nº. 5, p. 1032–1043, 2025.

[64] J. Deng, P. Burasa, S. A. Keivaan et K. Wu, “Waveguide receiver array for joint communication, sensing, and power transfer systems,” *IEEE Transactions on Microwave Theory and Techniques*, 2025, early access.

[65] P. Burasa, J. Deng et K. Wu, “A 300-GHz dual-polarized CMOS waveguide receiver for high-density terahertz integrated multichannel wireless systems-on-chip,” *IEEE Transactions on Microwave Theory and Techniques*, vol. 73, nº. 5, p. 3044–3058, 2025.

[66] M. Mailand et H.-J. Jentschel, “An effort reduced six-port direct conversion receiver and its calibration,” dans *IEEE Wireless Communications and Networking Conference*, New Orleans, LA, USA, 2005, p. 568–572, vol. 1.

[67] G. Vinci, A. Koelpin et R. Weigel, “Employing six-port technology for phase-measurement-based calibration of automotive radar,” dans *2009 Asia-Pacific Microwave Conference*, Singapore, 2009, p. 329–332.

[68] C. de la Morena-Alvarez-Palencia, K. Mabrouk, B. Huyart, A. Mbaye et M. Burgos-Garcia, "Direct baseband i-q regeneration method for five-port receivers improving dc-offset and second-order intermodulation distortion rejection," *IEEE Transactions on Microwave Theory and Techniques*, vol. 60, n°. 8, p. 2634–2643, 2012.

[69] A. Hasan et M. Helaoui, "Novel modeling and calibration approach for multiport receivers mitigating system imperfections and hardware impairments," *IEEE Transactions on Microwave Theory and Techniques*, vol. 60, n°. 8, p. 2644–2653, 2012.

[70] W. Zhang, A. Hasan, F. M. Ghannouchi, M. Helaoui, Y. Wu et Y. Liu, "Novel calibration algorithm of multiport wideband receivers based on real-valued time-delay neural networks," *IEEE Transactions on Microwave Theory and Techniques*, vol. 64, n°. 11, p. 3540–3548, 2016.

[71] ——, "Design and calibration of wideband multiport homodyne wireless receivers," *IEEE Transactions on Instrumentation and Measurement*, vol. 66, n°. 12, p. 3160–3169, 2017.

[72] S. Linz, F. Lurz, R. Weigel et A. Koelpin, "A review on six-port radar and its calibration techniques," dans *2018 22nd International Microwave and Radar Conference (MIKON)*, Poznan, Poland, 2018, p. 80–83.

[73] R. Chen, M. Tu, P. Cheong et W.-W. Choi, "Calibration techniques for concurrent dual-band multiport receivers," *IEEE Microwave and Wireless Technology Letters*, vol. 34, n°. 10, p. 1202–1205, 2024.

[74] K. Mabrouk, B. Huyart et G. Neveux, "3-d aspect in the five-port technique for zero-if receivers and a new blind calibration method," *IEEE Transactions on Microwave Theory and Techniques*, vol. 56, n°. 6, p. 1389–1396, 2008.

[75] H. Peng, Z. Yang et T. Yang, "Calibration of a six-port receiver for direction finding using the artificial neural network technique," *Progress In Electromagnetics Research Letters*, vol. 27, p. 17–24, 2011.

[76] H. Peng, T. Yang et Z. Yang, "Calibration of a six-port position sensor via support vector regression," *Progress In Electromagnetics Research C*, vol. 26, p. 71–81, 2012.

[77] S. Linz, F. Lurz, R. Weigel et A. Koelpin, "Squircle-based calibration algorithm for six-port radar," *IEEE Transactions on Microwave Theory and Techniques*, vol. 67, n°. 10, p. 4023–4030, 2019.

[78] J. A. Lima, J. M. W. Rogers et R. E. Amaya, “Optimization of EVM through diode bias control using a blind algorithm applied to multiport receivers,” *IEEE Transactions on Circuits and Systems II: Express Briefs*, vol. 62, nº. 3, p. 286–290, 2015.

[79] ——, “Finding the initial estimate for the diode bias point in multiport receivers,” *IEEE Transactions on Circuits and Systems II: Express Briefs*, vol. 63, nº. 1, p. 34–38, 2016.

[80] M. D. Ardakani, H. Tadayon, R. Karimian, S. Ahmadi et M. Zaghloul, “Digital predistortion implementation in short-range mm-wave six-port transceivers,” dans *2023 IEEE USNC-URSI Radio Science Meeting (Joint with AP-S Symposium)*, Portland, OR, USA, 2023, p. 93–94.

[81] M. Tu, P. Cheong, W.-W. Choi et K. Wu, “Multiport transmitter front-end architecture for concurrent dual-band digital predistortion,” *IEEE Transactions on Circuits and Systems II: Express Briefs*, vol. 71, nº. 2, p. 572–576, 2024.

[82] Y. Bigdeli, P. Burasa et K. Wu, “Extending the dynamic range of square-law power detectors for large-scale receiver arrays,” *IEEE Microwave and Wireless Technology Letters*, 2025, early access.

[83] B. Mnasri, T. Djerafi, S. Tatu et K. Wu, “Dynamic range improvement of six-port interferometer receivers,” dans *2017 XXXIInd General Assembly and Scientific Symposium of the International Union of Radio Science (URSI GASS)*, Montreal, QC, Canada, 2017, p. 1–3.

[84] A. Hamed, O. Habibpour, M. Saeed, H. Zirath et R. Negra, “W-band graphene-based six-port receiver,” *IEEE Microwave and Wireless Components Letters*, vol. 28, nº. 4, p. 347–349, 2018.

[85] W. Zhang, A. Hasan, F. M. Ghannouchi, M. Helaoui, Y. Wu et Y. Liu, “Concurrent dual-band receiver based on novel six-port correlator for wireless applications,” *IEEE Access*, vol. 5, p. 25 826–25 834, 2017.

[86] W. Zhang *et al.*, “Concurrent dual-band low intermediate frequency receiver based on the multiport correlator and single local oscillator,” *IEEE Microwave and Wireless Components Letters*, vol. 28, nº. 4, p. 353–355, 2018.

[87] W. Zhang, A. Hasan, F. M. Ghannouchi, M. Helaoui, Y. Wu et Y. Liu, “Concurrent dual-band receiver based on the multi-port correlator for wireless applications,” *IEEE*

Transactions on Circuits and Systems II: Express Briefs, vol. 65, n°. 6, p. 759–763, 2018.

[88] J. Moghaddasi et K. Wu, "Unified radar-communication (radcom) multi-port interferometer transceiver," dans *2013 European Radar Conference*, Nuremberg, Germany, 2013, p. 479–482.

[89] I. Hussain et K. Wu, "Cooperative interferometric receiver with time-agile radar sensing and radio communication capability," *IEEE Sensors Journal*, vol. 22, n°. 24, p. 23 896–23 905, 2022.

[90] ——, "Concurrent dual-band heterodyne interferometric receiver for multistandard and multifunction wireless systems," *IEEE Transactions on Microwave Theory and Techniques*, vol. 69, n°. 11, p. 4995–5007, 2021.

[91] P. Cheong et K. Wu, "Compendious concurrent dual-band receiver based on multiport interferometric architecture," *IEEE Transactions on Microwave Theory and Techniques*, vol. 69, n°. 7, p. 3388–3398, 2021.

[92] B. Mnasri, T. Djerafi, S. Tatu et K. Wu, "Dual input interferometer direct conversion receiver architecture," dans *2018 18th International Symposium on Antenna Technology and Applied Electromagnetics (ANTEM)*, Waterloo, ON, Canada, 2018, p. 1–3.

[93] J. Deng, P. Burasa et K. Wu, "All-in-one dual-polarization waveguide receiver for multichannel wireless systems," *IEEE Transactions on Microwave Theory and Techniques*, vol. 72, n°. 8, p. 4998–5013, 2024.

[94] ——, "Joint multiband linear interferometric receiver for integrated microwave and terahertz sensing and communication systems," *IEEE Transactions on Microwave Theory and Techniques*, vol. 72, n°. 9, p. 5550–5562, 2024.

[95] ——, "Multichannel and multifunction interferometric receiver architectures for multistandard millimeter-wave and terahertz applications," dans *2024 IEEE Wireless and Microwave Technology Conference (WAMICON)*, Clearwater, FL, USA, 2024, p. 1–4.

[96] ——, "Self-contained dual-input interferometric receiver for paralleled-multichannel wireless systems," *IEEE Transactions on Circuits and Systems I: Regular Papers*, vol. 71, n°. 2, p. 934–947, 2024.

[97] B. Boukari, E. Moldovan, S. Affes, K. Wu, R. G. Bosisio et S. O. Tatu, "Six-port fmcw collision avoidance radar sensor configurations," dans *2008 Canadian Conference on Electrical and Computer Engineering*, Niagara Falls, ON, Canada, 2008, p. 305–308.

[98] E. Moldovan, B. Boukari, S. O. Tatu, R. G. Bosisio et K. Wu, “77 ghz compact multi-port radar sensor for automotive applications,” dans *2011 8th European Radar Conference*, Manchester, UK, 2011, p. 105–108.

[99] S. A. Keivaan, P. Burasa et K. Wu, “Interferometric receiver architecture for multi-function wireless systems,” dans *2022 52nd European Microwave Conference (EuMC)*, Milan, Italy, 2022, p. 16–19.

[100] L. Chioukh, T. Djerafi, D. Deslandes et K. Wu, “Improvements of cardiopulmonary monitoring using harmonic six-port radar system,” dans *Global Symposium on Millimeter-Waves (GSMM)*, Montreal, QC, Canada, 2015, p. 1–3.

[101] A. Koelpin, F. Lurz, S. Linz, S. Mann, C. Will et S. Lindner, “Six-port based interferometry for precise radar and sensing applications,” *Sensors*, vol. 16, p. 1556, 2016.

[102] J. Moghaddasi, T. Djerafi et K. Wu, “Multiport interferometer-enabled 2-d angle of arrival (aoa) estimation system,” *IEEE Transactions on Microwave Theory and Techniques*, vol. 65, n°. 5, p. 1767–1779, 2017.

[103] H. Arab, S. Dufour, E. Moldovan, C. Akyel et S. O. Tatu, “A 77-ghz six-port sensor for accurate near-field displacement and doppler measurements,” *Sensors*, vol. 18, p. 2565, 2018.

[104] A. A. Sakr, W. M. Dyab et K. Wu, “A dually polarized six-port junction based on polarization-selective coupling for polarization-inclusive remote sensing,” *IEEE Transactions on Microwave Theory and Techniques*, vol. 66, n°. 8, p. 3817–3827, 2018.

[105] R. Mirzavand et P. Mousavi, “A zero-power sensor using multi-port direct-conversion sensing,” *IEEE Sensors Journal*, vol. 18, n°. 22, p. 9243–9250, 2018.

[106] S. Mann *et al.*, “High-precision interferometric radar for sheet thickness monitoring,” *IEEE Transactions on Microwave Theory and Techniques*, vol. 66, n°. 6, p. 3153–3166, 2018.

[107] B. Mnasri, P. Burasa, S. Tatu et K. Wu, “Interferometer based direction-of-arrival detection system,” dans *2018 18th International Symposium on Antenna Technology and Applied Electromagnetics (ANTEM)*, Waterloo, ON, Canada, 2018, p. 1–3.

[108] W. Dyab, A. A. Sakr et K. Wu, “Millimeter-wave polarization-inclusive remote sensing system based on dually-polarized six-port junction,” dans *2018 11th Global Symposium on Millimeter Waves (GSMM)*, Boulder, CO, USA, 2018, p. 1–3.

[109] N. Khalid, R. Mirzavand, H. Saghlatoon, M. M. Honari et P. Mousavi, “A three-port zero-power rfid sensor architecture for iot applications,” *IEEE Access*, vol. 8, p. 66 888–66 897, 2020.

[110] S. O. Tatu et E. Moldovan, “Millimeter-wave multi-port interferometric radar sensors: evolution of fabrication and characterization technologies,” *Sensors*, vol. 20, p. 5477, 2020.

[111] P. Cheong et K. Wu, “Full-range CSRR-based angular displacement sensing with multiport interferometric platform,” *IEEE Transactions on Microwave Theory and Techniques*, vol. 69, n°. 11, p. 4813–4821, 2021.

[112] N. Khalid, A. K. Iyer et R. Mirzavand, “A batteryless six-port rfid-based wireless sensor architecture for iot applications,” *IEEE Internet of Things Journal*, vol. 9, n°. 19, p. 18 550–18 558, 2022.

[113] X. Yang, C. Qi, J. Xie, X. Zhang, Z. Liao et X. Sun, “Unambiguous 2-d angle-of-arrival estimation receiver based on a 16-port interferometer,” *IEEE Transactions on Instrumentation and Measurement*, vol. 72, p. 1–10, 2023, art. no. 8003410.

[114] B. Tegowski et A. Koelpin, “Accuracy limitations of interferometric radar owing to the radar cross section of its antenna,” *IEEE Transactions on Microwave Theory and Techniques*, vol. 72, n°. 7, p. 4317–4324, 2024.

[115] J. Moghaddasi et K. Wu, “Millimeter-wave multifunction multiport interferometric receiver for future wireless systems,” *IEEE Transactions on Microwave Theory and Techniques*, vol. 66, n°. 3, p. 1452–1466, 2018.

[116] J. Deng, P. Burasa, S. A. Keivaan et K. Wu, “Spatially distributed polarization receiver array for communication and sensing multifunction systems,” dans *2024 54th European Microwave Conference (EuMC)*, Paris, France, 2024, p. 148–151.

[117] Y. Bigdeli, S. A. Keivaan, P. Burasa et K. Wu, “Towards the development of large-scale multifunction array transceiver systems,” dans *2023 Asia-Pacific Microwave Conference (APMC)*, Taipei, Taiwan, 2023, p. 890–892.

[118] B. Mnasri, T. Djerafi, S. O. Tatu et K. Wu, “Spatially distributed multi-input interferometric receiver for 5g wireless systems and beyond,” *IEEE Transactions on Microwave Theory and Techniques*, vol. 67, n°. 7, p. 2904–2915, 2019.

[119] S. A. Keivaan, P. Burasa et K. Wu, “Virtual receiver matrix for future multifunction wireless systems,” dans *2022 IEEE/MTT-S International Microwave Symposium (IMS 2022)*, Denver, CO, USA, 2022, p. 386–389.

[120] ——, “Virtual transceiver matrix for future programmable wireless sensing and communication frontends,” dans *2023 IEEE MTT-S International Conference on Numerical Electromagnetic and Multiphysics Modeling and Optimization (NEMO)*, Winnipeg, MB, Canada, 2023, p. 87–90.

[121] R. M. Evina, C. Hannachi et S. O. Tatu, “Optimization of 16-qam for mitigating impairments in 60 ghz six-port receivers,” dans *2021 IEEE Topical Conference on Wireless Sensors and Sensor Networks (WiSNeT)*, San Diego, CA, USA, 2021, p. 47–49.

[122] S. Tavoseh et A. Mohammadi, “Linearization of microwave power amplifier using multiport receiver with machine learning techniques in x-band,” *Analog Integrated Circuits and Signal Processing*, vol. 122, p. 4, 2025.

[123] Y. Su et Z. N. Chen, “Isolation improvement and beam manipulation of dual-polarized ris-halved lens antennas for compact transceiver systems,” *IEEE Transactions on Antennas and Propagation*, vol. 67, n°. 9, p. 5877–5884, 2019.

[124] S. Venkatesh, X. Lu, H. Saeidi et K. Sengupta, “Reconfigurable multifunctional terahertz holographic metasurface using CMOS chip tiling,” dans *2021 IEEE 19th International Symposium on Antenna Technology and Applied Electromagnetics (ANTEM)*, Winnipeg, MB, Canada, 2021, p. 1–3.

[125] K. Sengupta, S. Venkatesh, H. Saeidi et X. Lu, “Reconfigurable intelligent surfaces enabled by silicon chips for secure and robust mmwave and THz wireless communication,” dans *ESSCIRC 2022 – IEEE 48th European Solid State Circuits Conference (ESSCIRC)*, Milan, Italy, 2022, p. 546–549.

[126] J. Kim, J. Kim, J. H. Oh, S.-H. Wi et J. Oh, “Rotated feed-combined reconfigurable transmit RIS with disparate deployment of 1-bit hybrid units for B5G/6G,” *IEEE Transactions on Antennas and Propagation*, vol. 71, n°. 6, p. 5457–5462, 2023.

[127] P. Wang *et al.*, “A machine learning framework for the design of STCDME structures in RIS applications,” *IEEE Transactions on Microwave Theory and Techniques*, vol. 72, n°. 3, p. 1467–1479, 2024.

[128] J. Rao, Y. Zhang, S. Tang, Z. Li, C.-Y. Chiu et R. Murch, "A shared-aperture dual-band sub-6 ghz and mmwave reconfigurable intelligent surface with independent operation," *IEEE Transactions on Microwave Theory and Techniques*, 2025, early access.

[129] D. Inserra *et al.*, "Dual-orthogonal polarization amplifying reconfigurable intelligent surface with reflection amplifier based on passive circulator," *IEEE Transactions on Microwave Theory and Techniques*, vol. 72, nº. 7, p. 4383–4394, 2024.

[130] S. Alamdar *et al.*, "A 16 × 16 array composed of 4 × 4 fully scalable reconfigurable intelligent surfaces for 2.4 ghz wi-fi using rfid distributed control," *IEEE Transactions on Microwave Theory and Techniques*, 2025, early access.

[131] Y. Yang, M. Vaseem, R. Wang, B. Makki et A. Shamim, "A fully screen-printed vanadium-dioxide switch-based wideband reconfigurable intelligent surface for 5g and beyond," *IEEE Transactions on Microwave Theory and Techniques*, 2025, early access.

[132] I.-T. Chen, C. A. Lynch, A. Eid, J. G. D. Hester, K. Zeng et M. M. Tentzeris, "Additively manufactured semipassive rotman lens-based RIS-assisted mmid tag system for beyond-5g wireless networks in complex environments," *IEEE Transactions on Microwave Theory and Techniques*, vol. 73, nº. 1, p. 650–660, 2025.

[133] T. Mazloum *et al.*, "Indoor channel characterization using transmitting and reflecting RIS at mmwaves," *IEEE Transactions on Antennas and Propagation*, vol. 73, nº. 4, p. 2026–2037, 2025.

[134] B. Liu, Q. Zhang et H. Wong, "Multifunctional reconfigurable intelligent surface for wideband beamforming and frequency-and-spatial-diverse microwave sensing," *IEEE Transactions on Antennas and Propagation*, vol. 73, nº. 2, p. 1135–1148, 2025.

[135] S. Venkatesh, H. Saeidi, K. Sengupta et X. Lu, "Active and passive reconfigurable intelligent surfaces at mm-wave and THz bands enabled by CMOS integrated chips," dans *2023 IEEE Wireless and Microwave Technology Conference (WAMICON)*, Melbourne, FL, USA, 2023, p. 113–116.

[136] J. Rao, Y. Zhang, S. Tang, Z. Li, C.-Y. Chiu et R. Murch, "An active reconfigurable intelligent surface utilizing phase-reconfigurable reflection amplifiers," *IEEE Transactions on Microwave Theory and Techniques*, vol. 71, nº. 7, p. 3189–3202, 2023.

[137] Y. Youn *et al.*, "Liquid-crystal-driven reconfigurable intelligent surface with cognitive sensors for self-sustainable operation," *IEEE Transactions on Antennas and Propagation*, vol. 71, nº. 12, p. 9415–9423, 2023.

[138] Y. Zhao, P. Chen, M. Sun, T. Luo et Z. Cao, "RIS-aided sensing system with localization function: fundamental and practical design," *IEEE Sensors Journal*, vol. 24, n°. 1, p. 506–514, 2024.

[139] X. Wang, Z. Lin, F. Lin et L. Hanzo, "Joint hybrid 3d beamforming relying on sensor-based training for reconfigurable intelligent surface aided terahertz-based multiuser massive MIMO systems," *IEEE Sensors Journal*, vol. 22, n°. 14, p. 14 540–14 552, 2022.

[140] E. Westberg, J. Staudinger, J. Annes et V. Shilimkar, "5g infrastructure rf solutions: Challenges and opportunities," *IEEE Microwave Magazine*, vol. 20, n°. 12, p. 51–58, 2019.

[141] J. Moghaddasi et K. Wu, "Multifunction, multiband, and multimode wireless receivers: A path toward the future," *IEEE Microwave Magazine*, vol. 21, n°. 12, p. 104–125, Dec 2020.

[142] S. Shinjo, K. Nakatani, K. Tsutsumi et H. Nakamizo, "Integrating the front end: A highly integrated rf front end for high-shf wide-band massive mimo in 5g," *IEEE Microwave Magazine*, vol. 18, n°. 5, p. 31–40, Jul–Aug 2017.

[143] K. Wu, "Mhz-through-thz (mtt) challenges and opportunities [president's column]," *IEEE Microwave Magazine*, vol. 17, n°. 2, p. 8–10, Feb 2016.

[144] J. C. Rudell, V. Bhagavatula et W. C. Wesson, "Future integrated sensor radios for long-haul communication," *IEEE Communications Magazine*, vol. 52, n°. 4, p. 101–109, Apr 2014.

[145] T. S. Rappaport, Y. Xing, G. R. MacCartney, A. F. Molisch, E. Mellios et J. Zhang, "Overview of millimeter wave communications for fifth-generation (5g) wireless networks—with a focus on propagation models," *IEEE Transactions on Antennas and Propagation*, vol. 65, n°. 12, p. 6213–6230, Dec 2017.

[146] L. Taponecco, A. A. D'Amico et U. Mengali, "Joint toa and aoa estimation for uwb localization applications," *IEEE Transactions on Wireless Communications*, vol. 10, n°. 7, p. 2207–2217, Jul 2011.

[147] J. A. Nanzer, S. R. Mghabghab, S. M. Ellison et A. Schlegel, "Distributed phased arrays: Challenges and recent advances," *IEEE Transactions on Microwave Theory and Techniques*, vol. 69, n°. 11, p. 4893–4907, Nov 2021.

[148] D. Zhao *et al.*, "Millimeter-wave integrated phased arrays," *IEEE Transactions on Circuits and Systems I: Regular Papers*, vol. 68, nº. 10, p. 3977–3990, Oct 2021.

[149] N. Li *et al.*, "A four-element 7.5–9-ghz phased-array receiver with 1–8 simultaneously reconfigurable beams in 65-nm cmos," *IEEE Transactions on Microwave Theory and Techniques*, vol. 69, nº. 1, p. 1114–1126, Jan 2021.

[150] M. Gal-Katziri, C. Ives, A. Khakpour et A. Hajimiri, "Optically synchronized phased arrays in cmos," *IEEE Journal of Solid-State Circuits*, vol. 57, nº. 6, p. 1578–1593, Jun 2022.

[151] C.-N. Chen *et al.*, "38-ghz phased array transmitter and receiver based on scalable phased array modules with endfire antenna arrays for 5g mmw data links," *IEEE Transactions on Microwave Theory and Techniques*, vol. 69, nº. 1, p. 980–999, Jan 2021.

[152] H. Hashemi, X. Guan, A. Komijani et A. Hajimiri, "A 24-ghz sige phased-array receiver—lo phase-shifting approach," *IEEE Transactions on Microwave Theory and Techniques*, vol. 53, nº. 2, p. 614–626, Feb 2005.

[153] M. Zahra *et al.*, "A 2–5.5 ghz beamsteering receiver ic with 4-element vivaldi antenna array," *IEEE Transactions on Microwave Theory and Techniques*, vol. 68, nº. 9, p. 3852–3860, Sep 2020.

[154] A. Gupta et R. K. Jha, "A survey of 5g network: Architecture and emerging technologies," *IEEE Access*, vol. 3, p. 1206–1232, 2015.

[155] M. Kamel, W. Hamouda et A. Youssef, "Ultra-dense networks: A survey," *IEEE Communications Surveys and Tutorials*, vol. 18, nº. 4, p. 2522–2545, 2016.

[156] A. A. Farid, A. S. H. Ahmed, A. Dhananjay et M. J. W. Rodwell, "A fully packaged 135-ghz multiuser mimo transmitter array tile for wireless communications," *IEEE Transactions on Microwave Theory and Techniques*, vol. 70, nº. 7, p. 3396–3405, Jul 2022.

[157] P. Taghikhani, K. Buisman et C. Fager, "Hybrid beamforming transmitter modeling for millimeter-wave mimo applications," *IEEE Transactions on Microwave Theory and Techniques*, vol. 68, nº. 11, p. 4740–4752, Nov 2020.

[158] T. Kwon, Y.-G. Lim, B.-W. Min et C.-B. Chae, "Rf lens-embedded massive mimo systems: Fabrication issues and codebook design," *IEEE Transactions on Microwave Theory and Techniques*, vol. 64, nº. 7, p. 2256–2271, Jul 2016.

[159] R. Feger, C. Wagner, S. Schuster, S. Scheiblhofer, H. Jager et A. Stelzer, “A 77-ghz fmcw mimo radar based on an sige single-chip transceiver,” *IEEE Transactions on Microwave Theory and Techniques*, vol. 57, nº. 5, p. 1020–1035, May 2009.

[160] H. Krishnaswamy et L. Zhang, “Analog and rf interference mitigation for integrated mimo receiver arrays,” *Proceedings of the IEEE*, vol. 104, nº. 3, p. 561–575, Mar 2016.

[161] M. Hofmann, G. Fischer, R. Weigel et D. Kissinger, “Microwave-based noninvasive concentration measurements for biomedical applications,” *IEEE Transactions on Microwave Theory and Techniques*, vol. 61, nº. 5, p. 2195–2204, May 2013.

[162] S. A. Keivaan, P. Burasa et K. Wu, “Virtual receiver matrix for future multifunction wireless systems,” dans *IEEE/MTT-S International Microwave Symposium (IMS)*, 2022, p. 386–389.

[163] P. Burasa, B. Mnasri et K. Wu, “Millimeter-wave cmos sourceless receiver architecture for 5g-served ultra-low-power sensing and communication systems,” *IEEE Transactions on Microwave Theory and Techniques*, vol. 67, nº. 5, p. 1688–1696, May 2019.

[164] J. H. Deng, H. Xiong, Q. Yang, M. Suo, J. Y. Xie et H. Q. Zhang, “Metasurface-based microwave power detector for polarization angle detection,” *IEEE Sensors Journal*, vol. 23, nº. 19, p. 22 459–22 465, Oct 2023.

[165] K. Hietpas, “Next-generation das technology emerges to serve 5g needs,” *IEEE Journal of Microwaves*, vol. 66, nº. 5, p. 106–112, May 2023.

[166] Y. Zhang, R. Huang, G. Wang, Z. H. Jiang et W. Hong, “A low-cost polarization detection approach enabled by energy harvesting metasurface: Concept, design, and experiment,” *IEEE Transactions on Microwave Theory and Techniques*, 2024.

[167] J. Kaiser, “A scannable, beam-forming interferometer array system,” dans *International Symposium Digest on Antennas and Propagation*, Washington, DC, USA, Mar 1978, p. 114–117.

[168] R. J. Lioio, G. E. Clayton et R. A. Deaton, “Phase and time-difference precision direction finding system,” américain Brevet US 5,724,047 A, Mar 3 1998.

[169] S. M. Moon, J. W. Yu et M. Q. Lee, “Cmos four-port direct conversion receiver for bpsk demodulation,” *IEEE Microwave and Wireless Components Letters*, vol. 19, nº. 9, p. 581–583, Sep 2009.

[170] J. Östh, M. Karlsson, A. Serban et S. Gong, "M-qam six-port modulator using only binary baseband data, electrical or optical," *IEEE Transactions on Microwave Theory and Techniques*, vol. 61, nº. 6, p. 2506–2513, Jun 2013.

[171] A. Serban *et al.*, "Six-port transceiver for 6–9 ghz ultrawideband systems," *Microwave and Optical Technology Letters*, vol. 52, nº. 3, p. 740–746, Mar 2010.

[172] P. Guan *et al.*, "A 33.5–37.5-ghz four-element phased-array transceiver front-end with hybrid architecture phase shifters and gain controllers," *IEEE Transactions on Microwave Theory and Techniques*, vol. 71, nº. 9, p. 4129–4143, Sep 2023.

[173] W. Zhu *et al.*, "A 24–28-ghz four-element phased-array transceiver front end with 21.1%/16.6% transmitter peak/op1db pae and subdegree phase resolution supporting 2.4 gb/s in 256-qam for 5g communications," *IEEE Transactions on Microwave Theory and Techniques*, vol. 69, nº. 6, p. 2854–2869, Jun 2021.

[174] X. Liu *et al.*, "Area-efficient 28-ghz four-element phased-array transceiver front-end achieving 25.2% tx efficiency at 15.68-dbm output power," *IEEE Transactions on Microwave Theory and Techniques*, vol. 71, nº. 2, p. 654–668, Feb 2023.

[175] E. Biglieri *et al.*, *MIMO Wireless Communications*. Cambridge University Press, Apr 2010.

[176] E. E. Djoumessi, S. O. Tatu et K. Wu, "Frequency-agile dual-band direct conversion receiver for cognitive radio systems," *IEEE Transactions on Microwave Theory and Techniques*, vol. 58, nº. 1, p. 87–94, Jan 2010.

[177] J. Hasch, E. Topak, R. Schnabel, T. Zwick, R. Weigel et C. Waldschmidt, "Millimeter-wave technology for automotive radar sensors in the 77 ghz frequency band," *IEEE Trans. Microw. Theory Techn.*, vol. 60, nº. 3, p. 845–860, Mar. 2012.

[178] P. Kumari, J. Choi, N. González-Prelcic et R. W. Heath, "Ieee 802.11ad-based radar: An approach to joint vehicular communication-radar system," *IEEE Trans. Veh. Technol.*, vol. 67, nº. 4, p. 3012–3027, Apr. 2018.

[179] C. Waldschmidt, J. Hasch et W. Menzel, "Automotive radar — from first efforts to future systems," *IEEE J. Microw.*, vol. 1, nº. 1, p. 135–148, Jan. 2021.

[180] L. F. et al., "4d mmwave radar for autonomous driving perception: A comprehensive survey," *IEEE Trans. Intell. Veh.*, vol. 9, nº. 4, p. 4606–4620, Apr. 2024.

[181] L. W. et al., “Multi-modal and multi-scale fusion 3d object detection of 4d radar and lidar for autonomous driving,” *IEEE Trans. Veh. Technol.*, vol. 72, nº. 5, p. 5628–5641, May 2023.

[182] D. S. et al., “System performance of a 79 ghz high-resolution 4d imaging mimo radar with 1728 virtual channels,” *IEEE J. Microw.*, vol. 2, nº. 4, p. 637–647, Oct. 2022.

[183] M. L. et al., “Integrated sensor fusion based on 4d mimo radar and camera: A solution for connected vehicle applications,” *IEEE Veh. Technol. Mag.*, vol. 17, nº. 4, p. 38–46, Dec. 2022.

[184] E. Björnson, L. Sanguinetti, J. Hoydis et M. Debbah, “Optimal design of energy-efficient multi-user mimo systems: Is massive mimo the answer?” *IEEE Trans. Wireless Commun.*, vol. 14, nº. 6, p. 3059–3075, Jun. 2015.

[185] J.-H. Li et X. Liao, “Theoretical and experimental investigations of an integrated microwave power, frequency, and phase detector for x-band applications,” *IEEE Sensors Journal*, vol. 23, nº. 1, p. 219–225, 2023.

[186] F. M. et al., “A clinically evaluated interferometric continuous-wave radar system for the contactless measurement of human vital parameters,” *Sensors*, vol. 19, nº. 11, p. 2492, 2019.

[187] Z. Peng, L. Ran et C. Li, “A k-band portable fmcw radar with beamforming array for short-range localization and vital-doppler targets discrimination,” *IEEE Trans. Microw. Theory Techn.*, vol. 65, nº. 9, p. 3443–3452, Sep. 2017.

[188] H.-C. Yen, L.-Y. O. Yang et Z.-M. Tsai, “3-d indoor localization and identification through rssi-based angle of arrival estimation with real wi-fi signals,” *IEEE Trans. Microw. Theory Techn.*, vol. 70, nº. 10, p. 4511–4527, Oct. 2022.

[189] T. M. et al., “A cmos 76–81-ghz 2-tx 3-rx fmcw radar transceiver based on mixed-mode pll chirp generator,” *IEEE J. Solid-State Circuits*, vol. 55, nº. 2, p. 233–248, Feb. 2020.

[190] G. X. et al., “3-d high-resolution imaging and array calibration of ground-based millimeter-wave mimo radar,” *IEEE Trans. Microw. Theory Techn.*, vol. 72, nº. 8, p. 4919–4931, Aug. 2024.

[191] S.-Y. J. et al., “W-band mimo fmcw radar system with simultaneous transmission of orthogonal waveforms for high-resolution imaging,” *IEEE Trans. Microw. Theory Techn.*, vol. 66, nº. 11, p. 5051–5064, Nov. 2018.

[192] C. Wang, F. Haider, X. Gao, X. You, Y. Yang, D. Yuan, H. M. Aggoune, H. Haas, S. Fletcher et E. Hepsaydir, "Cellular architecture and key technologies for 5g wireless communication networks," *IEEE Communications Magazine*, vol. 52, n°. 2, p. 122–130, Feb. 2014.

[193] N. Chi, Y. Zhou, Y. Wei et F. Hu, "Visible light communication in 6g: Advances, challenges, and prospects," *IEEE Vehicular Technology Magazine*, vol. 15, n°. 4, p. 93–102, Dec. 2020.

[194] K. Chuang, H. Yektaii, D. McLaurin et C. Mayer, "Radio challenges, architectures, and design considerations for wireless infrastructure: Creating the core technologies that connect people around the world," *IEEE Microwave Magazine*, vol. 23, n°. 12, p. 42–59, Dec. 2022.

APPENDIX A LIST OF PUBLICATIONS AND AWARDS

Peer-reviewed Journal Papers

[**J1**] **S. A. Keivaan**, P. Burasa, K. Wu, "Virtual Receiver Matrix and Combinatory Analog Operations for Future Multifunction Reconfigurable Sensing and Communication Wireless Systems," in *IEEE Transactions on Microwave Theory and Techniques*, vol. 71, no. 1, pp. 424-433, Jan. 2023.

[**J2**] **S. A. Keivaan**, P. Burasa, J. Deng, K. Wu, "Concurrent Detection of 2-D Angle-of-Arrival and Polarization Enabled by Virtual Transceiver Matrix Architecture," in *IEEE Transactions on Microwave Theory and Techniques*, vol. 73, no. 9, pp. 6863-6878, Sep. 2025.

[**J3**] J. Deng, P. Burasa, **S. A. Keivaan**, K. Wu, "Waveguide Receiver Array for Joint Communication, Sensing, and Power Transfer Systems," in *IEEE Transactions on Microwave Theory and Techniques*, vol. 73, no. 7, pp. 4204-4217, Jul. 2025.

[**J4**] K. Wu, Y. Bigdeli, **S. A. Keivaan**, J. Deng and P. Burasa, "Integrated Sensing and Communication (ISAC) Transceiver: Hardware Architectures, Enabling Technologies, and Emerging Trends," in *IEEE Journal of Selected Topics in Electromagnetics, Antennas and Propagation*, vol. 1, no. 1, pp. 37-64, Sep. 2025.

[**J5**] **S. A. Keivaan**, P. Burasa, K. Wu, "A Millimeter-Wave 4D Automotive Joint Radar Communication for Accurate Multi-Target Detection in High-Density Environments," *Submitted to IEEE Transactions on Microwave Theory and Techniques.*

[**J6**] **S. A. Keivaan**, P. Burasa, K. Wu, "Evolution of Multi-Port Transceiver Systems: From Foundational Architectures to Virtualized and Reconfigurable Platforms," *Submitted to Electromagnetic Science Journal.*

Patents

[**P1**] K. Wu, **S. A. Keivaan**, and P. Burasa, "Method and device for demodulating signals using multiple receivers," U.S. Patent Application US20250183931A1, filed Feb. 10, 2025, published June 5, 2025.

[**P2**] **S. A. Keivaan**, P. Burasa, and K. Wu, "Method and apparatus for wireless transmission, reception and related operations using reconfigurable matrix of elements," U.S. Patent US12368494B2, granted July 22, 2025.

[**P3**] **S. A. Keivaan**, P. Burasa, and K. Wu, "Integrated Four-Dimensional Sensing and Data Communication System Based on Linear Interference Technique," *Submitted to U.S. Patent*, application No. 92081657US01, 2025.

Conference Papers and Presentations

[**C1**] **S. A. Keivaan**, P. Burasa, K. Wu, "Virtual Receiver Matrix for Future Multifunction Wireless Systems," in *2022 IEEE/MTT-S International Microwave Symposium*, IMS 2022, Denver, CO, USA, 2022, pp. 386-389.

[**C2**] **S. A. Keivaan**, P. Burasa, K. Wu, "Interferometric Receiver Architecture for Multifunction Wireless Systems," in *2022 52nd European Microwave Conference (EuMC)*, Milan, Italy, 2022, pp. 16-19.

[**C3**] **S. A. Keivaan**, P. Burasa, K. Wu, "Virtual Receiver Matrix for Multifunction Communication and Sensing Wireless Systems Using Simultaneous Incident Waves at the Same Carrier Frequency," in *2023 IEEE/MTT-S International Microwave Symposium*, IMS 2023, San Diego, CA, USA, 2023, pp. 1176-1179.

[**C4**] **S. A. Keivaan**, P. Burasa, K. Wu, "Virtual Transceiver Matrix for Future Programmable Wireless Sensing and Communication Frontends," in *2023 IEEE MTT-S International Conference on Numerical Electromagnetic and Multiphysics Modeling and Optimization (NEMO)*, Winnipeg, MB, Canada, 2023, pp. 87-90.

[**C5**] Y. Bigdeli, **S. A. Keivaan**, P. Burasa, K. Wu, "Towards the Development of Large-Scale Multifunction Array Transceiver Systems," in *2023 Asia-Pacific Microwave Conference (APMC)*, Taipei, Taiwan, 2023.

[**C6**] J. Deng, P. Burasa,**S. A. Keivaan**, K. Wu, "Spatially Distributed Polarization Receiver Array for Communication and Sensing Multifunction Systems," in *2024 54th European Microwave Conference (EuMC)*, Paris, France, 2024, pp. 148-151.

[**C7**] **S. A. Keivaan**, P. Burasa, K. Wu, "Joint 4D Radar and Communication System Enabled by Virtual Transceiver Matrix Architecture for Advanced Automotive Sensing and Connectivity," in *2025 IEEE/MTT-S International Microwave Symposium* , IMS 2025, San Francisco, CA, USA, 2025.

Awards

[**C1**] IEEE MTT-S Graduate Fellowship, 2025.

[**C2**] Student Grant, European Microwave Conference (EuMC), Milan, Italy, September 2022.

[**C3**] IEEE MTT-S IMS Ph.D. Student Sponsorship Initiative award, Denver, Colorado, U.S., 2022.